Summer 8-15-2019

Force Requirements and Force Generation During Endocytosis in Yeast

Jonah Kyle Scher-Zagier
Washington University in St. Louis

Recommended Citation

Scher-Zagier, Jonah Kyle, "Force Requirements and Force Generation During Endocytosis in Yeast" (2019). *Arts & Sciences Electronic Theses and Dissertations*. 1947.
https://openscholarship.wustl.edu/art_sci_etds/1947

WASHINGTON UNIVERSITY IN ST.LOUIS

School of Arts & Sciences
Department of Physics

Dissertation Examination Committee:
Anders Carlsson, Chair
Philip Bayly
Shankar Mukherji
Zohar Nussinov
Ralf Wessel

Force Requirements and Force Generation During Endocytosis in Yeast

by
Jonah Kyle Scher-Zagier

A dissertation presented to
The Graduate School
of Washington University in
partial fulfillment of the
requirements for the degree
of Doctor of Philosophy

August 2019
St. Louis, Missouri

Table of Contents

List of Figures

List of Tables

Acknowledgments

I'd like to acknowledge the substantial assistance of my advisor, Professor Anders Carlsson, in helping me carry out the research that went into this thesis, as well as the advice of the members of my committee, Professors Philip Bayly, Shankar Mukherji, Zohar Nussinov, and Ralf Wessel, and the informative input of Professor Elizabeth Haswell. I'd also like to acknowledge Professor Steve Maas and the other members of the FeBio forums for helping me with thorny technical issues with the FeBio software. Finally, I would like to acknowledge my parents and siblings, without whose support, financial and moral, this thesis would not have been possible.

Jonah Kyle Scher-Zagier

Washington University in Saint Louis
August 2019

Dedicated to my parents.

ABSTRACT OF THE DISSERTATION

Force Requirements and Force Generation During Endocytosis in Yeast

by

Jonah Kyle Scher-Zagier

Doctor of Philosophy in Physics

Washington University in St. Louis, 2019

Professor Anders Carlsson, Chair

Endocytosis is a process by which cells bring external materials into the intracellular environment and perform other essential biological functions. The main drivers of endocytosis include clathrin and actin, which help shape the membrane and form the endocytic invagination. In mammalian cells and other cells lacking a wall, the primary barriers to endocytosis are the bending rigidity of the cell membrane and surface tension. However, in cells with a rigid cell wall, such as those of yeast, this process is opposed by a substantial pressure within the cell, known as the turgor pressure, which is generated by a difference in the concentration of osmolytes such as glycerol across the membrane. In order to understand yeast endocytosis, it is necessary to understand how force and curvature generators behave under conditions of high turgor pressure, as well as other possible mechanisms cells may employ to reduce or overcome the turgor pressure barrier.

In this thesis, we model the generation of these high turgor pressures through osmolyte diffusion and accumulation, as well as examining the production of forces by curvature-generating molecules (CGMs) under high turgor pressure. We first investigate the possibility of reducing the turgor pressure barrier to endocytosis by modeling the steady-state reduction of the glycerol concentration, and thus the turgor pressure, in a cell with a single region of increased permeability, corresponding to a cell with a single endocytic zone. We then extend this model to cells with multiple endocytic zones, as well as to the time dependence of the glycerol concentration. We also model the behavior of idealized curvature-generating molecules under high-turgor pressure conditions in the presence of a stiff cell wall. We find that small numbers of channels can produce up to a 50% reduction in the turgor pressure. We also find that model CGMs analogous to clathrin can produce forces nearly sufficient to overcome the turgor pressure.

Chapter 1

Introduction

1.1 Endocytosis in Yeast

Endocytosis is a process through which cells bring in external material via deformation of the membrane. First, an indentation, known as an invagination, forms on the surface of the cell (Figure 1.1). The size of the invagination varies depending on the type of cell and endocytic process: In human cells, it has an initial radius of approximately 100 nm, which decreases to around 50 nm by the neck formation stage (Figure 1.2), while the invagination depth increases to around 70 nm [7], while by contrast in yeast cells the size of the endocytic invagination is under 50 nm [75]. The invagination then lengthens (the previously mentioned neck formation or elongation stage), and finally pinches off into a spherical lipid vesicle (the scission stage). The entire process, from the initial accumulation of proteins on the membrane to scission and vesicle formation takes place on a timescale of around 40-130 seconds [80].

Yeast, particularly the baking yeast *Saccharomyces cerevisiae,* is an ideal model system for understanding endocytosis due to the relative simplicity of its genome, about 12 million

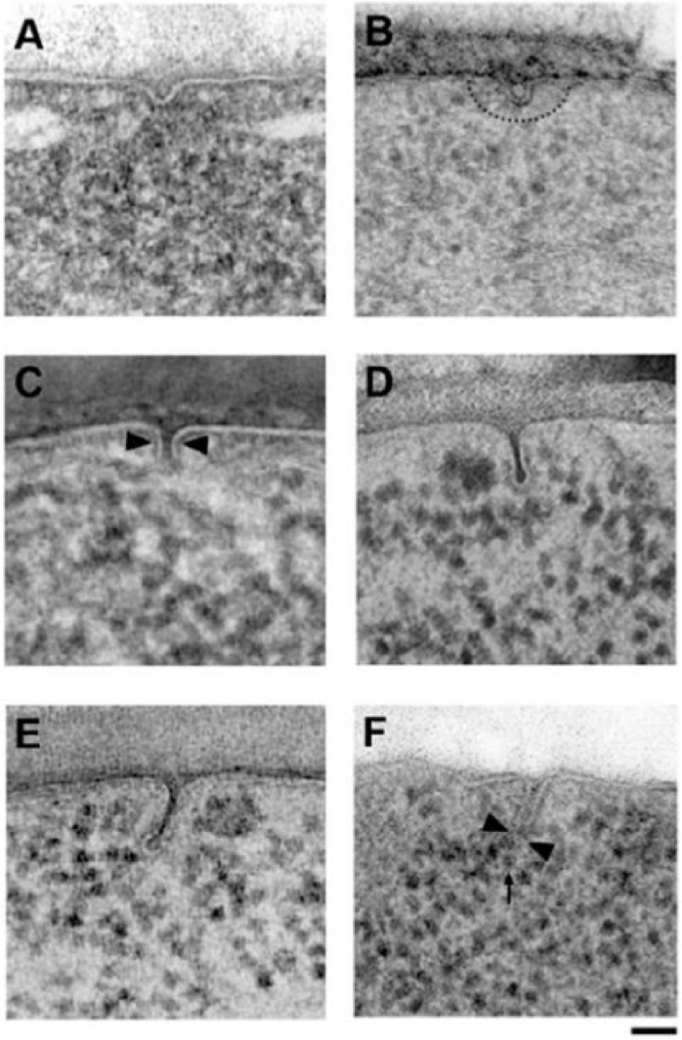

Figure 1.1: Electron tomography images of an endocytic patch at various points in its development, from initial invagination (A) to the beginning (D, E) and completion (F) of scission. Scale bar 50 nm [20].

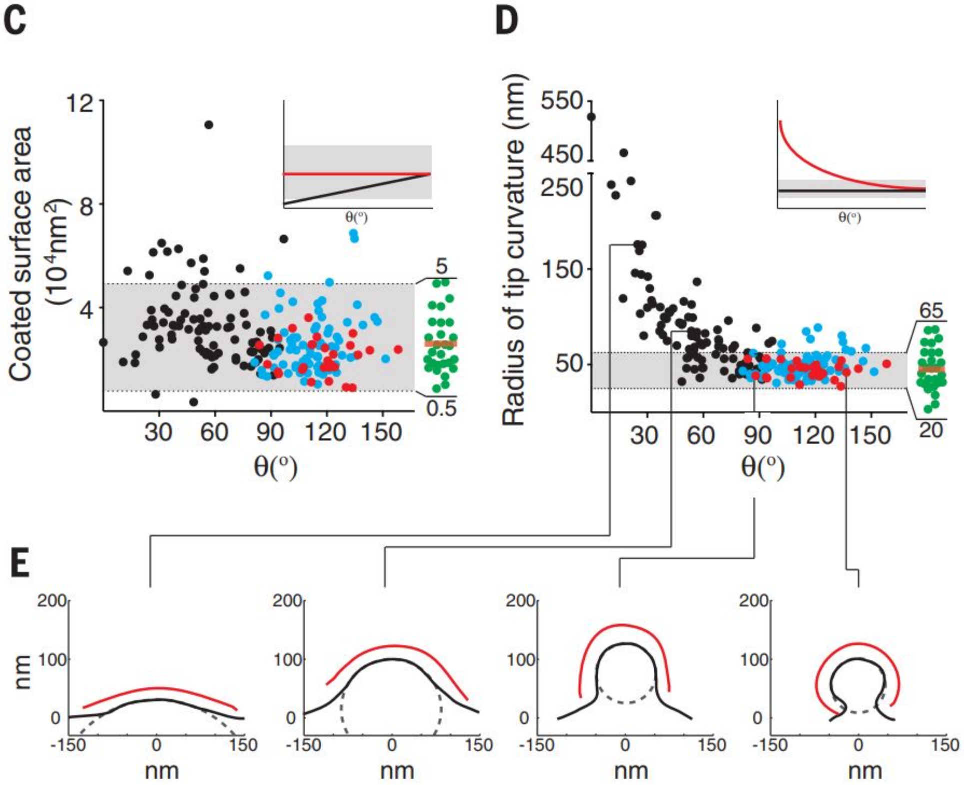

(a)

Figure 1.2: Size of endocytic indentations in nanometers in human cells. Frame C shows the constancy of surface area and Frames D and E show the change in the radius of curvature as endocytosis progresses [7].

base pairs relative to humans' 3.2 billion, and of its structure, since unlike plant or animal cells, it does not form complex differentiated multicellular structures [44, 84] . In yeast cells, the primary form of endocytosis is clathrin-mediated endocytosis (CME), a form of endocytosis that involves the assembly of cage of clathrin triskelia on the interior surface of the cell, which help promote the formation of the invagination by their intrinsic curvature. Clathrin recruitment precedes membrane deformation, although the precise time of bending after clathrin recruitment begins is variable [116].

This process serves a variety of physiological functions. It can incorporate bound receptor-ligand complexes into the cell, allowing the ligands to be brought into the cytoplasm and the receptors to be reincorporated into the membrane. CME can change the surface properties of the membrane, allowing for modulation of signal transduction, and also serves to recycle synaptic vesicles. Due to this versatility, however, it is also exploited by pathogens such as viruses and bacteria to gain access to cells [87].

Endocytosis involves a wide array of proteins (Figure 1.3). The formation of the invagination is preceded by the accumulation of coat proteins, including clathrin, Sla2, and Ent1 and Ent2. The nucleator Las17 and and the branching protein complex Arp 2/3 promote polymerization of actin. The protein Sla2 plays an essential role by binding actin to the endocytic patch by means of interactions with epsin [121, 141, 146]. The epsins Ent1 and Ent2 are adaptor proteins that bind clathrin to the cell membrane, as well as possibly generating curvature independently [37, 69].

The primary force-generating protein associated with CME is actin. Networks of filamentous actin (F-actin) generated by Las17-activated Arp 2/3 complex accumulate around the vicinity of an endocytic patch [103]. Actin generates the necessary forces

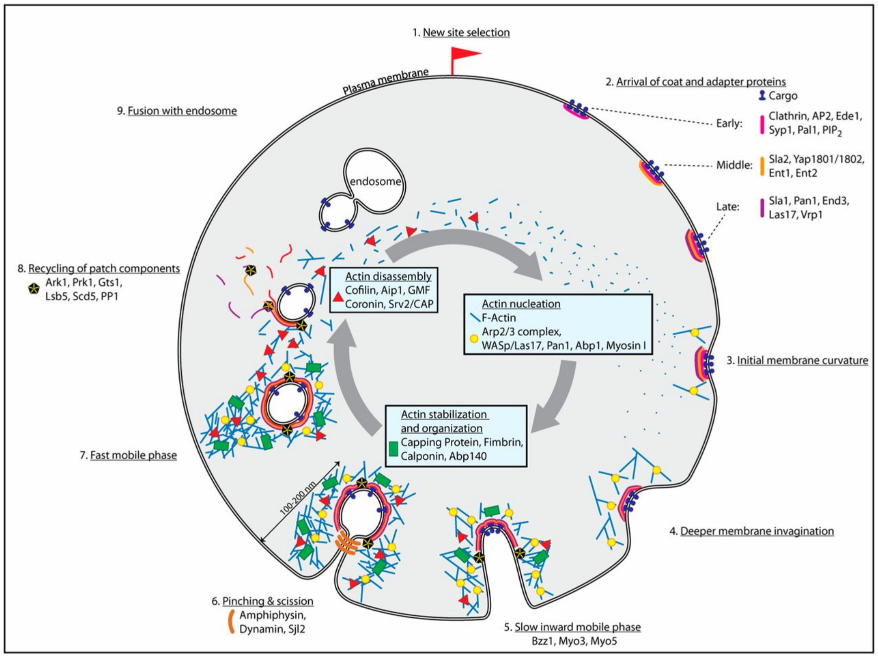

(a)

Figure 1.3: Schematic of stages of endocytosis in yeast [46].

through polymerization of actin monomers, with thermal fluctuations of the membrane providing a gap for additional monomers to polymerize and thus displace the membrane. Rather than polymerizing away from the membrane, actin polymerizes at the membrane and thus pushes on it directly [27]. This actin network around endocytic patches may form a variety of shapes during endocytosis, starting as a ring during the initial stages, while transitioning to a trailing tail-like structure during the latter stages [103]. The network also plays a role in vesicle scission, pinching off the neck of the vesicle.

Endoctytic scission has its own associated proteins, in addition to actin. Among these are yeast dynamin-associated GTPase Vps1, which plays a role in membrane tubulation and also assists in the removal of coat proteins post-scission [139]. Clathrin also affects scission, possibly regulating the time and location at which scission is initiated [76].

There are several force barriers to endocytosis, including surface tension, membrane curvature and osmotic pressure. In mammalian cells, the former two are the primary barrier to endocytosis, since they resist the changes in the area and curvature necessary to produce an invagination [142]. In cells possessed of a rigid cell wall, such as yeast and plant cells, the osmotic pressure difference between the exterior and interior of the cell, known as the turgor pressure, usually is the primary obstacle.

Models of endocytosis have typically focused on actin force generation, curvature-generating proteins, and membrane deformation. For instance, one model considered the balance between the effects of surface tension and polymerization of the CGP clathrin in forming endocytic buds [111]. It found that membrane tension opposed endocytosis, not only directly, but by inhibiting the polymerization of clathrin and thus the generation of curvature, which was validated by experiments on vesicles. Thus, in different regimes of clathrin polymerization energy and membrane tension, the endocytic process would proceed to different stages (Figure 1.4).

Other models have also focused on the balance between surface tension and clathrin bending energy. For instance, Hassinger et al. analyzed a continuum model of endocytic bud formation based on the Helfrich energy [50] (see further discussion of the Helfrich energy in section 1.2), which took into account membrane tension, intrinsic curvature generation by clathrin, and the intrinsic bending energy of the membrane. They found that the process of transition from a flat membrane to an invagination and then an endocytic bud depends on the balance between surface tension σ and the coat rigidity κ, to which clathrin-membrane interactions are a major contributor: at high ratios of σ/κ, there is a rapid transition between the flat and budded shapes, characterized by the presence of a snap-through instability, whereas at low values of σ/κ, the transition is gradual and continuous. Other models have examined the effects of tension in conjunction with actin forces or clathrin curvature generation, again finding snap-through instabilities in the shape dependent on surface tension [138].

Most of these models, including the previous ones, have not directly treated the turgor pressure or the effect of the cell wall. Some have, such as the model of Dmitrieff et al [33], which examined the dynamics of endocytosis using a bending energy approach that incorporated surface tension, the intrinsic curvature of clathrin, and actin force generation modeled as a point force. They found that pressure and bending rigidity had a greater effect on the shape of endocytic pits than surface tension, and estimated that the curvature energy of clathrin was not sufficient to overcome the turgor pressure barrier. As with various previous analyses, they also observed a snap-through instability. They also found that certain types of curvature-generating proteins could help stabilize the shape, which agrees somewhat with the previous results of Hassinger et al.

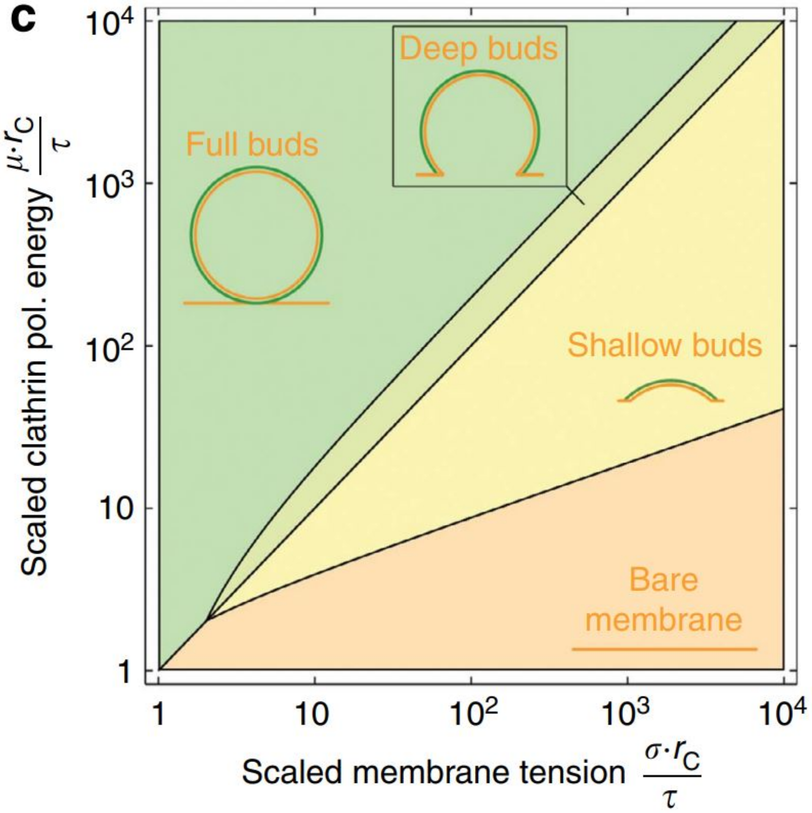

Figure 1.4: Different types of endocytic invaginations form in different regimes of membrane tension and clathrin polymerization [111]

1.2 Membrane Shape and Deformation

Biological cells such as *S. cerevisiae* are surrounded by a fluid lipid bilayer membrane, which serves to separate the intracellular fluid from the external environment. This membrane is composed primarily of phospholipids. Membrane lipids tend to have a hydrophobic tail, which is isolated from the intracellular and extracellular fluid in the interior of the bilayer, and a hydrophilic head, which is exposed to the internal and external aqueous environments. This hydrophobicity effect causes membrane lipids to aggregate and form a bilayer. The cell membrane lipid density is about 5×10^6 per square micron, and about 50% of its mass is lipids. However, the membrane also contains a variety of proteins (Figure 1.5). Among the most important for the purpose of endocytosis are channel proteins, which allow water, ions, and larger molecules to pass through the membrane into the cytoplasm.

The dynamics of the lipid bilayer membrane play a central role in yeast endocytosis. It has a surface tension, which resists attempts at deformation, as does the bending rigidity of the membrane. The membrane may also be shaped by the presence of clathrin or other curvature-generating molecules, including preferentially curved lipids. The lipid bilayer behaves fluidly in response to in-plane stresses, but deforms elastically under out-of-plane forces. In the case of endocytosis in yeast or plants, the cell membrane is also subject to a substantial turgor pressure, on the order of 0.2 MPa in budding yeasts [45], and a confining potential due to the presence of the rigid cell wall. This recent measurement of the turgor pressure was published as we were finishing the work described in Chapter 2. In that work we used an average over existing measurements. More recently, we have come to feel that the recent measurement is the most reliable one.

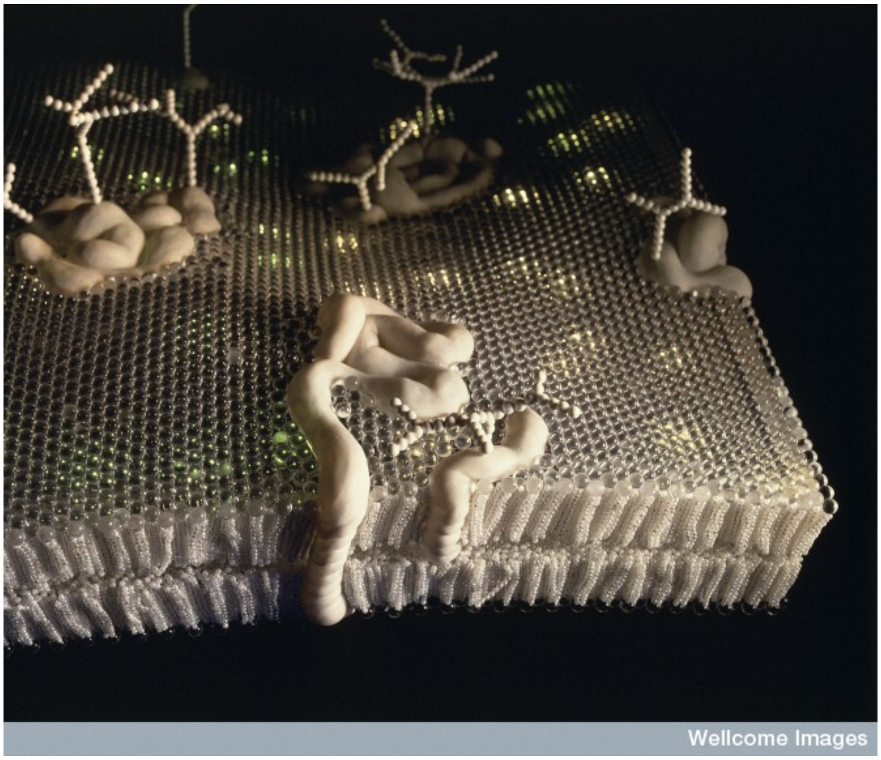

Figure 1.5: Schematic of lipid bilayer membrane with included proteins (Wellcome Images)

The statics and dynamics of a cell membrane can be modeled by the so-called Helfrich membrane energy, which treats the bilayer as a single thin shell subject to perpendicular bending forces and moments. This energy employs the fluid mosaic model, which suggests that there is little resistance to shearing of the bilayer and thus neglects tangential shear forces. The Helfrich membrane energy for the general case (not including the effects of the cell wall) can be written

$$U = 2\kappa \int dA \Big[\big(C - C_0 \big)^2 + \sigma \Big] + \int dV \Pi \tag{1.1}$$

Here C is the curvature associated with a given conformation of the cell membrane, and C_0 is the intrinsic curvature associated with the presence of CGMs; both of these may be functions of the body coordinates of a given point. The volume integration is over the space enclosed by the lipid bilayer membrane, and the area integration is over the surface of the same.

In the case of the early stages of endocytosis, this equation can be greatly simplified by the Monge representation, which parametrizes the membrane deformation in terms of a single radially dependent height, $z(r)$, thus implicitly describing a situation in which the membrane height is single-valued. In this representation the Gaussian curvature C can be written in terms of z as:

$$C = \nabla \cdot \left(\frac{\nabla z}{\sqrt{1 + (\nabla z)^2}} \right) \tag{1.2}$$

The Monge representation typically further makes use of the small-displacement approximation, by which $\sqrt{1 + (\nabla z)^2} \approx 1 + \frac{1}{2}(\nabla z)^2$.

In the absence of turgor pressure or a cell wall, the equation of shape derived by setting the variation of the Helfrich energy to zero and using the Monge approximation factors into the product of a Helmholtz and a Laplacian operator (Helmholtz-harmonic), such that the solution to this equation is given by

$$z(r) = a_0 + a_1 \ln r + a_2 I_0(\xi r) + a_3 K_0(\xi r), \tag{1.3}$$

where $\xi^2 = C_0^2 + \sigma/\kappa$ and I_0 and K_0 are the modified Bessel functions of the first and second kind, respectively. However, this solution is of limited applicability to endocytosis in yeast, since it neglects the contribution of the turgor pressure.

The presence of the cell wall may be modeled in several ways in the Monge representation. The simplest is to use a single potential proportional to z^2 to model the effects of the cell wall. The resulting equation is of biharmonic type and has a simple analytic solution. However, if a potential of this form is used for $z > 0$, it effectively overestimates the turgor pressure (if employed in conjunction with a turgor pressure potential), or further inaccurately represents its dependence on height, if a single quadratic potential is used to represent the combined effects of the wall and turgor pressure.

A more accurate strategy is to model the portion of the membrane above the cell wall and the portion below separately, with the assumption that there is at most one intersection. This renders analytic computation of the coefficients of the two solutions difficult, however, and necessitates numerical computation of the intersection radius by an iterative procedure.

The shape of the lipid bilayer membrane is not fully described by the Helfrich model, however. Even within a continuum description, the bilayer nature of the membrane causes deviations from the simple Helfrich model. For instance, there exist viscous forces between the leaflets of the bilayer, which become non-negligible in the limit of large inter-leaflet relative velocity. These interlayer drag forces play a role in phenomena such as tether formation in a pipette, when the viscous forces due to interlayer drag may be tens of times larger than those due to a thin-shell description based on the neutral surface of the bilayer [36]. At a local scale, individual lipids are not static, but undergo rapid movement, including rotations, displacement, lateral diffusion within a bilayer leaflet and even diffusion between leaflets of the bilayer. Many of these processes occur rapidly: for instance, the diffusion coefficient for lateral movement within a bilayer is around 10^{-8} cm^2/s, corresponding to diffusing about 100 nm in a second [4].

1.3 Clathrin and Other Curvature-Generating Molecules

Curvature-generating molecules (CGMs), specifically curvature-generating proteins (CGPs), play a fundamental role in endocytosis, since to initiate endocytosis the endocytic region must attain a curvature opposite in sign to that of the cell membrane as a whole, which then must tubulate and pinch off into a free vesicle. Among the CGMs involved in endocytosis are proteins such as clathrin and epsin, which are present in clathrin-mediated endocytosis, and proteins such as cavin and caveolin, which help promote clathrin-independent endocytosis pathways [81]. The most important of these CGMs is clathrin, a triskelial molecule (Figure 1.6) which forms roughly hemispherical cages around endocytic zones. These cages change shape as endocytosis proceeds, eventually becoming coats around the detached endocytic vesicles before decoating [110].

Other curvature-generating molecules and methods of curvature generation exist and contribute to endocytosis. For instance, BAR-domain proteins (Figure 1.7) generate

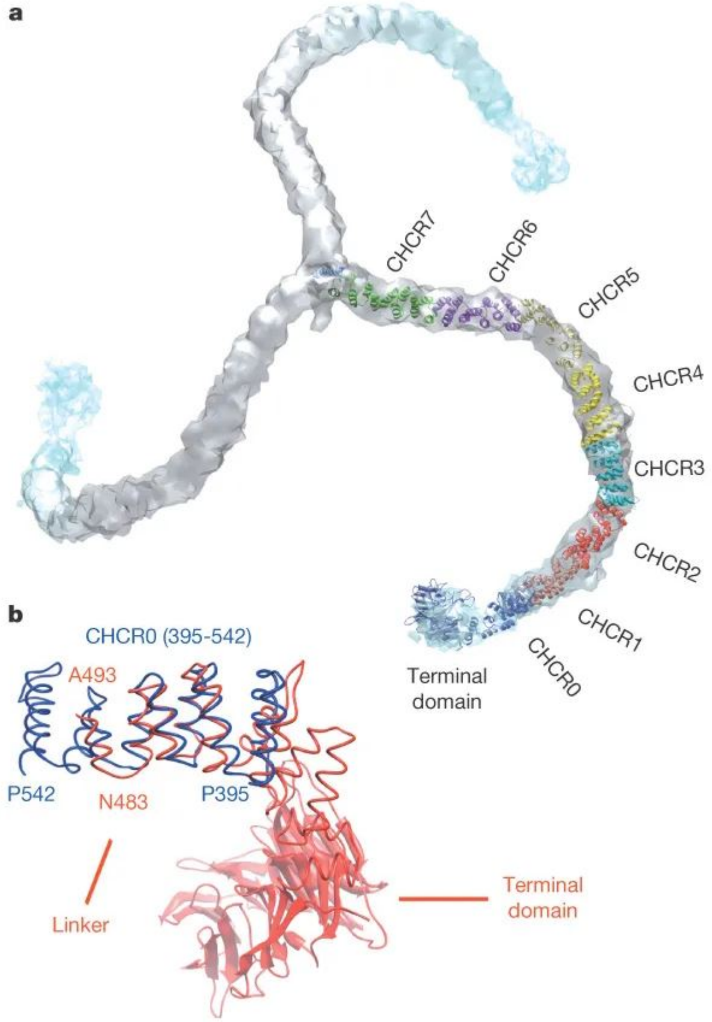

Figure 1.6: Image of clathrin molecule with labeled regions [38]

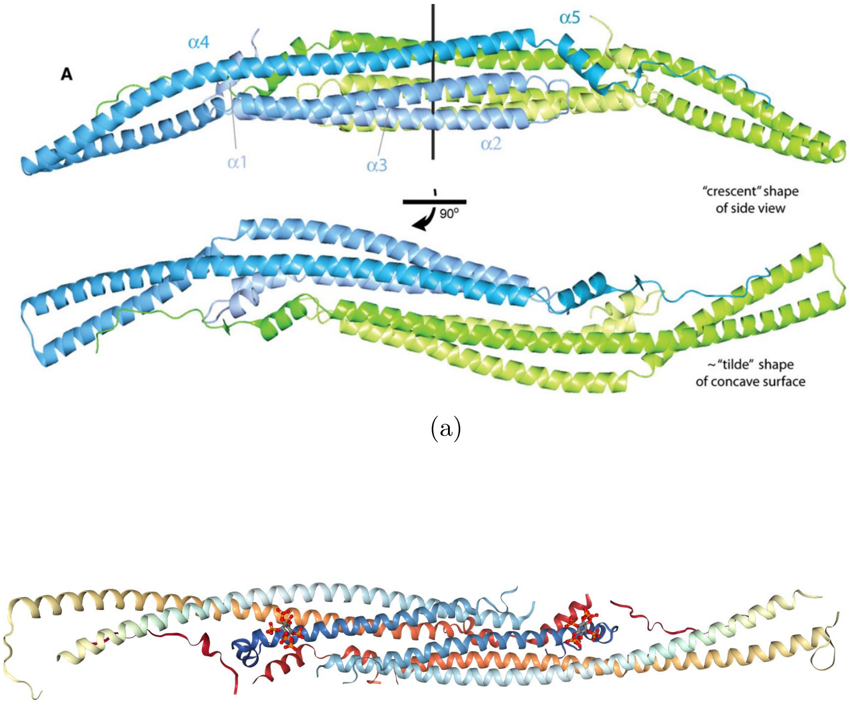

(a)

(b)

Figure 1.7: Image of human F-BAR domain protein (a) and yeast F-BAR domain protein (b) [53, 96]

directionally-biased curvature, having a different radius of curvature in different directions along the surface of the endocytic patch. This class of proteins may generate curvature through causing the membrane to conform to its geometry, as in the case of clathrin, or through methods such as the insertion of amphipathic helices [94]. The curvature-generating behavior of BAR-domain proteins varies based on several factors, such as the density of proteins on the membrane and the membrane surface tension. At high protein density, BAR domain proteins sort according to membrane curvature, whereas at high tension, they promote tubulation and fission [118].

Not all curvature-generating molecules are proteins. Lipids, for instance, can have a preferred curvature due to asymmetries. If the headgroups or tailgroups of lipids are of different sizes, giving them essentially conical shapes, they will induce a curvature in the membrane. The accumulation of lipid species of differing preferred curvature in the two leaflets of the membrane can reinforce this tendency [88]. Some experimental evidence suggests that preferentially curved lipids may play a role in endocytosis [58, 59].

Although molecules such as clathrin and BAR domain proteins generate curvature through their specific folded structure, some methods of curvature generation are independent of the physical structure and arrangement of charged domains in the CGMs. For instance, if there is an excess of proteins on one leaflet of the membrane, the pressure generated from collisions between these molecules can induce membrane curvature, a process known as protein crowding. This process has been demonstrated for various proteins, including epsin, Sar1p and green fluorescent protein [127]. Although there is little apparent dependence on hydrophobicity or other specific features of the molecules involved, larger molecules require lower concentrations to achieve the same degree of crowding, and similarly for molecules that have a higher affinity for membrane binding.

1.4 Elasticity of the Cell Wall

To properly understand the dynamics of endocytosis in systems such as yeast cells and plant cells, it is necessary to account for the dynamics of the stiff cell wall. The cell wall of *S. cerevisiae* and other yeasts (Figure 1.8) is central to the structural integrity of the cell. It is is composed of a variety of molecules, principally glycoproteins and polysaccharides; of these, the polysaccharides comprise the majority of the cell wall mass, with polymers of glucose and mannose predominating. The composition of the cell wall, however, is variable, with the percentage of the various components changing in response to changes in the acidity or nutrient content of the external environment, as well as temperature [3], which may cause variation in mechanical properties such as as the cell wall rigidity. The cell membrane also contains mechanosensing proteins, which interact with the cell wall and may produce conformational changes in the cell wall or in its mechanical properties in response to external forces [72]. The thickness of the cell wall is also highly variable, and depends on the specific environment experienced by the cell. For instance, in the presence of the enzyme Zymolyase, *S. cerevisae* cell walls are thinner and weaker, whereas the presence of diamide causes oxidative stress that leads to cell walls up to 40 nm thicker than in its absence [35]. Another yeast species, *Kluyveromyces lactis,* has a cell wall whose thickness varies from approximately 64 ± 10 nm in the presence of glucose to 105 ± 18 nm in the presence of ethanol, and whose thickness also shows a spatial variation over the surface of the cell [8]. Despite this variation, the thickness of the cell of *S. Cerevisae* tends to be approximately 100 nm, with different experiments measuring 100 ± 15 nm [8], or 102.12 ± 3.38 nm [82], but other studies finding numbers as high as 200 nm for the membrane-wall complex [93], which given the membrane thickness of around 10 nm corresponds to a wall thickness of nearly 200 nm [115].

The mechanical properties, such as the Young's modulus, can be determined by a variety of probes. For instance, one such experiment measured the response of stationary-phase *S. cerevisiae* cells to compression forces up to the point of failure, finding an average Young's modulus of 127 ± 4 MPa for cell walls with an average thickness of 90 nm [122, 124, 125]. The measurements also showed that the cell wall had a breaking strain of 75%. Another experiment determined the Young's modulus of *S. cerevisiae* to be 112 ± 6 MPa in the exponential growth phase and 107 ± 6 MPa in the stationary phase, corresponding to no statistical difference and suggesting the the mechanical properties of the yeast cell wall are constant across different growth phases, as well as roughly agreeing with the previous measurement. This latter experiment found a breaking strain of about 82% [125]. In

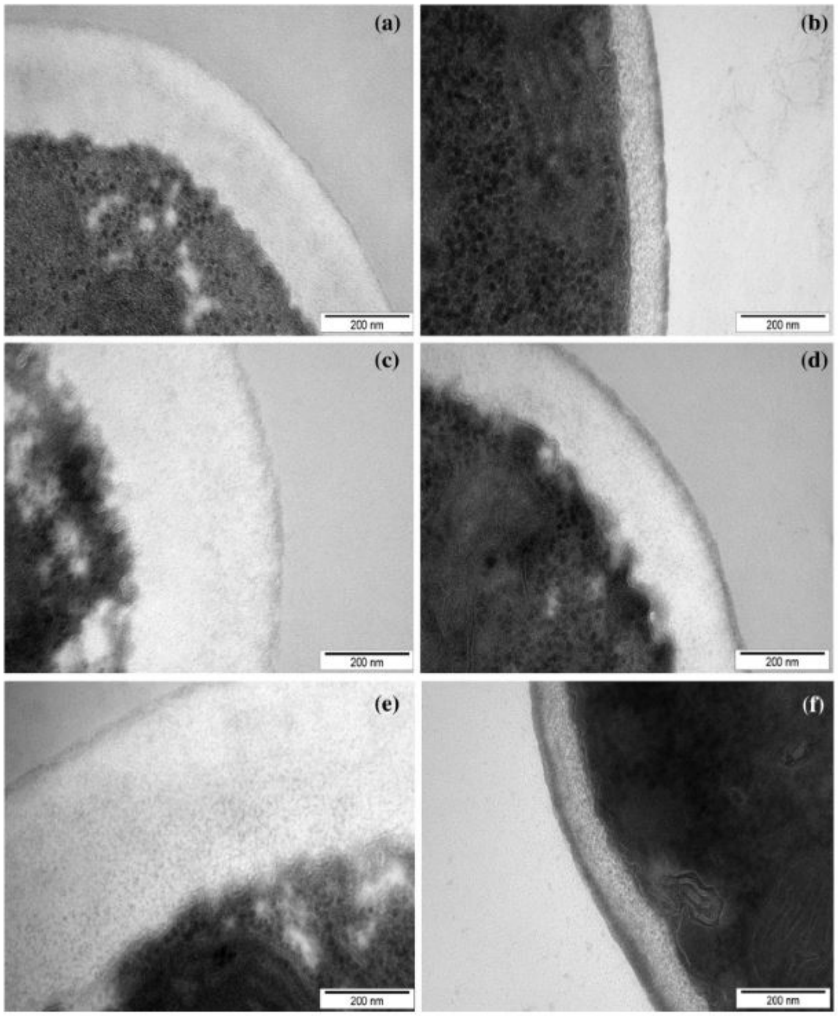

Figure 1.8: Image of yeast cell wall (white) in *C. utilis* at various pH levels [21]

contrast, later research using population averages of the various cells found a Young's modulus of approximately 185 MPa and a breaking strain of 67%. It also found that failure of cells occurred around the equator [129].

In the case of *S. cerevisae*, since the radius of the cell is about 3 μm and the endocytic region is about 100 nm in diameter, the surface of the cell wall can be approximated as flat. The local behavior of the cell wall, such as that of interest in the vicinity of a single endocytic patch, can be modeled as an elastic half-space. The accuracy of this approximation depends on the ratio of size of the region of interest to the thickness of the wall, which for an endocytic patch whose radius is about 50 nm is 0.5. This is an acceptable approximation but may produce some error. Since the thickness of the cell wall is approximately 100 nm, if we take the Young's modulus to be 127 MPa, the Hookean approximation to the wall force is:

$$F_w = (Y/t)z \tag{1.4}$$

where z is the displacement and t is the cell wall thickness. The displacement under the turgor pressure, which is approximately 0.2 MPa, can be estimated by equating this force to the turgor pressure, giving

$$z_0 = \Pi t/Y \tag{1.5}$$

which for the given parameter values is approximately $0.002t$. As such, the thickness of the cell wall is roughly 500 times the displacement under the turgor pressure.

Various models, in fact, treat the cell wall as an elastic half-space; for instance, measurements of the stiffness of the cell or cell wall through AFM indentation [40].

1.5 Turgor Pressure Generation and Measurement

Osmotic pressure refers to the difference in pressure between two regions filled with solvent and solutes and separated by a semipermeable membrane, through which only the solvent can pass. This is particularly relevant in biological systems, in which the polar lipid bilayer membrane behaves as a semipermeable membrane that allows the passage of water but not large polar molecules such as glycerol, partly due to different effective permeabilities from the presence of aquaporins, aquaglyceroporins, and other channel proteins.

If we consider a system with two regions, the first (region 1) containing pure solvent, and the second (region 2) containing a mixture of solvent and solute, we can derive the equilibrium osmotic pressure by considering the chemical potential of the solvent, $\mu_w = \mu_{w,0} + RT \ln x_w$, where R is the ideal gas constant, T is the temperature, and x_w is the mole fraction of solvent. Here $\mu_{w,0}$ is the chemical potential of the pure solvent, i.e. for $x_w = 1$. Since the solvent can flow freely across the lipid membrane, the chemical potential of the solvent in the two regions must be equal:

$$\mu_{w,0}(p) = \mu_w(p + \Pi) = \mu_{w,0}(p + \Pi) + RT \ln x_w \tag{1.6}$$

The definition of the differential chemical potential is, in terms of the entropy per molecule and molecular volume [9]:

$$d\mu_i = -\bar{S}_i dT + \bar{V}_i dp, \tag{1.7}$$

which holds for any component i of a mixture. Thus, when temperature does not vary and the molecular volume does not depend on pressure, we can integrate $d\mu_w$ from p to $p + \Pi$, giving (for the solvent):

$$\mu_{w,0}(p + \Pi) - \mu_{w,0}(p) = \bar{V}\Pi \tag{1.8}$$

Or:

$$- RT \ln x_w = \bar{V}\Pi \tag{1.9}$$

Since $x_w + x_s = 1$, in the limit of low solute concentration we can take $\ln(x_w) \approx -x_s$, giving the osmotic pressure as:

$$\Pi = RTx_s/\bar{V} \tag{1.10}$$

The molecular-level origin of osmotic pressure is complicated, and may vary from system to system. The simplest model explains osmotic pressure by analogy to the case of an ideal gas, to which the definition of osmotic pressure for the case of low solute concentration bears a close resemblance. Because the membrane is permeable only to the solvent molecules, the solvent diffuses freely between the two regions separated by the semipermeable membrane until the density of molecules on either side is equal. By contrast, the solute molecules remain in one region, and this, combined with the equal density of solvent molecules, results in a density in the region with solute, and thus more collisions and a higher pressure. However, this model has limited explanatory power; some have noted that it does not account for the much stronger intermolecular interactions in liquids, and that it supposes a diffusive mechanism whereas osmotic flow is too rapid for diffusion. Alternatively, other models have proposed that the osmotic pressure may arise from statistical-mechanical interactions; with the osmotic pressure being due to interactions between molecules [19].

Another model proposes that in the case of solute molecules that are larger than the solvent molecules, which will generally be the case with solutions of water and organic molecules, interactions with the membrane will cause these larger solute molecules to be further from the membrane, on average, than the solvent molecules. This is hypothesized to create a negative pressure gradient in the direction perpendicular to the membrane, since there are fewer molecules closer to the wall, which in turn produces a net flux of solvent through the membrane [5]. Clearly, this mechanism might not apply to systems where the solute and solvent are of more comparable size, or where the nature of the interactions with the membrane is more complicated.

The term turgor pressure refers to the difference in osmotic pressure between the interior and exterior of a walled cell. The yeast cell has a high turgor pressure, which serves as the primary barrier to endocytosis. This turgor pressure is generated primarily by the presence of the osmolyte glycerol. While in mammalian cells and other cells lacking a wall, endocytic force generators primarily need to overcome the surface tension and bending rigidity of the lipid bilayer membrane, turgor pressure forces in yeast pose a significantly higher barrier.

Although the turgor pressure in yeast cells is clearly high, the question of how to measure its actual value is non-trivial. Some of the earliest methods of measuring turgor pressure including looking at the collapse of gaseous vesicles in cells [60, 71], or even examining the bulk properties of multiple cells in solution [79].

Later, osmotic shock experiments became the primary means of measuring yeast turgor pressure. This involves placing the yeast cell in a hyperosmotic environement, i.e. one enriched in glycerol. Water will then permeate into the intracellular fluid through aquaporins or aquaglyceroporins. The change in volume of the cell is related to the turgor pressure by the linear formula [90]:

$$\Pi - \Pi_0 = \epsilon(\Delta V/V_0)$$

Here V_0 is the baseline volume and ϵ is an elastic modulus. This method is widely used and popular, but suffers from the problem of osmoregulation. Cells regulate the activity of their membrane transporter molecules, and thus their permeability and cell volume, in response to the external osmotic environment. Appreciable adaptation to osmotic shock in the yeast *S. cerevisiae*, for instance, occurs on a timescale of at most minutes [97]. As such, osmotic shock techniques may provide an overestimate of the true osmotic pressure [14].

A more accurate method of measuring the turgor pressure is atomic force microscopy (AFM) indentation experiments. Unlike osmotic shock experiments, the cell may not be able to adapt its turgor pressure to indentation, if done quickly enough. Given the wide range of measured turgor pressures for osmotic shock experiments, between 0.05 MPa and 1 MPa, indentation experiments offer a potentially more accurate method of estimating yeast turgor pressure. The turgor pressure can be approximated from the stiffness of the cell and the radius of the indentation as approximately $\Pi = \frac{k}{\pi r}$ [137]. One AFM indentation experiment found a yeast turgor pressure of 0.21 ± 0.05 MPa [45]. This method has also been applied to other cells with high turgor pressure, such as plant cells [13].

1.6 Solute Reaction-Diffusion Processes in Cells

A variety of processes are involved in the transport of molecules in yeast through endocytosis, both active and passive. Diffusion of water and glycerol, however, is the most important in generating the turgor pressure, the primary barrier to invagination and the most prominent factor differentiating yeast endocytosis from mammalian. Further, production, association and dissociation of molecular species also play a central role: for instance, glycerol is produced inside the *S. cerevisiae* cytoplasm and actin monomers polymerize in order to generate forces that drive endocytosis, processes which require the modeling of a reaction-diffusion system. In the case of glycerol in yeast, synthesis occurs proximally through dihydroxyacetone phosphate (DHAP) reduction, and ultimately through the metabolism of environmental glucose, glycolysis [42, 101].

On the theoretical side, the simple case of the diffusion of a single molecule of diffusion coefficient D can be described by the classic diffusion equation.

$$\frac{\partial C}{\partial t} = D\Delta C \tag{1.12}$$

When chemical reactions between molecules lead to changes in molar quantity, the diffusion equation becomes instead a reaction diffusion equation. For a general system of N molecular species with possible coordinate and time dependence, this is (vectors in bold):

$$\frac{\partial \mathbf{C}}{\partial t} = D\Delta \mathbf{C} + \mathbf{Q}(\mathbf{C}, \mathbf{r}, t) \tag{1.13}$$

The term $\mathbf{Q}(\mathbf{C}, \mathbf{r}, t)$ can have any dependence on molecular concentration, time, or spatial coordinates, but most common reactions are polynomial in the concentration with no explicit spatial or temporal dependence, of the form $\mathbf{Q}(\mathbf{C}) = \sum_i \mathbf{A}_i \mathbf{C}^{n_i}$ for a collection of tensors $\mathbf{A}_i$ and orders n_i.

The special case of a zeroth-order spatially-dependent term, i.e. one of the form $\alpha(\mathbf{r})$, indicates the presence of a source or sink of concentration. Typically this indicates that the formation of the molecule is being treated implicitly, although it can also represent the physical introduction or removal of a solute. In this case, the equation reduces to:

$$\frac{\partial \mathbf{C}}{\partial t} = D\Delta\mathbf{C} + \alpha(\mathbf{r}) \tag{1.14}$$

For instance, in the case of uniform glycerol production within a yeast cell, the term $\alpha(\mathbf{r})$ would be constant for $r < R_{cell}$ and zero for $r > R_{cell}$.

Since cells maintain a homeostatic environment, we will frequently be interested in an steady-state version of the reaction diffusion equation, i.e. $D\Delta\mathbf{C} + \mathbf{Q}(\mathbf{C}, \mathbf{r}) = 0$. A steady-state reaction-diffusion equation can be solved for various boundary conditions, such as Dirichlet boundary conditions (specified concentration) or Neumann boundary conditions (specified molecular current). A particular type of boundary condition of great relevance to endocytosis, however, is the permeability boundary condition, of the form (for a single molecular species):

$$P(C_{out} - C_{in}) = D\frac{\partial C}{\partial n} \tag{1.15}$$

Here $\frac{\partial C}{\partial n}$ represents the normal derivative, and both it and the difference $C_{out} - C_{in}$ are taken across a surface S, and P is the permeability. This corresponds to the idealization of an infinitesimally thin permeable or semipermeable membrane, such as a lipid bilayer. Constancy of the current also implies continuity of the normal derivative, i.e. $\frac{\partial C}{\partial n}|_{out} = \frac{\partial C}{\partial n}|_{in}$, assuming equal diffusion coefficients in the intracellular and extracellular fluid. As the permeability approaches infinity, the concentration difference across the membrane surface goes to zero. Similarly, in the case of zero permeability, this boundary condition simply reduces to the Neumann boundary condition $\partial C/\partial n = 0$, corresponding to no current across the membrane, such that the interior and exterior solutions are decoupled.

The permeability boundary condition also corresponds to a discontinuity in pressure across the boundary, which defines the turgor pressure, proportional to the difference between the osmotic pressures of the external and internal environments.

1.7 Scope

This thesis deals with theoretical modeling and simulation of the forces and conditions involved in clathrin-mediated endocytosis in yeast cells, specifically *S. cerevisiae*, sometimes called brewer's yeast or baker's yeast. Previous research has focused primarily on the contributions of curvature-generating molecules and force generation by actin polymerization, but has made simplistic assumptions about the effects of turgor pressure and cell wall forces, as well as those of curvature-generating proteins under such forces. We seek to address the question of how CME can proceed under high-turgor conditions. Are there any mechanisms that might plausibly reduce the high turgor pressure barrier to endocytosis? What would they look like, and how would they affect the internal environment of the cell? How do CGMs like clathrin behave under these high-turgor conditions, and how do they affect the shape of the endocytic region? Can they overcome the turgor pressure, alone or in conjunction with other molecules?

In the second chapter, we address the possibility of local permeability reduction serving as a mechanism for the reduction of the turgor pressure barrier to endocytosis. We develop a model of a yeast cell with a region of increased membrane permeability, roughly corresponding in size to the ribosome-free actin-rich zone of an endocytic patch. We use spherical Fourier series methods to model the spatial dependence of the equilibrium concentration, and assess the plausibility of generating such permeability increases with channels present in *S. cerevisae*, as well as evaluating the dependence of the permeability reduction on potentially variable parameters such as endocytic patch size.

In the third chapter, we extend the permeability-reduction model of the first chapter using a finite-element analysis technique. We are able to test the previous model against a different method of evaluating the turgor pressure and equilibrium concentration. We also examine the time-dependence and equilibration behavior of a system representing a cell with one or more permeable regions, in addition to looking at the deformation and stresses induced in this system. Since this method allows us to treat multiple permeable patches, we investigate interaction effects between two or more patches, such as whether the average concentration depends on the distribution of patches or how the permeability of one patch is correlated with the concentration at another.

In the fourth chapter, we treat the behavior of model curvature-generating molecules under high-turgor, stiff-wall conditions. We consider a minimal model of clathrin-like molecules as rods with preferred top and bottom distances. We also model the behavior of the lipid bilayer membrane and the cell wall under high-turgor conditions, especially insofar as they interact with the curvature-generating molecules, allowing us to evaluate the distribution of forces generated by CGMs, as well as the extent to which they can overcome the turgor pressure; this model also allows us to determine the profile of the CGM-membrane complex. We assess the dependence of CGM-membrane profile height and force generation on a variety of parameters of interest, such as the turgor pressure itself or the bending rigidity of the CGMs. We also establish the possibility of a stable energetically preferred patch size through a simple attractive energy model.

In the fifth chapter, we summarize the results discussed in the previous three chapters, as well as discussing possible future work, including extensions to the models discussed in Chapters 2-4.

Chapter 2

Local Turgor Pressure Reduction via Channel Clustering

2.1 Introduction

Clathrin-mediated endocytosis (CME) contributes to numerous biological processes, such as cell growth, viral invasion, and neural signaling [87]. It involves the inward bending of a portion of the lipid bilayer, which subsequently pinches off to form a vesicle that moves into the cytoplasm. CME has been studied extensively in yeast, due to the ease of genetic manipulation and fluorescent labeling. In yeast, CME involves actin poymerization as well as clathrin and BAR-domain proteins, which help drive invagination through a non-zero preferred curvature. It is believed [22, 33, 41, 68] that growing actin filaments exert pushing forces on the membrane, which drive the actin network into the cytoplasm. This motion of the actin network exerts pulling forces to drive invagination, through a coupling via the adapter protein Sla2. Recent theoretical work on CME in yeast has treated the mechanics of forces generated by actin polymerization, as well as the intrinsic curvature of the clathrin coat that accumulates on the cell membrane [33, 63, 78, 147]. To date, however, it is not known how actin and other curvature-generating proteins can produce enough force to overcome the large turgor pressure in yeast [1, 12]. Here we explore the hypothesis that increasing the membrane permeability at the endocytic site can locally reduce the turgor pressure and thus facilitate endocytosis. The work discussed here has been published as "Local Turgor Pressure Reduction via Channel Clustering," by Jonah K. Scher-Zagier and Anders E. Carlsson, (*Biophysical Journal*, 2016, vol. 111.12, pp. 2747-2756).

The turgor pressure Π [12] pushes the plasma membrane against the cell wall and thus helps the cell maintain its shape and rigidity. It is generated through the larger internal concentration of glycerol, the main osmolyte in yeast, relative to the outside.

The magnitude of Π is determined by the requirement that the chemical potential of the solvent (water) be constant across the membrane. For a dilute solution, the solvent chemical potential is $\mu(P,T,C) = \mu_0(P,T) - (C/C_{solvent})k_BT$ [77], where P is pressure, T is temperature, and C and $C_{solvent}$ are the solute and solvent concentrations respectively. The chemical potential varies with pressure according to $\partial\mu_0(P,T)/\partial P = 1/N_AC_{solvent}$ [77], where N_A is Avogadro's number and $C_{solvent}$ is given in molar units. Thus the constancy of μ implies [54] that between any two points,

$$\Delta P = N_Ak_BT\Delta C. \tag{2.1}$$

If the points are on opposite sides of the membrane, this implies that the turgor pressure is

$$\Pi = N_Ak_BT\Delta C, \tag{2.2}$$

where $\Delta C = C_{in} - C_{out}$ is the concentration difference across the membrane.

and plant turgor pressures are comparable to these [13]. As our baseline value, we use the value 0.6 MPa obtained by a systematic fit using thermodynamic modeling [113]. In the scenario treated here, where a permeable patch leads to large concentration gradients inside the cell, Eq. 2.1 implies corresponding internal gradients of the pressure. Thus pressure does not equilibrate, even at long times, as long as the concentration gradient is maintained by the continuing production of osmolyte inside the cell. The pressure gradient does not cause macroscopic fluid flow, because there are additional forces on water molecules due to the osmolyte concentration gradient. The situation is analogous to that of water in a swimming pool. The pressure is greater at the bottom, but yet there is no macroscopic flow because the water molecules at the bottom have lower gravitational potential energy. In the present case, the gravitational potential energy variation is replaced by variation in the free energy of water molecules resulting from the inhomogeneous osmolyte concentration.

Can established mechanisms, including curvature-generating proteins and actin polymerization, provide enough force to overcome the turgor pressure barrier? The driving forces from curvature-generating proteins and actin, along with opposing forces from surface tension and turgor pressure, are encapsulated in the “Helfrich" membrane deformation energy:

$$U = \int_S \left[2\kappa(H - H_0)^2 + \sigma - f_{actin} z\right] dS + \Pi V \qquad (2.3)$$

Here κ is the bending modulus, Π is the turgor pressure, dS is an element of membrane area, V is volume of the invagination, H is the mean curvature, H_0 is the spontaneous curvature, σ is the surface tension, z is the inward displacement of the membrane, and f_{actin} is the pulling force density from actin. We estimate whether it is energetically favorable for a hemispherical invagination of radius of $R_i = 30$ nm [75] to form in the presence of accepted values of the turgor pressure. We take $\kappa = 285 k_B T$ [64], and Π=0.6 MPa in the middle of the range of experimental values [31, 45, 90, 95, 113]. Then the stabilizing contribution from the curvature-generating proteins is $= -2\pi R_i^2 \kappa / R_i^2 = -1800 k_B T$ (the negative of the curvature energy of the flattened membrane), while the opposing contribution from the turgor pressure is $(2\pi/3) R_i^3 \Pi = 8250 k_B T$, leaving $8250 k_B T - 1800 k_B T = 6450 k_B T$ to be supplied by actin pulling forces.

It is unlikely that actin polymerization can supply such a large energy. The above calculation suggests that about 22% of the opposing force from turgor pressure is canceled by the curvature-generating proteins, leaving a residual pressure of about $0.47\ MPa$ to generated by actin polymerization. This corresponds to a total force of $0.47 MPa \times \pi (30\ nm)^2 = 1300\ pN$. This force must come from the polymerization of actin filaments around the invagination [22, 33]. The number of growing actin filaments is estimated to be 100-150 [140], so forces of about 10 pN per filament would be required. But the stall force estimated for a $2\ \mu M$ free actin concentration A [140] is only $f_{stall} = (k_B T / \delta \ln{(A/A_c)} \simeq 5 pN$ [56], using a critical concentration of $0.1 \mu M$ [105] and a polymerization step size $\delta = 2.7 nm$. Thus actin polymerization cannot generate the 10 pN per filament force required. The 10 pN estimate is sensitive to the number of growing filaments; a filament number two to three times larger than the estimated value would reduce the force per filament below the stall force. However, it is unlikely that the growing-filament number exceeds our estimate. Ref. [120] estimated the upper bound of the number of growing filaments to be 140, by subtracting the number of capping protein molecules present from the number of Arp2/3 molecules, where the latter number was assumed to correspond to the number of actin filaments. Ref. [17] estimated only 8 growing filaments on the basis of polymerization-dynamics experiments.

Previous work has also suggested that known mechanisms of actin polymerization are too weak to drive endocytosis. A finite-element calculation [22] found that the actin polymerization pressure was too small to overcome the turgor pressure, and that overcoming a turgor pressure of just 0.1 MPa requires an actin network stiffer than any that have been studied to date. Another calculation based on membrane elasticity theory and an actin point force suggested that the required force is even larger than our estimate [33]. Finally, calculations using somewhat different approaches [12] found it implausible that actin polymerization can overcome the turgor pressure. We note, however, that the insufficiency of actin polymerization forces cannot be taken as rigorously proved, because there are substantial uncertainties in all of the quantities used to estimate the slowing of polymerization.

Thus for endocytosis to proceed against current estimates of the turgor pressure, rather extreme assumptions about actin polymerization forces and elastic properties would likely have to hold. A local reduction of the turgor pressure, in the vicinity of the endocytic site, provides a possible alternative to unphysically large actin polymerization forces.

2.2 Materials and Methods

To see how much the turgor pressure might be reduced by a physically reasonable distribution of membrane channels, we solve two diffusion-based models of yeast membranes with locally enhanced permeability. The assumption of a locally enhanced permeability is supported by the observation of patches of the glycerol transporter Fps1 at the cell membrane in budding yeast [134]. However, it is not known whether these patches coincide with endocytic sites.

2.2.1 Assumptions

Model 1 assumes a spherical cell with the membrane permeability increased in a narrow circular patch (see Figure 2.1). Glycerol, the main osmolyte, is produced at a rate, constant in both time and space within the cell. The turgor pressure is determined by a balance between production and leakage. We assume azimuthal symmetry about the center of the permeable patch, and define the angle θ relative to this center. To optimize numerical convergence, we assume a smoothly varying permeability profile of the form $P(\theta) = P_a + P_b \exp[-\theta^2/(\Delta\theta)^2]$. For ease of comparison with our analytic Model 2 below, we also fit this to a model with a discontinuous permeability, having the form:

$$P(\theta) = \begin{cases} P_1 & \theta < \theta_0 \\ P_2 & \theta > \theta_0 \end{cases} \tag{2.4}$$

The coefficients $P_{a,b}$ of the continuous permeability are chosen so that $P(0) = P_1, P(\pi) = P_2$. We then choose $\Delta\theta$ so as to optimize the fit to the discontinuous permeability. For conceptual clarity, we present our results below in terms of θ_0, P_1 and P_2.

Model 2 assumes an infinite, impermeable plane, with two long-distance concentrations C_{in}, C_{out}, and a perfectly permeable hole of radius a (we take $C_{out} = 0$ in our results presented below). These approximations allow for an analytic solution. Model 2 is a good approximation to Model 1 in certain parameter ranges, since the size of the permeable patch is small relative to the size of the cell, and the permeability in the middle of the

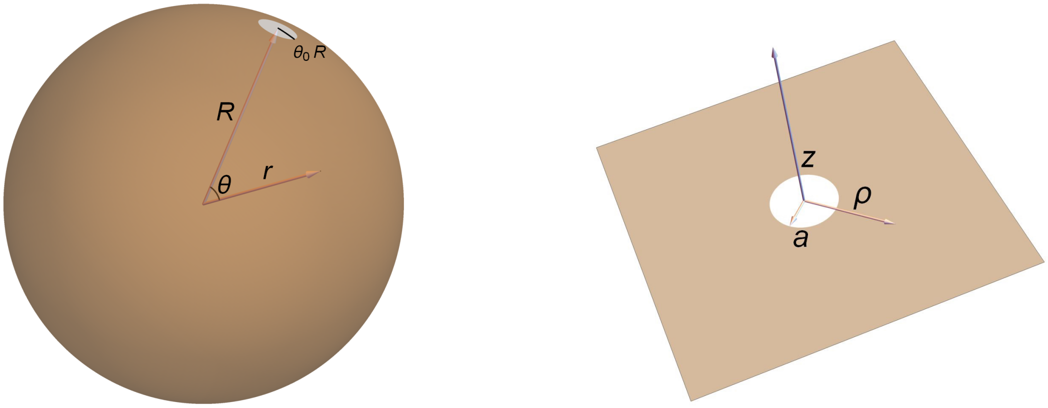

Figure 2.1: Model 1 - spherical cell with permeable patch, and Model 2 - plane with hole

patch is much larger than that far from the patch. In relating Models 1 and 2, we find that a good match is obtained by taking $a = 1.3\theta_0 R$, where R is the cell radius.

In both models, the varying concentrations of glycerol cause a spatially varying hydrostatic pressure because of the constraint of spatially constant chemical potential. The effects of the pressure on the water and glycerol diffusion coefficients, and possible pressure gradient terms in the glycerol current, are assumed small and are neglected.

2.2.2 Equations

In Model 1, the steady-state distribution of glycerol $C(\mathbf{r})$ is governed by the reaction-diffusion equations:

$$D\nabla^2 C(\mathbf{r}) + \alpha = 0 \quad (r < R) \tag{2.5}$$

$$D\nabla^2 C(\mathbf{r}) = 0 \quad (r > R) \tag{2.6}$$

where r is distance from the center of the cell, D is the diffusion coefficient, and α is the rate of glycerol production. The boundary conditions, taking into account the definition of the permeability as the ratio of current density to concentration discontinuity, are

$$\begin{cases} \left(\frac{\partial C}{\partial r}\right)_{r=R} = -P(\theta)(1/D)\Delta C, \\ \lim_{r\to\infty} C(r,\theta) = 0 \end{cases} \tag{2.7}$$

where $\Delta C = \lim_{\epsilon\to 0}\big[C(R-\epsilon,\theta) - C(R+\epsilon,\theta)\big]$ is the concentration discontinuity.

Since Model 2 assumes asymptotic concentrations rather than a production rate, there is no α term, and we have

$$D\nabla^2 C(\mathbf{r}) = 0. \tag{2.8}$$

The boundary conditions are

$$\begin{cases} C(z=0^+,\rho) = C(z=0^-,\rho) \text{ for } \rho < a \\ \left(\frac{\partial C}{\partial z}\right)_{z=0} = 0 \text{ for } \rho > a \\ \lim_{z\to\infty} C(z,\rho) = C_{out} \\ \lim_{z\to-\infty} C(z,\rho) = C_{in} \end{cases} \tag{2.9}$$

Here z is the coordinate perpendicular to the plane (at $z = 0$), and ρ is the radial coordinate, measured from the z-axis going through the center of the hole.

2.2.3 Solution of Model 1

Model 1 has the general solution

$$C(r,\theta) = -\frac{\alpha}{6D}r^2 + \sum_{l=0}^{\infty} C_l (r/R)^l P_l(\cos\theta) \qquad r < R \tag{2.10}$$

$$C(r,\theta) = \frac{\alpha R^3}{3Dr} - \sum_{l=1}^{\infty} \frac{lC_l}{l+1}(R/r)^{l+1} P_l(cos\theta) \quad r > R. \tag{2.11}$$

Here we have expanded $P(\theta)$ as $P(\theta) = \sum_{l=0}^{\infty} A_l P_l(\cos\theta)$, where $P_l(\cos\theta)$ is the Legendre polynomial of order l and $A_l = [(2l+1)/2] \int d\theta \cos(\theta) P(\theta) P_l(\cos\theta)$; the relationship between the coefficients of P_l for $r > R$ and $r < R$ results from the continuity of $\partial C/\partial r$ at R. Integrating the first of Eqs. 2.7 with $P_k(\cos\theta)$ and employing the orthogonality properties of the Legendre polynomials, we see that the C_l in (2.10) and (2.11) satisfy

$$(1/D)\sum_{l=0}^{\infty}\sum_{m=0}^{\infty} \frac{2l+1}{l+1} C_l I_{lmk} A_m + \frac{kC_k}{R}\frac{2}{2k+1} = \frac{\alpha R^2}{2D}\frac{2A_k}{2k+1} + \frac{2\alpha R}{3D}\delta_{k0} \tag{2.12}$$

where (in terms of the Wigner-3j symbol) [66]:

$$I_{lmk} = \int_{-1}^{1} d(\cos\theta) P_l(\cos\theta) P_m(\cos\theta) P_k(\cos\theta) = 2\begin{pmatrix} l & m & k \\ 0 & 0 & 0 \end{pmatrix}^2 \tag{2.13}$$

The 3j-symbols are nonzero only when $J = l + m + k$ is even, and were calculated from the identity

$$\begin{pmatrix} l & m & k \\ 0 & 0 & 0 \end{pmatrix} = (-1)^g \sqrt{\frac{(2g-2l)!(2g-2m)!(2g-2k)!}{(2g+1)!}} \frac{g!}{(g-l)!(g-m)!(g-k)!}, \tag{2.14}$$

where $g = J/2$.

To calculate the coefficients numerically, we approximate the infinite-dimensional system with one of finite dimension by truncating the summation at L coefficients, resulting in an $L \times L$ system (600 by 600, unless otherwise mentioned) to be solved for the coefficients C_l.

The A_l were obtained as numerical integrals. We find that the solution to the truncated system converges as L increases. As a measure of the convergence of the solution we used the variation of the concentration difference across the membrane. The choice of $L = 600$ is justified by Figure 2.2, which indicates that the solution converges for about $L > 150$ for the baseline parameters; for the slowest converging cases the error is less than 1%. Thus we see that the approximate solution of Equations 4 and 5 provides an accurate solution to the problem.

2.2.4 Solution of Model 2

The solution to Model 2 uses the solution for the case $C_{in} = -C_{out}$ given in Ref. [28]. We summarize the method used to obtain the solution. The approach uses the correction to the solution that would hold if no hole were present. The sign of the correction is opposite on each side. We thus have

$$C(\mathbf{r}) = \begin{cases} C_{in} - \tilde{C}(z,\rho) & z < 0 \\ C_{out} + \tilde{C}(z,\rho) & z > 0, \end{cases} \tag{2.15}$$

where $\tilde{C}(z,\rho)$ is the correction for $z > 0$.

At $z = 0$, the boundary conditions (Eq. 2.9) require that $C(\mathbf{r})$ be continuous inside the hole, while outside the hole $\frac{\partial C}{\partial z} = 0$. In terms of the correction, this becomes $\tilde{C}(0^+,\rho) = (1/2)(C_{in} - C_{out})$ for $\rho < a$, $\left(\frac{\partial \tilde{C}(z,\rho)}{\partial z}\right)_{z=0} = 0$ for $\rho > a$.

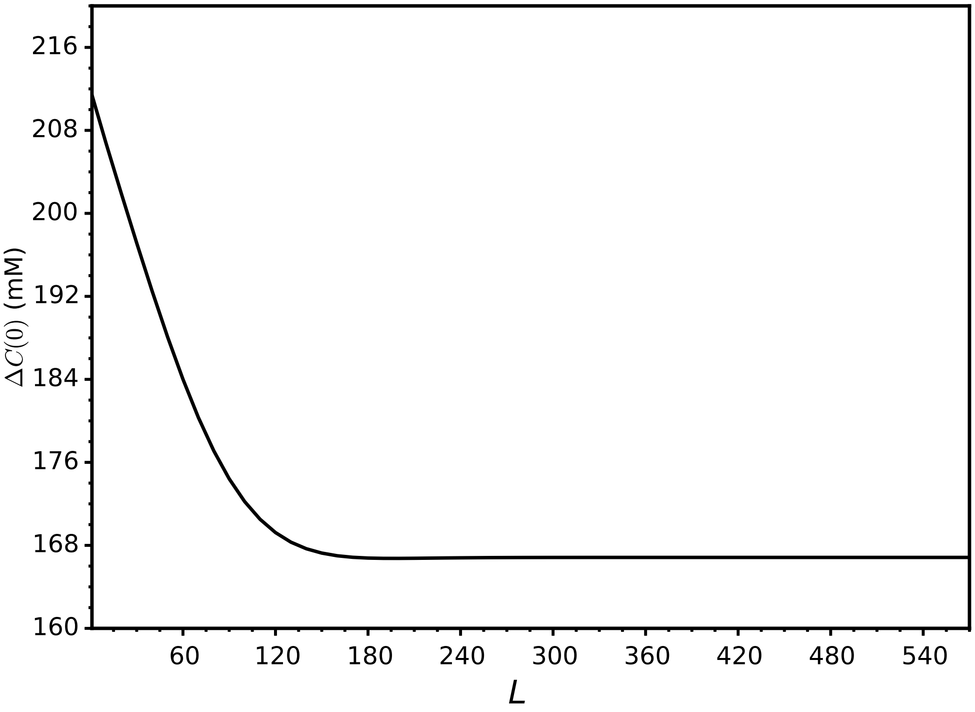

Figure 2.2: Concentration difference at $\theta = 0$ vs L, using baseline parameters. L is the numerical cutoff for Eq. 2.12, and the plot shows that the results are well converged already when $L > 150$.

Eq. 2.8 for $\tilde{C}$ is solved in the Supplementary Material by an expansion in Bessel functions. The result, for $C_{out} = 0$, is

$$C(\mathbf{r}) = \begin{cases} C_{in} - \dfrac{C_{in}}{\pi} \tan^{-1}\left(\sqrt{\dfrac{2}{\zeta + \lambda}}\right) & z < 0 \\ \dfrac{C_{in}}{\pi} \tan^{-1}\left(\sqrt{\dfrac{2}{\zeta + \lambda}}\right) & z > 0 \end{cases} \tag{2.16}$$

where $\lambda = (1/a^2)(\rho^2 + z^2 - a^2)$ and $\zeta = \left(\lambda^2 + \frac{4z^2}{a^2}\right)^{1/2}$.

This model is expected to reproduce the spherical-model results in certain limits. In the spherical model there is a finite discontinuity across the hole, while in the planar model, the concentration is continuous. In the spherical model, there is some membrane current outside the patch, whereas in the planar model there is none. Finally, the spherical model has a curved geometry, while that in the planar model is flat. We thus expect the planar model to approximate the spherical one well only if $P_1 a/D$ is large, $P_2 R/D$ is small, and a/R is small. The second and third conditions hold for all our parameter sets, but the first holds only at the upper end of the values of P_1 that we have treated.

2.3 Results

2.3.1 Model 1 - spherical cell

The parameter values are given in Table 2.1. We vary θ_0 and P_1 since their values are poorly known. In choosing our range of values for θ_0, we note that the radius of the invagination is about 30 nm, corresponding to $\theta = 0.01$, while the radius of the ribosome-free zone around the invagination indicating the presence of F-actin is about 100 nm [75], corresponding to $\theta = 0.033$. The value of θ_0 is likely not much smaller than the radius of the invagination region, because the turgor pressure needs to be reduced over the whole invagination region. However, portions of the permeable region outside the invagination region can contribute to the turgor pressure reduction in the invagination region. Thus we used a range of θ_0 values between 0.006 and 0.03. As a baseline value, we use $\theta_0 = 0.02$.

We base our range of values of P_1 on P_c, the single-channel permeability of a channel protein such as Fps1 in *S. Cerevisiae*, which can transport glycerol to the outside of the cell. We are not aware of experimental estimates of the single-channel permeability of Fps1 or other glyceroporins. The value of P_c was thus determined as being in the middle of the range of water permeability values quoted in Ref. [145], noting that glycerol permeability values are similar to water permeability values [15]. To estimate P_1 from P_c, we assume a constant density of channels. The permeability is taken to be

$$P_1 = (1 - n_c A_c)P_2 + n_c P_c \approx n_c P_c, \tag{2.17}$$

where $n_c = N_c/A_p$ is the channel number density per unit area and A_c is the area per channel. The term with the minus sign is the total area taken up by the channels, and is included to avoid double-counting of the permeability. The second relation holds approximately because $P_1 >> P_2$. Our range of P_1 values corresponds to values of the center-to-center channel distance ranging down to 10 nm; the baseline value of 4×10^{-2} cm/s corresponds to a spacing of 16 nm. Because the measured global permeability values [70] include the effects of channels such as Fps1, and P_2 corresponds to regions of the membrane where channels are depleted by clustering into patches in other regions, we choose our value of P_2 at the lower end of the values quoted in Ref. [70].

Cell radius, R	3 μm	[126]
Patch angular radius, θ_0	0.02 radians (varied)	[75]
Single-channel permeability, P_c	1.0×10^{-13}cm^3/s	[145]
Patch permeability, P_1	4×10^{-2} cm/s (varied)	From assumed spacing of 16 nm
Membrane permeability, P_2	4×10^{-6} cm/s	[70]
Glycerol diffusion coefficient, D	1.1×10^{-6} cm^2/s	10% of value in [23]
Turgor pressure, Π	0.6 MPa	[113]
Glycerol production rate, α	30 mM/s (see section 2.7)	Determined from Π

Table 2.1: Parameter values for spherical-cell model. For parameters that are varied we give baseline values used in most of the plots.

In choosing D, we assumed a cytoplasmic value ten times smaller than the water value given in Ref. [23]. This value is somewhat uncertain, and we treat the effects of varying D in the **Discussion**. The production rate α was obtained by imposing the constraint $k_B T N_A \Delta C(\pi) = \Pi$. We note that because all concentrations in the model are proportional to α, changes in α will not affect fractional reductions in turgor pressure.

Figure 2.3a shows the typical behavior of the concentration as a function of radius, going from inside the cell, through the cell membrane $r = 3\ \mu m$, and continuing outside the cell. Each of the curves shows a dropoff in C approaching the membrane from the inside, with a corresponding feature outside the membrane. This leads to a reduction in the discontiniuty ΔC, which causes a corresponding reduction in the turgor pressure Π according to Eq. 2.2. As seen in the figure, the effect is smaller when the patch width θ_0 is reduced and larger when P_1 is increased. Figure 2.3b shows ΔC as function of angle relative to the patch center. The maximum reduction in ΔC, 31%, occurs at the center $\theta = 0$ of the patch, but the effect is also pronounced for $\theta > \theta_0$; at $\theta = \theta_0$ the reduction is 22%. Thus significant local reductions in turgor pressure occur for our baseline parameter values.

Figure 2.4a shows the concentration difference reduction as a function of P_1 for a range of values of θ_0. All the curves have a similar shape, with the reduction becoming larger as θ_0 increases.

2.3.2 Scaling form for concentration difference reduction

The model has two small dimensionless parameters: $P_2R/D = 1.1 \times 10^{-3}$, and $a/R = 1.3\theta_0 \approx 0.008 - 0.04$. The smallness of these parameters suggests that the ratio of ΔC at the center of the patch to ΔC at the other end of the cell, $\delta c = |\Delta C(0)/\Delta C(\pi)|$, might depend only weakly on P_2 and R, provided that a is kept constant. As mentioned above, there is no dependence on α, since increasing α by a certain factor changes both $\Delta C(0)$ and $\Delta C(\pi)$ by the same factor. If P_2 and R have only weak effects on δc, then δc will be determined almost entirely by P_1, a, and D. There is only one dimensionless combination of these parameters that could enter δc, so a relation of the form

$$\delta c = f(P_1 a/D) \tag{2.18}$$

should hold to high accuracy, where f is an unknown function. This relation makes two predictions. i) That δc is independent of P_2. We have tested this prediction by increasing and decreasing P_2 by a factor of two, and as expected found changes of only 0.5%. ii) If $P_1^{50\%}$ is the value of P_1 required to achieve a 50% reduction in ΔC, so that $\delta c = 0.5$, then $P_1^{50\%} \propto 1/a$. Our test of this prediction is given in Fig. 2.4b, which shows that the relationship

$$P_1^{50\%} = 0.44D/a \tag{2.19}$$

holds to an accuracy of 2%.

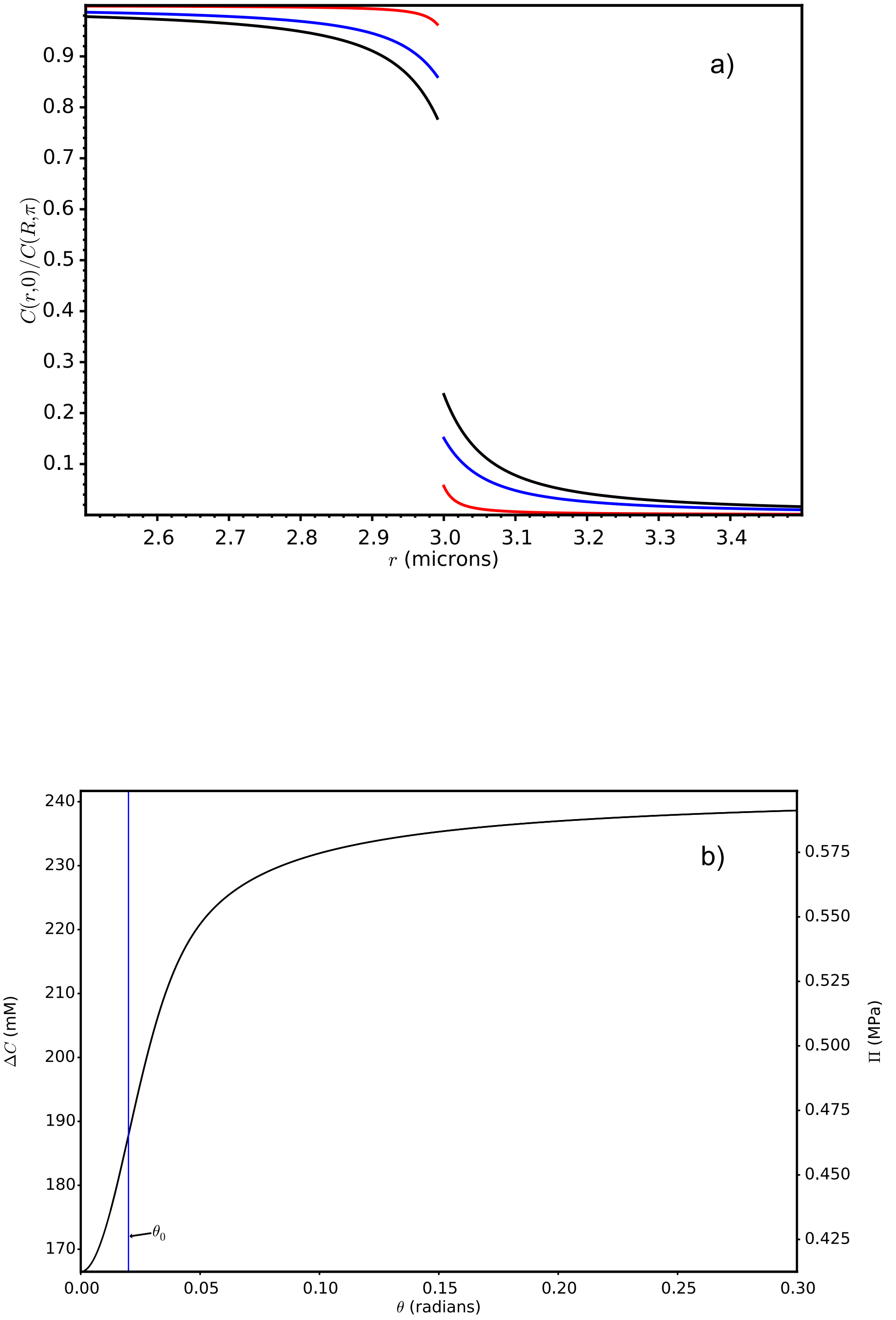

Figure 2.3: a) Concentration vs. radius for various values of θ_0 and P_1. Parameters are baseline except for the following. Red line: $\theta = 0.006$. Black line: $P_1 = 0.08$ cm/s. b) Concentration difference vs. angle for baseline parameters.

2.3.3 Model 2 - planar geometry

Figure 2.5a shows results for Model 2. It is seen that the concentration drops over a range of values of z comparable to the hole width a. We compared these results to those for the spherical model by identifying a with $1.3\theta_0 R$, z with $r - R$, C_{in} with the concentration at the center of the cell, and taking $C_{out} = 0$; the prefactor in a optimized the agreement between the models. We also used a large value of P_1, to optimize agreement with the planar case. The agreement is quite good, with the main difference being that the discontinuity ΔC vanishes in the planar model while it has a small nonzero value in the spherical model.

2.3.4 Analytic theory of patch current and reduction in concentration difference

For the purposes of finding a simple formula for the reduction of $\Delta C(0)$ in Model 1, we first develop an expression for the total current I through the patch. We calculate I in Model 2 as a starting point. Inspection of Eq. 2.16 shows that if $C(\vec{r}, \rho)$ is the solution for a hole of radius a, then $C(\vec{r}/\eta, \rho/\eta)$ is the solution for a hole of radius ηa. In other words the spatial scale of the solution is proportional to a. Since the current density in the hole is proportional to $D\partial C/\partial z \propto a^{-1}$, and the area of the hole is proportional to a^2, it follows that $I \propto a$. Inserting the additional proportionality to C_{in} and D, we obtain

$$I = \nu D a C_{in} \tag{2.20}$$

where $\nu = 1.98$ is obtained numerically from the solution given in Eq. 2.16.

We next calculate the current I through the permeable patch in Model 1 in two limiting cases. We assume that the permeability has the constant value P_1 over a disk of radius a, and the value P_2 outside that disk, and use $\Delta C(\pi)$ as a measure of the bulk concentration discontinuity. In the limit of low permeability $P_1 a/D << 1$, ΔC should be constant over the interior surface of the cell, because diffusion will eliminate concentration gradients. Then $I = P_1 \pi a^2 \Delta C(\pi)$. In the high-permeability limit $P_1 a/D >> 1$, the planar model is applicable, and we use Eq. 2.20. We identify C_{in} in Eq. 2.20 with $\Delta C(\pi)$, since the concentration outside the cell at $\theta = \pi$ is very small, so that $C \simeq \Delta C$. Thus $I = \nu D a \Delta C(\pi)$.

To construct a formula for intermediate values of $P_1 a/D$, we view osmolytes flowing through the patch as experiencing two resistances in series, corresponding to diffusion to the patch and subsequent permeation of the patch. Each process is defined by a resistance $\Delta C(\pi)/I$. The resistance to diffusion is the total resistance for very large P_1, which from the discussion above is $1/\nu D a$. Similarly the resistance to permeation is obtained by taking $P_1 a/D$ very small, and equals $1/P_1 \pi a^2$. Adding the resistances, we obtain $\Delta C(\pi)/I = 1/\nu D a + 1/P_1 \pi a^2$, or

$$I = \Delta C(\pi) \frac{\nu P_1 D \pi a^2}{\nu D + P_1 \pi a}. \tag{2.21}$$

Finally, I is related to $\Delta \bar{C}$, the average of ΔC over the permeable patch. By the definition of the permeability, $I = \pi a^2 P_1 \Delta \bar{C}$. Putting this into Eq. 2.21, we have

$$\frac{\Delta \bar{C}}{\Delta C(\pi)} = \frac{1}{1 + \frac{\pi P_1 a}{\nu D}} \tag{2.22}$$

As seen in Figure 2.5b, this formula gives an excellent description of the simulation results, provided that we use a fitted value of $\nu = 2.9$. It emphasizes the role of the key dimensionless parameter $P_1 a/D$.

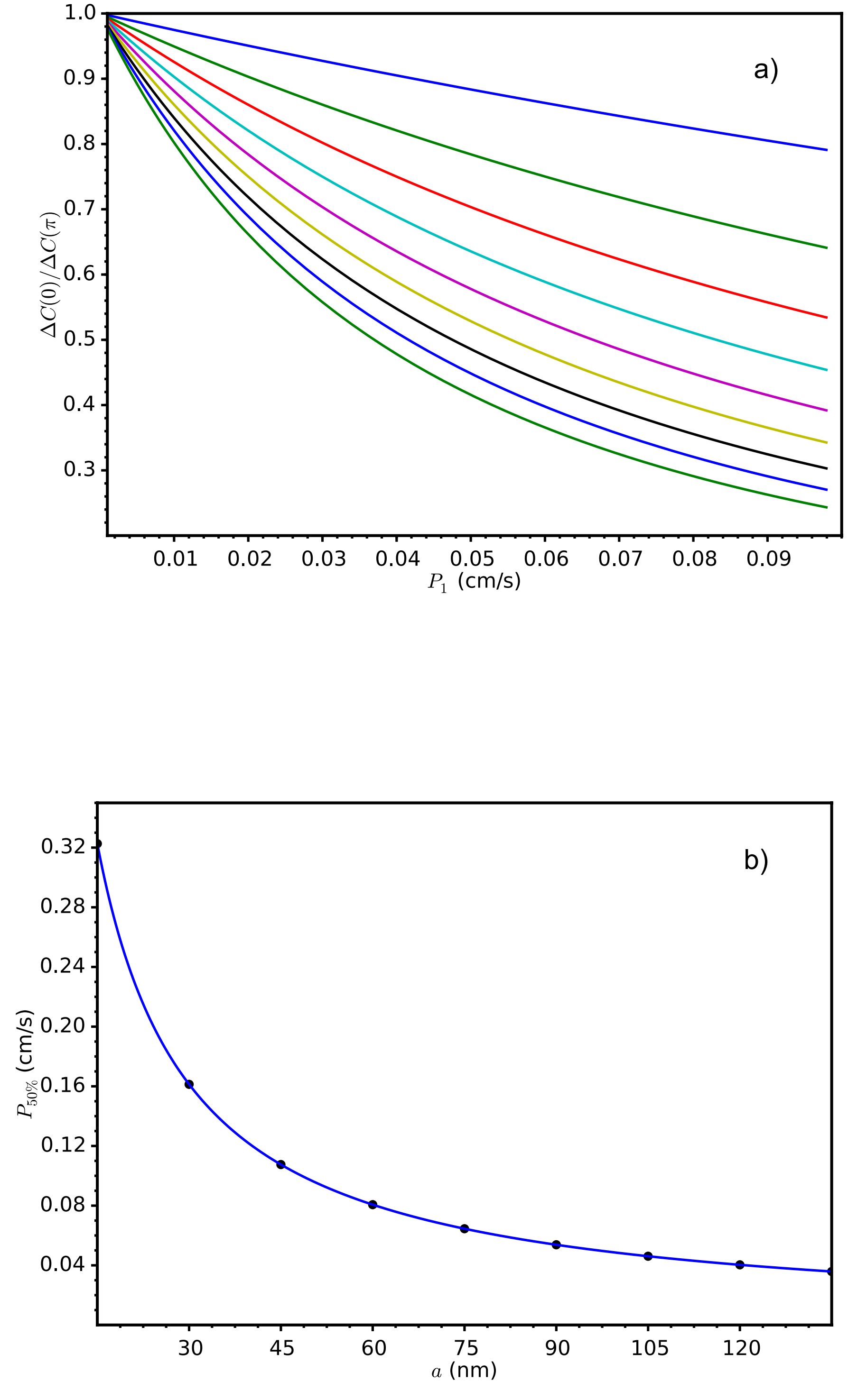

Figure 2.4: a) Concentration difference at $\theta = 0$, relative to bulk membrane value, vs. permeability. Curves (top to bottom) have θ_0 ranging from 0.006 to 0.03, with spacing 0.003. b) Value of P_1 required to reduce $\Delta C(0)/C(\pi)$ by 50%, as function of patch radius a. Solid line denotes fit of form $P_{50\%} = 0.44D/a$.

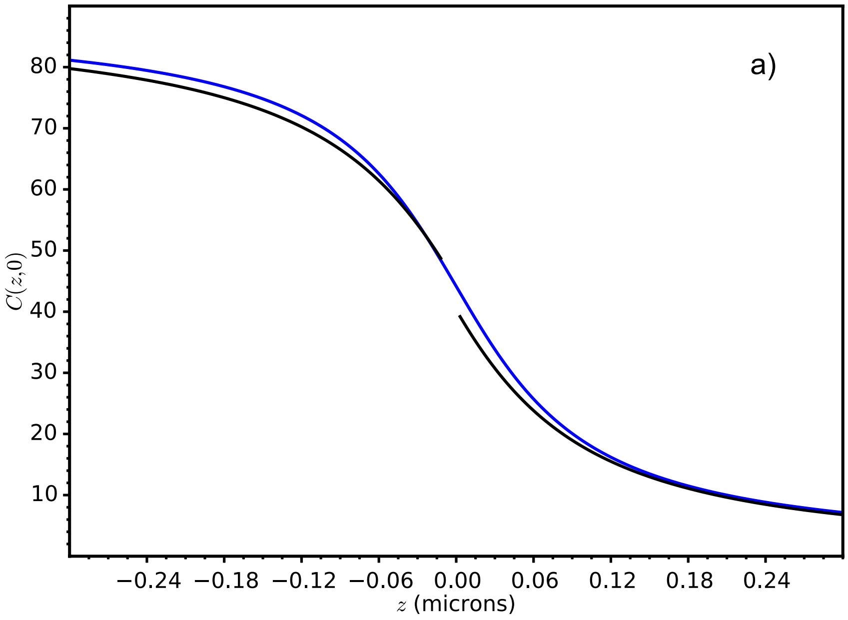

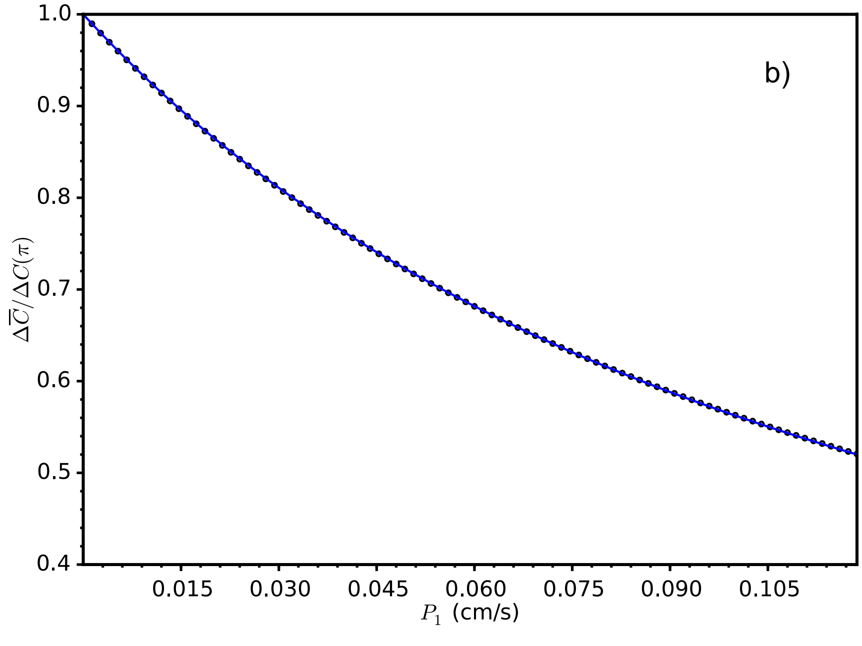

Figure 2.5: a) Planar model concentration (black) and spherical model concentration (blue) along line through center of hole/patch, for $P_1 = 1.0cm/s$ and $a = 1.3\theta_0 R = 78nm$. In spherical model, plot is radial and $r = R + z$. b) Reduction in average concentration over permeable patch as function of P_1. Dots are numerical results and line is analytic theory from Eq. 2.22, using $a = 1.3\theta_0 R$ and a fitted value $\nu = 2.9$.

2.4 Discussion

2.4.1 Extent of turgor pressure reduction in yeast

To evaluate the potential relevance of local turgor pressure reduction to endocytosis in yeast, we estimate a plausible value of P_1. Superresolution imaging of aquaporin clusters in brain cells [123] found an area of 36 nm^2 per aquaporin, corresponding to a center-to-center spacing of 6 nm. Because endocytic protein patches contain a number of other membrane proteins, we use a conservative estimate of a 10 nm center-to-center spacing, corresponding to a channel density n_c of 10^{12} cm^{-2}. Taking the single-channel permeability to be $1.0 \times 10^{-13} cm^{-3}$ (Table 2.1), we find $P_1 = 0.1 cm/s$. Above in Fig. 2.4b, we found that for this value of P_1, a 50% reduction in the turgor pressure will occur as long as the patch radius is 45 nm or greater. Thus patches only slightly larger than the invagination size can reduce the turgor pressure significantly. A patch of 45 nm would contain about 60 channels. This number is comparable to the counts of the coat proteins known to be important for endocytosis in budding yeast. For example, the maximum count of the linker protein Sla2 is about 50 [104]. In addition, this channel cluster size is similar in magnitude to the 35-channel aquaporin clusters previously observed [123].

Eq. 2.22 shows that the turgor pressure reduction is enhanced if D is smaller than the value given in Table 2.1. It will also be enhanced if diffusion in the cell wall outside the membrane is slower than in the cytoplasm. Since treating a cell wall with finite thickness would be significantly more complicated than the calculations we have done, we instead have considered a model in which the diffusion coefficient is reduced uniformly outside the membrane. This corresponds to changing the boundary conditions in Eqs. 2.7. We find that if the outside value of the diffusion coefficient is reduced by 50%, $P_{50\%}$ is reduced by 55%.

For the turgor pressure reduction to facilitate endocytosis, it must persist when the membrane is bent inward, up to the point where a tubule forms and late-arriving curvature-generating proteins assist the process. We see no mathematically practical way of performing the calculations for an inward-bent membrane. However, we note that diffusion currents in general are much more sensitive to the maximum size of their target than to its shape. For example, the diffusion current to a perfectly absorbing cylindrically symmetric ellipsoid of semimajor axis a and semiminor axis b,with $a >> b$, differs from the current to a perfect absorbing sphere of radius a by only a logarithmic factor of $(1/\ln(2a/b))$ [16]; the current to a disk of radius a differs from that to a sphere of radius a by only a factor of $(2/\pi)$ [28]. Therefore the current I from the inside of the cell through the permeable patch should depend mainly on the maximum dimension of the patch rather than its deformation. Further, $I = N_c P_c \Delta\bar{C}$ where N_c is the number of channels, P_c is the single-channel permeability, and $\Delta\bar{C}$ is the average concentration difference across the membrane over the area of the patch. If N_c and P_c are constant, then $\Delta\bar{C}$ will also be relatively independent of patch deformation. Thus the turgor pressure reduction will persist even when the membrane is bent inwards, until it forms a tubule.

The presence of permeable patches can also cause a substantial decrease in the bulk turgor pressure if α is unaffected by the patches. Using the maximum estimate of $P_1 = 0.1 cm/s$, together with the corresponding patch radius of 45 nm, we find a global turgor pressure reduction of 52%. This does not affect our key results because we focus on the *ratio* of the turgor pressure at the permeable patch to that in other parts of the cell. Because the permeable patch is small, the measured turgor pressure corresponds to the calculated value away from the patch. The effect on the bulk turgor pressure will be reduced if P_2 is larger than is assumed in Table 2.1, because a lower fraction of the total osmolyte current will flow through the patch. It will also be reduced if D is smaller, because this reduces the required values of P_1 and a, according to Eq. 2.19.

2.4.2 Relation to experiments

We are not aware of experiments currently in the literature that can test the hypothesis of local turgor pressure reduction in yeast. However, the efficiency of invagination is greatly reduced in deletion mutants of the channel Fps1 [1], an effect that could increase turgor pressure either locally or globally. Fps1 localizes in membrane patches [134]. To establish the extent of channel clustering at endocytic sites, one could use two-color fluorescence imaging to measure colocalization of Fps1 and with endocytosis markers such as the early scaffold protein Ede1 or the polymerized-actin proxy Abp1. Colocalization of channel patches with endocytic proteins would indicate that the turgor pressure is locally reduced around the endocytic site. Appearance of the channels before Ede1 would suggest that the channels have a function in marking the endocytic site. On the other hand, appearance of the channels after Abp1 could mean that polymerized actin is important for recruiting the channels. Such a possibility is suggested by the documented effects of polymerized actin on channel dynamics in other types of cells [49, 86, 148]. If the channel patches do colocalize with endocytic sites, superresolution measurements of the distribution of channels could provide a concrete test of our hypothesis.

Previous experiments have demonstrated that the effect described here, variations of osmotic pressure difference across the membrane caused by variations in channel density, does function on larger spatial scales. For example segregation of aquaporins and Na^+/H^+ channels to the leading edge of cancer cells led to osmolyte concentration gradients over the length of the cell, which in turn created internal pressure gradients that drove migration through artificial channels [130]. Here we predict that gradients of osmolytes over much smaller distances, caused by higher densities of channels, will lead to osmotic pressure variations over these smaller distances.

2.4.3 Application to plant cells

The high turgor pressure in plants also poses conceptual difficulties in rationalizing the mechanobiology of endocytosis, and some early papers actually doubted the existence of the process for this reason [51, 100]. Endocytosis in plants has some parallels to the process in yeast, in particular its polymerized-actin dependence [10, 11]. The difficulties of overcoming high turgor pressure in plants by an actin-dependent process might thus be eased by a local turgor pressure reduction mechanism like that we discuss here for yeast.

2.4.4 Alternative mechanisms

There are several other possible mechanisms that might deal with the difficulty of generating sufficient force via actin polymerization and curvature-generating proteins. A calculation based on the total number of type-I myosins in fission yeast [12], assuming that each one can generate 2 pN of force, suggested that they could overcome the turgor pressure, but only over a smaller region of radius 10 nm. The geometric arrangement of myosins that would supply forces with the correct orientation and distribution is also not known. One possibility is that the myosins turn actin filaments into "superpolymerizers" by i) binding the filaments to the membrane and ii) moving to the growing tip of the actin filament after each polymerization event and keeping it far enough from the membrane that new subunits can be added freely [133]. In this hypothesis, myosins act somewhat like formins, which drive processive elongation of actin filaments while bound to the membrane. An alternate possibility is one analogous to tubulation of giant unilamellar vesicles driven by type-1 myosin [144], where the driving force for tubulation came from myosin motion along a preexisting actin scaffold. We are not aware of measurements of the force-generating capability of yeast type-1 myosins, but mammalian type-1 myosins are able to generate up to 5 pN of force per molecule [48]. It is also possible that there are growing actin filaments that were not detected in the previous filament counts based on Arp2/3 complex mediated branching [120, 140]. These could, for example, be generated by domains on the actin nucleator Las17 that act independently of the Arp2/3 complex [136].

It has also been suggested that polymerization of actin filaments along the membrane could generate much larger forces in a wedge-like geometry [34]. The transmission of such forces to the membrane would require a vary stiff actin gel [22]. There is no proof that a gel with such properties exists, but the high crosslinking fraction in endocytic actin patches could make them much stiffer than other forms of polymerized actin.

Another possibility is that curvature-generating proteins (CGPs) could be providing a very large fraction, say 90% of the force overcoming turgor pressure. However, if this were the case, one would expect that the large heterogeneity between cells, and between endocytic events in the same cell, would often lead to the CGPs exerting sufficient force to drive the process by themselves, in the absence of actin polymerization. Correlative electron-microscopy and light-microscopy experiments [75] have shown that this is not the case: substantial membrane deformation seldom or never occurs without polymerized actin.

Finally, the global turgor pressure could be overestimated. The turgor pressure is typically measured indirectly [113], by exposing the cell to increasing solute concentrations and measuring the volume change. The turgor pressure is proportional to the minimal external solute concentration increase that causes the cell wall to collapse, on the assumption that the membrane collapses at zero turgor pressure. These methods could overestimate the turgor pressure because cells react to increasing external solute concentration by increasing the internal solute concentration, thus requiring higher external concentrations for collapse [134]. Osmoregulation could also confound mechanically based turgor pressure measurements [95], if internal osmolytes are upregulated in response to force opposing cell growth. Direct methods using an indentor that penetrates the cell wall are impractical in yeast because of the small system size. But experiments in plant cells [13] have shown good consistency between indirect and direct methods. Therefore, for the global turgor pressure in yeast to be strongly overestimated, osmoregulation mechanisms in yeast would have to be more efficient than in plants.

2.5 Author contributions

JSZ collaborated on developing the mathematical formalism, implemented and performed the calculations, generated the figures, and collaborated on writing the paper. AEC collaborated on developing the mathematical formalism and on writing the paper, and supervised the project.

2.6 Acknowledgements

This work was supported by the National Institutes of Health under Grant R01 GM107667. We appreciate informative conversations with Elizabeth Haswell.

2.7 Erratum

The default value of the glycerol production rate used in the figures, except for Figure 2.5a, is not 30 mM/s, but rather 18.6 mM/s. This corresponds to the production rate that makes the concentration on the side of the cell opposite the permeable patch approximately equal to 242 mM, corresponding to 0.6 MPa. The value given in Table 2.1, 30 mM/s, is several times too large. The value of alpha for Figure 2.5a corresponds to a concentration of 88 mM, or about 0.2 MPa, on the side of the cell opposite the patch. This value is likely more accurate, since it corresponds to the turgor pressure determined through indentation experiments on S. Cerevisiae.

Local Turgor Pressure Reduction
by Channel Clustering
Supplementary Material

Solution of planar model

Since there are no sources in this model, the concentration is described by Laplace's equation, $\nabla^2 \tilde{C}(z, \rho) = 0$. From the cylindrical symmetry of the problem about the z-axis, the general form of the correction to the concentration may be written as

$$\tilde{C}(z, \rho) = \int_0^\infty dk \, A(k) e^{-k|z|} J_0(k\rho) \tag{2.23}$$

Here $J_0(k\rho)$ is the zeroth-order Bessel function of the first kind. The integral form of the boundary conditions is

$$\int_0^\infty dk \, A(k) J_0(k\rho) = \frac{1}{2}(C_{out} - C_{in}) \text{ for } \rho < a \tag{2.24}$$

$$\int_0^\infty dk \, kA(k) J_0(k\rho) = 0 \text{ for } \rho > a \tag{2.25}$$

We make the substitutions $\rho = ax, t = ka, A(k) = a\frac{(C_{out} - C_{in})}{\pi} f(t)$.We then have

$$\int_0^\infty dt f(t) J_0(xt) = \frac{\pi}{2} \text{ for } x < 1 \tag{2.26}$$

$$\int_0^\infty dt \, t f(t) J_0(xt) = 0 \text{ for } x > 1 \tag{2.27}$$

The solution to this equation is outlined in [85]. We write:

$$\int_0^\infty dt\, t f(t) J_0(xt) = \frac{1}{x}\frac{d}{dx}\int_x^1 ds \frac{s\psi(s)}{\sqrt{s^2-x^2}}, \tag{2.28}$$

where is a function to be determined. This only holds for $0 < x < 1$, else the left-hand side is zero by Eq. 2.27. Inverting the Hankel transform, integrating by parts, and recalling that $J_0(0) = 1$ and $J_0' = -J_1$, we have

$$\begin{aligned} f(t) = \int_0^1 dx\, J_0(xt) x \frac{1}{x}\frac{d}{dx}\int_x^1 ds \frac{s\psi(s)}{\sqrt{s^2-x^2}} = \int_0^1 dx\, J_0(xt)\frac{d}{dx}\int_x^1 ds \frac{s\psi(s)}{\sqrt{s^2-x^2}} = \\ -\int_0^1 ds\, \psi(s) - \int_0^1 dx\, \frac{d}{dx}\left[J_0(xt)\right]\int_x^1 ds \frac{s\psi(s)}{\sqrt{s^2-x^2}} = -\int_0^1 ds\, \psi(s) + \int_0^1 dx \int_1^x ds\, \frac{st J_1(xt)}{\sqrt{s^2-x^2}}\psi(s) = \\ -\int_0^1 ds\, \psi(s) + \int_0^1 ds\ \ st\psi(s) \int_0^s dx\, \frac{J_1(xt)}{\sqrt{s^2-x^2}} \end{aligned} \tag{2.29}$$

From the relation [47]

$$\int_0^s dx\, \frac{J_1(xt)}{\sqrt{s^2-x^2}} = \frac{2\sin^2(st/2)}{st} = \frac{1-\cos(st)}{st}, \tag{2.30}$$

we have

$$f(t) = -\int_0^1 ds\, \psi(s)\cos(ts). \tag{2.31}$$

Then (2.30) becomes

$$\pi/2 = -\int_0^\infty dt \int_0^1 ds\, J_0(xt)\psi(s)\cos(ts) = -\int_0^x ds\, \frac{\psi(s)}{\sqrt{x^2-s^2}}, \tag{2.32}$$

where we have used the relation [47]

$$\int_0^\infty dt\, J_0(xt)\cos(st) = \frac{1}{\sqrt{x^2 - s^2}} \quad (x > s); \tag{2.33}$$

for $x < s$ the integral vanishes. The solution to Eq. 2.32 is $\psi(s) = -1$, or $f(t) = \frac{\sin t}{t}$. We then have $A(k) = \frac{(C_{out} - C_{in})}{\pi} \frac{\sin ka}{k}$, and the correction is

$$C^{(1)} = \int_0^\infty dk\, \frac{\sin(ka)}{k} e^{-k|z|} J_0(k\rho) = \sin^{-1}\left[\frac{2a}{\sqrt{k^2 + (\rho + a)^2} + \sqrt{k^2 + (\rho - a)^2}}\right], \tag{2.34}$$

where the second equality is obtained from Ref. [47]. Algebraic manipulations show that this is $\tan^{-1}\left(\sqrt{\frac{2}{\zeta + \lambda}}\right)$, justifying Eq. 15.

Chapter 3

Time-Dependent Analysis of Permeability-Increase Mechanism for Endocytosis

3.1 Introduction

As discussed above, endocytosis is a process by which cells incorporate material from the external environment, or from the cell's own lipid membrane, into the extracellular fluid. It serves a variety of purposes, including incorporating food molecules, modulating the properties of the membrane to facilitate signal transduction, and providing a pathway that can be exploited by pathogens to enter the cell, such as allowing viruses access for the purposes of replication [87]. This process involves an assembly of dozens of specialized proteins, notably actin, which generates forces through polymerization of monomers; clathrin and other curvature-generating proteins, which stabilize and promote the curved shape of the endocytic vesicle; molecules that promote attachment to the plasma membrane; and a variety of signaling molecules [67, 106].

The primary obstacle to endocytosis in yeast is the turgor pressure, the difference in osmotic pressure between the extracellular fluid and the external environment. Measurements of turgor pressure in yeast are difficult because of the presence of the stiff cell wall [124] and because of the capability of yeast cells to osmoregulate, adjusting their internal glycerol levels in response to external osmotic stimuli [6, 112]. However, AFM indentation experiments have estimated a turgor pressure of 0.2 MPa [45].

In the previous chapter, we considered the possibility of local turgor pressure reduction by a single endocytic patch in a steady-state situation [114]. In real cells, endocytosis is a dynamic mechanism that takes place over various timescales, depending on the type of endocytosis: for instance, certain forms of CME in neurons take anywhere from less than one second to 50 seconds [128], whereas the whole process CME in yeast can occur in 40-120 seconds [80], although the membrane deformation may occur faster, on the scale of 15-30 seconds [75]. In addition, a single endocytic zone constitutes a small fraction of the total cell area; as such, there is usually more than one endocytic event occurring at any given time in a single cell. Some estimates of endocytic event frequency in yeast protoplasts are around 2 events per minute, depending on factors such as the concentration of glucose in the environment [25]. Endocytic frequency also depends heavily on the cellular membrane composition [32]. Thus, if regions of reduced turgor pressure are associated with endocytic patches, there could be several permeable patches present simultaneously.

The primary osmolyte in yeast is glycerol, which generates turgor pressure through chemical potential differences across the cell membrane. The glycerol concentration profile is determined by the diffusion of glycerol through the intracellular and extracellular fluid, which corresponds to a multilayer diffusion problem, where the intracellular and extracellular fluid constitute separate layers, and the cell membrane can be modeled as either an additional, thinner layer or as an interface condition between the other two layers. Multilayer diffusion, including the analogous case of heat diffusion, has been extensively studied, particularly from a theoretical perspective. For instance, for a one-dimensional system of an arbitrary number of layers, the critical time has been found to depend not only on the diffusion coefficients of the layers, but also on their spatial ordering [55]. Non-Euclidean geometries have been studied as well, usually with some type of simplification, such as assuming spherical symmetry or limiting the treatment to certain types of boundary conditions [24, 39].

3.2 General Equations

We model the diffusion of glycerol in a spherical cell with a spatially and temporally constant production rate, as well as the surrounding fluid. The cell is permeable to glycerol, and has one or more regions of increased permeability. This corresponds to solving the equation

$$D\nabla^2 C(\mathbf{r},t) + \alpha(\mathbf{r}) = \frac{\partial C(\mathbf{r},t)}{\partial t} \tag{3.1}$$

subject to the permeability boundary condition

$$P(\theta,\phi)(C_{out}(R,\theta,\phi,t) - C_{in}(R,\theta,\phi,t)) = \left.\frac{\partial C(r,\theta,\phi,t)}{\partial r}\right|_{r=R}, \tag{3.2}$$

continuity of the normal derivative at $r = R$, and other appropriate boundary conditions depending on the specifics of the system, such as finiteness at the origin.

Our primary model uses the finite element software FEBio [83] to model the behavior of glycerol diffusion in a spherical model yeast cell with a rigid cell wall. This package can model the time dependence and steady-state behavior of the solute concentration of a multiphasic system consisting of one of more diffusing solutes, corresponding to the previous equations, as well as the deformation of the system. We modified the the software with a custom-written plugin that imposes a spatially varying, angularly dependent permeability on the surface of the cell. This permeability is chosen to match the functional form previously used in the semi-analytic steady-state model of a permeable cell with a single permeable patch. That is, it is of the form:

$$P(\theta, \phi) = a + b \exp[-\delta r^2(\theta, \phi)], \tag{3.3}$$

where δ is related to the angular size of the patch, and is determined by the best fit to a discontinuous permeable patch of the same angular size θ_0; $r(\theta, \phi)$ is the great-circle distance between the point on the surface of the sphere defined by (θ, r) and the center of the permeable patch, (θ_0, ϕ_0). The parameters a and b are chosen such that the permeability at the center of the patch has the increased value P_1, whereas the permeability opposite the patch has the baseline membrane value P_2. The cell is treated by a three-component model, consisting of an interior component that represents the intracellular fluid, a component of finite thickness that represents the membrane-cell wall complex, with the diffusivity and hydraulic permeability of the cell wall, and an exterior component, roughly ten times larger than the interior, that represents the extracellular fluid. Glycerol production occurs at a constant rate α in the interior of the cell, chosen to correspond to the production rate that produces a turgor pressure of 0.2 MPa for a cell with a spatially homogeneous permeability. We generally use zero-concentration and zero-pressure conditions on the surface of the extracellular fluid domain, far from the glycerol-producing intracellular region.

We also compare this to our previous model [114], which used a semi-analytic solution through Fourier-Legendre polynomials of the equilibrium diffusion equation with an isotropic source term inside the cell to determine the steady-state behavior of a cell with a single permeable patch. We further extend this model to treat a case with an arbitrary varying permeability dependent on the angle θ, in particular the case of two permeable patches at opposite sides of the cell. Finally, we extend the previous semi-analytic model to treat the case of a time-dependent concentration.

3.3 Simulation results

One purpose of the finite element model is to provide a test of the validity of our previous semi-analytic model, which predicted the steady-state distribution of glycerol in a cell with a single permeable region as a function of radius and angle. Although we cannot accurately analyze patch sizes as small as those treated in our previous work, around 0.02 radians or 60 nm in radius, we can test the validity of this model and the previous by comparing the finite-element simulation for somewhat larger patch sizes, around 0.2 radians or 600 nm in radius, and correspondingly smaller permeabilities, about 1/10 the physical value shown in the table. The finite-element model for a single patch of angular radius 0.2 radians, the default permeability, and an initial intracellular and extracellular concentration of zero (Figure 3.1) gives a maximum steady-state concentration C_{max} of 7 mM, attained at $\theta = \pi$, opposite the permeable patch, whereas the semi-analytic model gives 7.12 mM, a difference

Parameter	**Default Value**
Diffusion coefficient, D	$1.1{\times}10^{-11}$ m^2/s
Glycerol production rate, α	10 mM/s
Patch permeability, P_1	4×10^{-2} cm/s
Cell permeability, P_2	4×10^{-6} cm/s
Cell wall rigidity, E	127 MPa
Membrane thickness, δ	10 nm
Membrane-wall hydraulic permeability, P_{hydr}	$2.17{\times}10^{-1}\mu\text{m}^4/(N \cdot s)$
Glycerol molar mass, m_{gl}	92 grams/mol
Glycerol density, m_{gl}	1.26 g/cm^3
Cell radius, R	3 microns

Table 3.1: Parameter values for time-dependent spherical cell model. The hydraulic permeability, the wall rigidity, the glycerol density, and the glycerol molar mass apply only to the finite-element model.

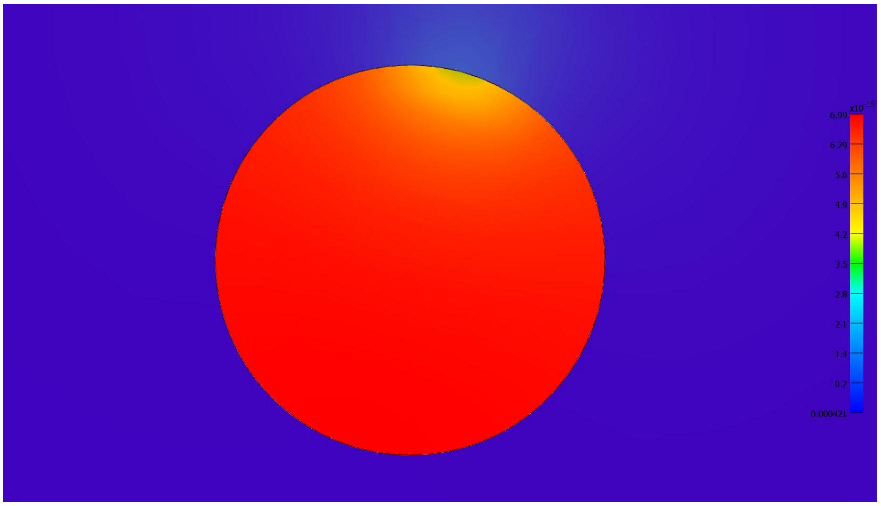

Figure 3.1: Steady-state concentration profile of cell with a single patch of angular radius 0.2 radians and default permeability at $t = 31.18$ s.

of about 2%. However, for a permeability 90% smaller, the semi-analytic model predicts a maximum concentration of 24.3 mM, whereas the finite-element model gives 26.6 mM, nearly a 10% difference.

In our previous work, we treated the case of a single permeable patch, in contrast to the more realistic situation in which multiple endocytic patches are present. The finite element analysis treats a system with an arbitrary permeability distribution on the surface of the cell. Further, the semi-analytic model with an azimuthally symmetric permeability is readily extended to a situation with two patches at opposite sides of the cell (i.e. at $\theta = 0, \pi$). Figure 3.2 shows the angular dependence of the concentration just inside the cell as predicted by the semi-analytic theory for a cell with two permeable patches of angular radius 0.2 rad and permeability $0.1P_1$, and the same dependence predicted by the finite-element model. The semi-analytic model has some noise, which is due to the error in the Fourier-Legendre series approximation. If we compare this with the results of the FEM model for the same parameters (Figure 3.3), we see that the FEM concentration profile differs by approximately 10%, suggesting some inaccuracy, but that the general shape of the profile of concentration versus angle is similar.

Figure 3.4 shows the angular dependence of the concentration difference in the semi-analytic model for the more physical case corresponding to the default permeability and angular size. We see that the larger patch sizes significantly reduce the bulk concentration. As in the case of a single patch, the dimensionless parameter P_1a/D determines the value of concentration ratios like $\delta C = C(0,0)/C(R,\pi)$, the ratio of the concentration near a patch to the concentration far from the patch; however, the dependence $\Delta C(0)/\Delta C(\pi) = f(P_1a/D)$ clearly does not hold, since the concentration difference near both patches is of course identical in the case of two patches. Moreover, the value of δC does not seem to depend on the number of patches, assuming sufficiently small

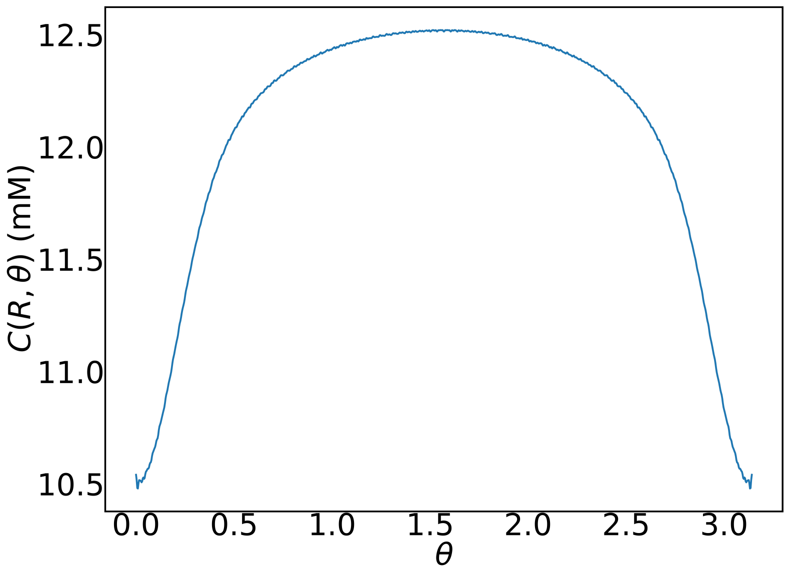

Figure 3.2: Steady-state concentration vs. angle of cell with two patches of size 0.2 radians and permeability $0.1P_1$ (semi-analytic model)

patch sizes. That is, δC is the same between, for instance, a cell with a single patch with default parameter values and one with two patches with the same parameter values, in spite of the fact that the center concentration $C(0,0)$ varies substantially with patch number. Further, the average concentration does not depend strongly on the distribution of patches: for instance, displacing the ϕ-center of a patch $\pi/4$ radians does not produce an appreciable alteration.

As mentioned above, our finite-element model also allows us to characterize how rapidly the concentration difference will be reduced after the appearance of a permeable patch, relative to the time scale of the endocytosis. For a single patch of angular radius 0.2 radians and permeability 4×10^{-3} cm/s, equal to 0.1 times the default value, the concentration at the center of the cell takes about ten seconds to equilibrate from its initial

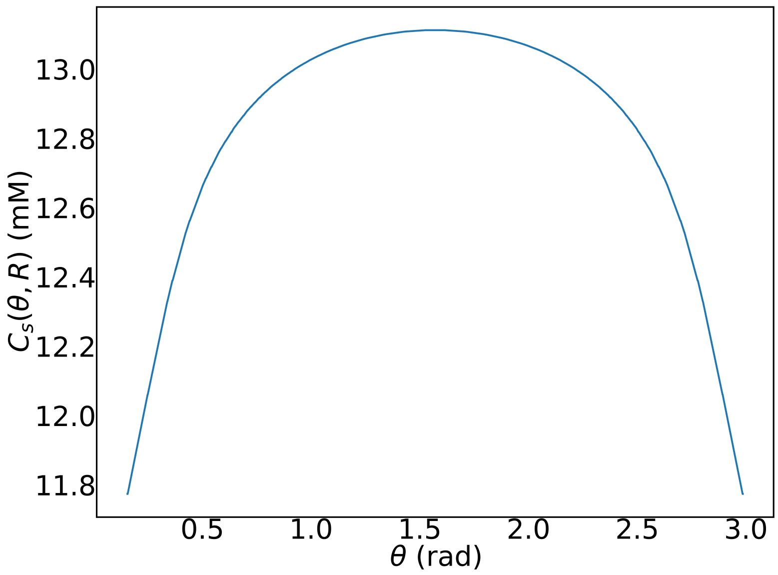

Figure 3.3: Steady-state concentration $C_s(\theta, R)$ in the FEM model vs. angle for a cell with two patches of size 0.2 radians and permeability $0.1P_1$

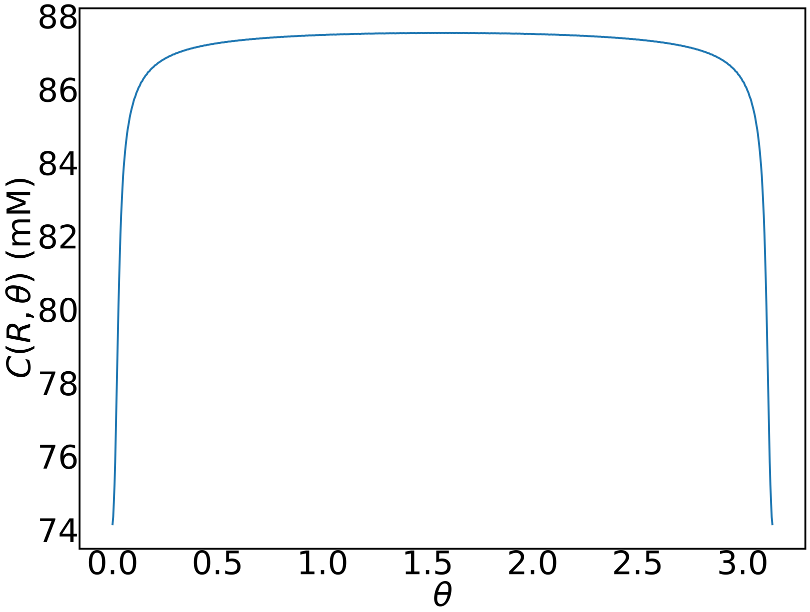

(a)

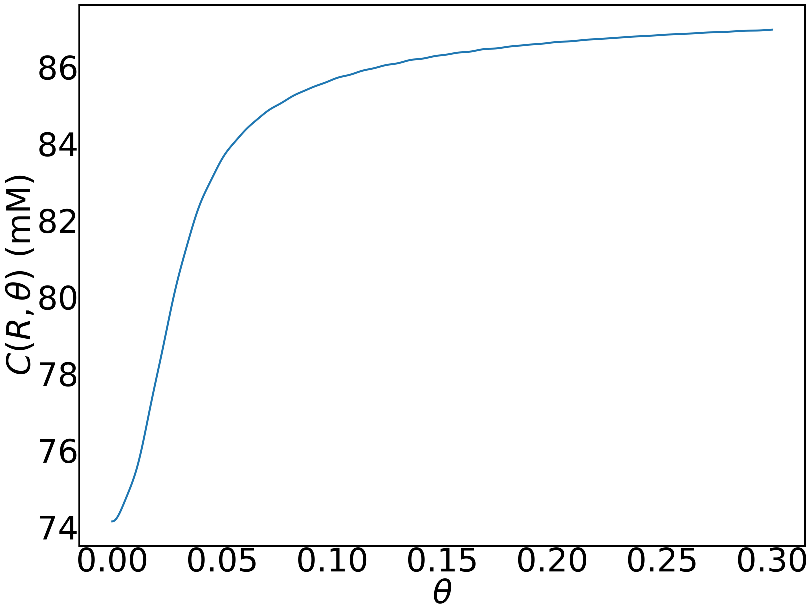

(b)

Figure 3.4: a) Steady-state concentration vs. angle of cell with two patches of default size and permeability (semi-analytic model). b) Concentration vs. angle near one of the patches for same parameter values (semi-analytic model).

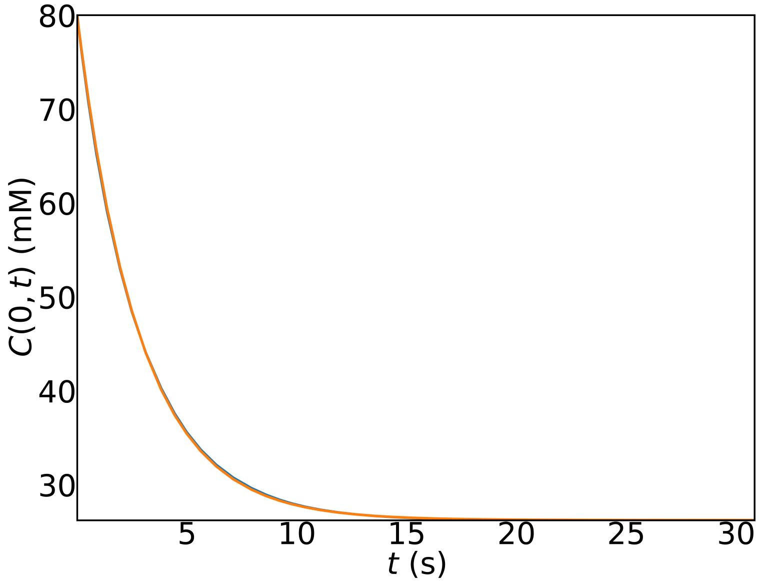

Figure 3.5: Concentration at $r = 0, \phi = 0$ (orange) and best-fit curve of the form $a + be^{-\lambda t}$ (blue) versus time for a cell with a patch of permeability $0.1P_1$ and angular size 0.2 radians (FE model)

concentration of 80 mM, corresponding to a 0.2 MPa pressure difference across the membrane, to its final steady-state concentration of 27 mM. The concentration at the center of the cell shows the same time dependence: at $t = 10$ s, it is only 5% higher than its final steady-state value (Figure 3.5). The semi-analytic solution of the reaction-diffusion equation for this case, described in Section 3.6, predicts that the concentration over time at any given point will be of the form

$$C(t) = \sum c(\lambda)e^{-\lambda t} \tag{3.4}$$

For the case of a single cell with maximum patch permeability $0.1P_1, \theta_0 = 0.2$ radians, the interior concentration is well-described by a single eigenvalue, i.e. the time dependence is of

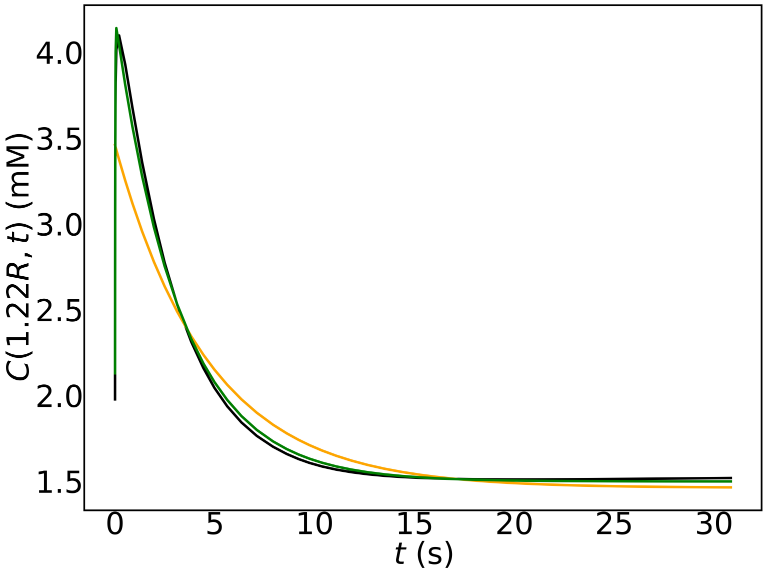

Figure 3.6: Concentration at $r = 3.65$ (black) and best-fit curves of the forms $a + be^{-\lambda t}$ (orange) and $a + b_1 e^{-\lambda_1 t} - b_2 e^{-\lambda_2 t}$ (green) versus time for a cell with a patch of permeability $0.1P_1$ and angular size 0.2 radians (FE model)

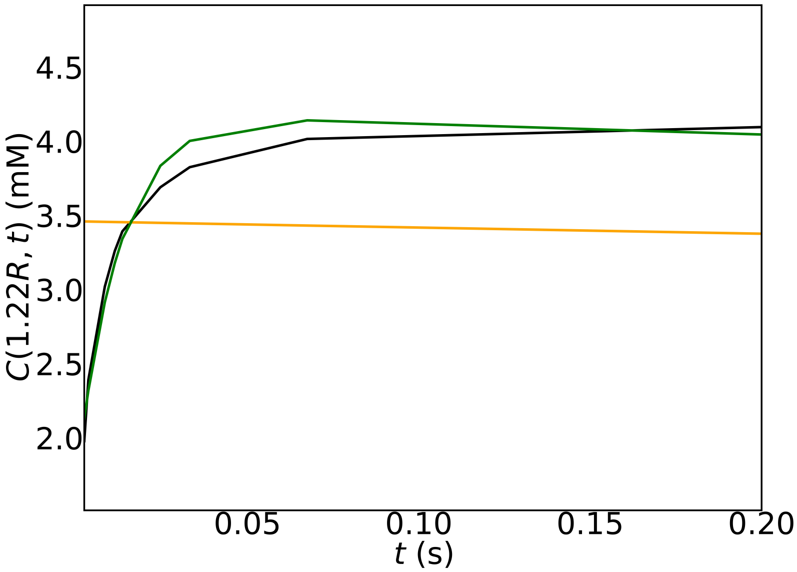

Figure 3.7: Concentration at $r = 3.65$ nm (black) and best-fit curves of the forms $a + be^{-\lambda t}$ (orange) and $a + b_1 e^{-\lambda_1 t} - b_2 e^{-\lambda_2 t}$ (green) versus time for a cell with a patch of permeability $0.1P_1$ and angular size 0.2 radians; zoom view (FE model)

the form $C(0,t) = a + be^{-\lambda t}$, as shown in Figure 3.5. This form holds for general points within the cell, i.e. for $r < R$, with a time dependence described by a single eigenvalue, $\lambda = 0.35/\mathrm{s}$. However, this description breaks down for short times at certain points outside the cell; since the external environment is relatively far from its steady-state concentration, the concentration outside the cell undergoes an initial increase for $t < 0.1$ due to permeation of solute from within the cell, whereas after this time diffusion dominates over permeation and the concentration decreases exponentially with the same time dependence as the internal concentration. In this case the concentration is well-described by two eigenvalues, i.e. $C(t) = a + b_1 e^{-\lambda_1 t} - b_2 e^{-\lambda_2 t}$ (Figures 3.6, 3.7) The initial increase corresponds to the second, larger eigenvalue λ_2 whereas the long-time behavior is described by λ_1, which is approximately the same as the interior time eigenvalue.

3.4 Conclusions

We developed a finite element model that allows for several extensions of our previous analysis of the glycerol concentration and turgor pressure distribution in a permeable cell with a single permeable patch and internal glycerol production, extending it to consider a more arbitrary angular distribution of patches, including multiple patches, as well as considering the equilibration behavior of the system. These changes render it closer to the situation in actual yeast cells. We further developed an analytic framework for an arbitrary angularly-dependent permeability (Section 3.5) and for the time-dependence of the concentration (Section 3.6).

We found that certain properties of the system are not strongly dependent on patch number; for instance, the presence of multiple patches does not change δC, the ratio of the concentration near a patch to the concentration far from a patch, which also retains its dependence on $P_1 a/D$. We further compared the semi-analytic theory and a new finite-element model and found good agreement, providing support for the consistency of both models.

We examined the time-dependent behavior of the system for a single permeable patch, finding that equilibration times are around 10 seconds after the permeability of the patch is increased, corresponding, for instance, to channel activation. This time is smaller than the timescale of endocytosis, suggesting that increasing local permeability, and the concomitant local turgor pressure reduction, could provide a viable mechanism to facilitate endocytosis. We also were able to describe the time evolution in terms of exponential decay with a small number of eigenvalues λ, although the analytic theory allows for a continuous spectrum. We thus found that the concentration outside the cell has both a permeation-dominated and diffusion dominated timescale; during the first approximately 0.1 seconds, permeation of glycerol produced within the cell dominates, whereas for longer times the removal of glycerol through diffusion is more important.

3.5 Semi-analytic theory of steady-state concentration with general angularly-dependent permeability

We can extend our model of the steady-state concentration profile of a spherical cell with a permeable patch to the case of an arbitrary permeability profile $P(\theta, \phi)$ on the surface of the cell, where θ is the polar angle and ϕ is the azimuthal angle. In this case, the system satisfies the equations:

$$\begin{gathered} D\nabla^2 C + \alpha(r) = 0 \\ \tfrac{\partial C}{\partial r}\big|_{r=R_-} = \tfrac{\partial C}{\partial r}\big|_{r=R+} \\ D\tfrac{\partial C}{\partial r}\big|_{r=R} = P(\theta,\phi)(C_{out}(r,\theta,\phi) - C_{in}(r,\theta,\phi)) \end{gathered} \tag{3.5}$$

Here "in" and "out" denote the interior and exterior solutions at $r = R$, defined limit-wise, and $\alpha(r)$ is a constant α for $r < R$ and zero otherwise.

The particular solution to this equation inside the cell is $-\frac{\alpha r^2}{6D}$. We can then write the general solution as:

$$\begin{gathered} C_{out} = \sum_{l=0}^{\infty}\sum_{m=-l}^{l} a_{ml} r^{-l+1} Y_m^l(\theta,\phi) \\ C_{in} = -\tfrac{\alpha r^2}{6D} + \sum_{l=0}^{\infty}\sum_{m=-l}^{l} b_{ml} r^l Y_m^l(\theta,\phi) \end{gathered} \tag{3.6}$$

where Y_m^l are the spherical harmonics.

The first boundary condition gives:

$$\sum_{l=0}^{\infty}\sum_{m=-l}^{l} a_{ml}(l+1)R^{-l+2}Y_m^l(\theta,\phi) = -\frac{\alpha R}{3D} + \sum_{l=0}^{\infty}\sum_{m=-l}^{l} b_{ml} r^l Y_m^l(\theta,\phi) \tag{3.7}$$

Or:

$$a_{lm}, a_{00} = \frac{l+1}{l} R^{-(2l+1)} b_{lm}, \frac{\alpha R^3}{3D} \tag{3.8}$$

We expand the permeability as a sum of spherical harmonics, i.e. $P(\theta,\phi) = \sum_{l=0}^{\infty}\sum_{m=-l}^{l} d_{ml} r^l Y_m^l(\theta,\phi)$. Then the permeability boundary condition gives us:

$$\frac{\alpha R^2}{2} + D\sum_{l_1=0}^{\infty}\sum_{m_1=-l_1}^{l_1}\left(\frac{l_1}{l_1+1}-1\right)b_{m_1 l_1}R^{l_1}Y_{m_1}^{l_1}(\theta,\phi) = \tag{3.9}$$

$$-\frac{\alpha R}{3D} + \sum_{l_2=0}^{\infty}\sum_{m_2=-l_2}^{l_2} l_2 b_{m_2 l_2} r^{l_2-1}Y_{m_2}^{l_2}(\theta,\phi)\sum_{l=0}^{\infty}\sum_{m=-l}^{l} d_{ml}r^l Y_m^l(\theta,\phi) \tag{3.10}$$

Multiplying by a third spherical harmonic $Y_{m_3}^{l_3}(\theta,\phi)$ and using orthogonality of the spherical harmonics, this becomes:

$$\sqrt{\pi}\alpha R\delta_{l_3,0}^{m_3,0} + \frac{\alpha d_{l_3 m_3}R^2}{3D} - d_{l_3 m_3}R^{l_3}\frac{1}{l_3+1} = \sum_{l_1 m_1}\sum_{l_2 m_2} l_1 b_{l_1 m_1} d_{m_2 l_2} R^{l_1-1} I_{l_1 l_2 l_3}^{m_1 m_2 m_3} \tag{3.11}$$

where

$$I_{l_1 l_2 l_3}^{m_1 m_2 m_3} = \int_0^{2\pi}\int_0^{\pi} d\theta\ d\phi \sin\theta Y_{m_1}^{l_1}(\theta,\phi)Y_{m_2}^{l_2}(\theta,\phi)Y_{m_3}^{l_3}(\theta,\phi) \tag{3.12}$$

which can be written in terms of Clebsch-Gordon coefficients as:

$$\sqrt{\frac{(2l_1+1)(2l_2+1)(2l_3+1)}{4\pi}}\begin{pmatrix} l_1 & l_2 & l_3 \\ 0 & 0 & 0 \end{pmatrix}\begin{pmatrix} l_1 & l_2 & l_3 \\ m_1 & m_2 & m_3 \end{pmatrix} \tag{3.13}$$

Although the previous solution satisfies the equation and boundary conditions, its complexity prevents its numerical evaluation for physically realistic patch sizes. In particular, while the coefficients of the azimuthally symmetric solution, $I_{l_1 l_2 l_3}$, depend on three indices that vary from 1 to a number N determined by the size of the patch, the coefficients of this general solution depend on six, that is $I_{l_1 l_2 l_3}^{m_1 m_2 m_3}$, of which three vary from $-2N$ to $2N$. For the N needed to obtain acceptable precision for the single-angle case ($N > 100$), this would require calculating over 10^{12} coefficients. However, by exploiting the symmetry of the system and the properties of the Clebsch-Gordon coefficients, this computational load could be lowered significantly: approximately 99.9% of the coefficients are zero, and the others satisfy various symmetries such as invariance under interchange of columns, evident from the definition of the integral.

3.6 Semi-analytic theory of azimuthally symmetric time-dependent concentration profile

Our previously published model deals with a steady-state situation, where the glycerol production within the cell is balanced by its outflux. As in section 3.3, we extend this model to incorporate time dependence of the concentration, in this case by using a similar semi-analytic approach to that employed for the steady-state profile. We consider a spherical cell with a spatially varying, azimuthally symmetric permeability $P(\theta)$. The interior and exterior concentration satisfy the system:

$$
\begin{gathered}
D\nabla^2 C_{in} + \alpha = \tfrac{\partial C}{\partial t} \\
D\nabla^2 C_{out} = \tfrac{\partial C}{\partial t} \\
\tfrac{\partial C_{out}}{\partial r}\Big|_{r=R_-} = \tfrac{\partial C_{in}}{\partial r}\Big|_{r=R+} \\
D\tfrac{\partial C}{\partial r}\Big|_{r=R} = P(\theta,\phi)(C_{out}(R,\theta,t) - C_{in}(R,\theta,t)) \\
C_{in}(r,\theta,0) = g_{in}(r) \\
C_{out}(r,\theta,0) = g_{out}(r)
\end{gathered}
\tag{3.14}
$$

We use the established approach of writing the solution as the sum of a particular solution of the inhomogeneous equation and a solution of the homogeneous equation that gives the correct boundary conditions. We write each concentration as the sum of a steady-state term that depends only on the spatial coordinates and a transient term:
$C_{in}(r,\theta,t) = S_{in}(r,\theta) + V_{in}(r,\theta,t), C_{out}(r,\theta,t) = S_{out}(r,\theta) + V_{out}(r,\theta,t).$

Since the boundary conditions must be valid at all times, the steady-state terms satisfy:

$$\begin{gathered} D\nabla^2 S_{in} + \alpha = 0 \\ D\nabla^2 S_{out} = 0 \\ \tfrac{\partial S_{out}}{\partial r}\Big|_{r=R_-} = \tfrac{\partial S_{in}}{\partial r}\Big|_{r=R+} \\ D\tfrac{\partial S}{\partial r}\Big|_{r=R} = P(\theta,\phi)(S_{out}(R,\theta) - S_{in}(R,\theta)) \end{gathered} \tag{3.15}$$

The solution to this is simply the concentration given by the model from our previous paper:

$$\begin{gathered} S_{out} = \tfrac{\alpha R^3}{3Dr} + \sum_{l=1}^{\infty} d_l r P_l(\cos(\theta)) \\ S_{in} = -\tfrac{\alpha r^2}{6D} + \sum_{l=0}^{\infty} \tfrac{l}{l+1} R^{2l+1} d_l r^l P_l(\cos(\theta)) \end{gathered} \tag{3.16}$$

The transient terms satisfy:

$$
\begin{aligned}
D\nabla^2 V_{in} &= \tfrac{\partial C}{\partial t} \\
D\nabla^2 V_{out} &= \tfrac{\partial C}{\partial t} \\
\tfrac{\partial V_{out}}{\partial r}\Big|_{r=R_-} &= \tfrac{\partial V_{in}}{\partial r}\Big|_{r=R+} \\
D\tfrac{\partial C}{\partial r}\Big|_{r=R} &= P(\theta,\phi)(V_{out}(R,\theta,t) - V_{in}(R,\theta,t)) \\
C_{in}(r,\theta,0) &= g_{in}(r) - S_{in}(r,\theta) \\
C_{out}(r,\theta,0) &= g_{out}(r) - S_{out}(r,\theta) \\
V_{out}(R_{max},\theta) &= 0
\end{aligned}
\tag{3.17}
$$

The interior and exterior transient equations are identical. We seek a solution to this equation of the form $C(\mathbf{r},t) = \Psi(\mathbf{r})T(t)$. This gives, by separation of variables:

$$(1/))D\nabla^2\Psi = (1/T)\frac{\partial T}{\partial t} = -\lambda \tag{3.18}$$

where λ is a positive, real separation constant to ensure boundedness at infinite time.

The solution of the temporal component is $T(t) = ce^{-\lambda t}$. The spatial portion becomes

$$\nabla^2\Psi = (1/T)\frac{\partial T}{\partial t} = -(\lambda/D)\Psi \tag{3.19}$$

which we recognize as the Helmholtz equation, whose azimuthally symmetric solutions are

$$\Psi_l(r,\theta) = \big(a_l j_l(\sqrt{\lambda/D}r) + b_l y_l(\sqrt{\lambda/D}r)\big)P_l(\cos\theta) \tag{3.20}$$

The functions j_l, y_l are the spherical Bessel functions of the first and second kinds respectively and the P_l are the Legendre polynomials. Separating the eigenfunctions into interior and exterior components, and noting that the interior solution cannot contain y_n

due to the latter being non-finite at $r = 0$, we have:

$$\begin{aligned} \Psi_{in,l} &= a_l(\lambda) j_l(\sqrt{\lambda/D} r) P_n(\cos\theta) \\ \Psi_{out,l} &= b_l j_l(\sqrt{\lambda/D} r) + e_l y_l(\sqrt{\lambda/D} r)) P_l(\cos\theta) \end{aligned} \tag{3.21}$$

where we have arbitrarily chosen the coefficient of the interior Ψ to be 1.

Applying the derivative continuity condition, we have

$$a_l(\lambda) j_n'(\sqrt{\lambda/D} r) = b_{mn} j_n'(\sqrt{\lambda/D} r) + e_{mn} y_n'(\sqrt{\lambda/D} r) \tag{3.22}$$

which gives us $b_l(\lambda) = a_l(\lambda) - \varphi_l(\lambda) e_l(\lambda)$ for $\varphi_l(\lambda) = y_l'(\sqrt{\lambda/D} R)/j_l'(\sqrt{\lambda/D} R)$. The permeability condition mixes together different values of l, and thus cannot be imposed on the individual eigenfunctions $\Psi_{in,l}$ but rather applies to the sum $\sum\limits_l \Psi_l$. That is, at $r = R$,

$$P(\theta) \sum_l (\Psi_{in,l} - \Psi_{out,l}) = D \frac{\partial}{\partial r} \sum_l \Psi_{in,l} \tag{3.23}$$

We expand the permeability as $P(\theta) = \sum\limits_k f_k P_k(\cos\theta)$, giving us

$$\sum_k \sum_l P_k(\cos\theta) P_l(\cos\theta) f_k e_l(\lambda) [y_l(\sqrt{\lambda/D} R) - \varphi_l j_l(\sqrt{\lambda/D} R)] = \sum_l a_l(\lambda) \sqrt{D\lambda} j_l'(\sqrt{\lambda/D} R) P_l(\cos\theta) \tag{3.24}$$

Multiplying by $P_n(\cos\theta)$, substituting in Equations 3.21 and 3.22, and using orthogonality of the Legendre polynomials, this becomes

$$\frac{2}{2n+1} a_n(\lambda) \sqrt{D\lambda} j_n'(\sqrt{\lambda/D} R) = \sum_n \sum_l \nu_l(\lambda) I_{kln} f_n e_l(\lambda) \tag{3.25}$$

where $I_{kln} = \int\limits_{-1}^{1} dx P_k(x) P_l(x) P_n(x)$ and

$$\nu_l(\lambda) = y_l(\sqrt{\lambda/D}R) - \varphi_l j_l(\sqrt{\lambda/D}R) \tag{3.26}$$

This is a set of equations that defines $a_l(\lambda)$ in terms of $e_k(\lambda)$ for all λ, k, l.

We can then write the general solution as

$$\begin{aligned} V_{out} &= \int d\lambda\lambda \sum_l \Psi_{out,l}(\mathbf{r}) e^{-\lambda t} \\ V_{in} &= \int d\lambda\lambda \sum_l \Psi_{in,l}(\mathbf{r}) e^{-\lambda t} \end{aligned} \tag{3.27}$$

Note that any prefactor $c(\lambda)$ in these solutions can be incorporated into the coefficients $a_l(\lambda)$ etc.

The initial conditions are:

$$V_{in}(r,\theta,0) = \int d\lambda\lambda \sum_l \Psi_{out,l}(\mathbf{r}) = g_{in}(r) - S_{in}(r,\theta), \tag{3.28}$$

and similarly for V_{out}. We can write the conditions for V_{in}, V_{out} in a single line as:

$$V(r,\theta,0) = \int d\lambda\lambda \sum_l \Psi_l(r,\theta) = g(r) - S(r,\theta), \tag{3.29}$$

where for instance $\Psi_l(r,\theta) = \Psi_{in,l}(r,\theta)$ for $r < R$ and $\Psi_{out,l}(r,\theta)$ for $r > R$ and similarly for the other functions. If we choose the interior and exterior initial conditions to be exactly equal to the angular component of the steady-state concentration $S(r,\theta)$, this becomes:

$$\int d\lambda\lambda \sum_l \Psi_l(r,\theta) = h(r) \tag{3.30}$$

for a function $h(r)$ equal to the radial term in the initial conditions. Using orthogonality of $P_k(\cos(\theta))$, this becomes:

$$\frac{2}{2l+1}\int d\lambda\lambda\Psi_{r,k}(r) = h(r) \tag{3.31}$$

for all k, where $\Psi_{r,l}$ is the radial component of the eigenfunction and $h(r)$ is the appropriate initial data, or:

$$\Psi_{r,l} = \begin{cases} a_l j_l(\sqrt{\lambda/D}r) \quad r < R \\ [a_l(\lambda) - \varphi_l(\lambda)e_l(\lambda)]j_l(\sqrt{\lambda/D}r) + e_l y_l(\sqrt{\lambda/D}r) \qquad\qquad r > R \end{cases} \tag{3.32}$$

When combined with Equation 3.25 this determines $\mathrm{a}_l(\lambda)$.

Chapter 4

Force Generation by Curvature-Inducing Molecules in Cells with Turgor

4.1 Introduction

The previous chapters have treated the origins of the forces opposing the central process of clathrin-mediated endocytosis [87]. This process involves the invagination of a portion of the cell membrane, driven by curvature-generating proteins (CGMs) and in many cases the the polymerization of actin. Under some conditions, the dimple eventually lengthens and pinches off into a free vesicle which moves into the cell. CME has been observed in many biological systems, from animal cells to yeast cells [80] and plant cells [26], in processes varying from viral transport [102] to mammalian nervous activity [62, 92]. Forces opposing endocytosis include the bending rigidity of the membrane, surface tension, and (in some types of cells) turgor pressure.

CGMs play a key role in CME, as well as in various other processes in a wide variety of cells, such as cell-cell fusion and curvature sensing [74, 109]. Among those with a role in CME, the most studied is clathrin, which has been shown to sense and influence membrane curvature, and likely plays a critical role in generating curvature and even forces [57]. However, other curvature-generating proteins can also affect endocytosis [65]. For example, BAR-domain proteins, which induce an asymmetric curvature [119, 131], have been shown to colocalize with clathrin-coated pits [117]. They can also affect endocytosis in a variety of ways, for example by stabilizing or destabilizing the invagination, potentially leading to pinch-off in later stages [138]. Epsin contributes to CME [30, 91] , possibly by inducing a high degree of curvature in conjunction with clathrin [98]. Curvature may also be induced by other factors, such as the presence of curved lipids asymmetrically distributed between the two leaflets of the lipid bilayer [58], or hydrophobic insertion [132]. In addition, protein crowding, in which a curved membrane favors greater numbers of attached proteins than a flat membrane, may be important [127].

CME in yeast presents additional challenges not present in, for example, mammalian cells, due to the presence of a high turgor pressure and a stiff cell wall. The primary barrier to yeast endocytosis is the turgor pressure [1], which may attain values as high as 0.6 MPa in budding yeast [113] and 1 MPa in fission yeast [12]. We use 0.2 MPa as a baseline value, since this value was determined from very rapid indentor experiments, rather than from slower osmotic shock experiments, which may trigger osmoregulation that confounds the experiment [45]. This turgor pressure is continuously generated by osmolytes, primarily glycerol [99], and is balanced by the high yield strength of the cell wall. If the applied pressure on the cell wall exceeds its stiffness, it will rupture [124]. In order to withstand the turgor pressure, the yeast cell wall is stiffened by agents such as chitin and β-glucan [3, 143] .

Previous simulations of actin growth suggest that actin can generate a maximum useful force of up to 360 pN [22], which can effectively cancel out a substantial portion of the turgor pressure. When spread over a region corresponding to our default CGM radius of 36 nm and area of 3300 nm^2 for a hexagonal patch with amputated corners, this corresponds to a pressure of approximately 0.11 MPa directed out of the cell, reducing the pressure that must be overcome by the CGMs from 0.2 MPa to 0.09 MPa.

Some previous estimates have found that CGMs lack the ability to overcome turgor pressure on the scale of that in yeast [33]. As an first estimate of the CGMs' force-generating capability, we consider a flat patch of area A, composed of CGMs of intrinsic curvature C_0 with bending rigidity κ; it will preferentially form a spherical cap corresponding to a sphere of radius $R_0 = 1/C_0$ and height $\frac{A}{2\pi R_0}$, since there is no stretching and thus the surface area remains constant. The energy of this system is:

$$U = 2\kappa \int dA \Big[\big(C - C_0\big)^2 + \sigma \Big] + \int dV \Pi \tag{4.1}$$

Thus the bending energy difference between the flat and curved states is $2\kappa A C_0^2$, the turgor pressure energy difference is zero since the area stays constant, and the turgor pressure energy difference is $\Pi V_{curved} = \frac{1}{12}\frac{\Pi A^2}{\pi R_0^2}(3R_0 - \frac{A}{2\pi R_0})$, which leads to an estimate of the maximum turgor pressure that can be overcome by CGMs as

$$\Pi_{max} = \frac{24\pi\kappa}{A(3C_0^{-1} - \frac{AC_0}{2\pi})} \tag{4.2}$$

In particular, for our hemispherical clathrin patch of radius $A = 3273$ nm, intrinsic curvature $C_0 = 0.02/\text{nm}$, and bending rigidity $300 k_b T$,[64] this is roughly equal to the turgor pressure, 0.2 MPa. Thus, it would appear that the CGMs could almost overcome the turgor pressure by themselves. In addition, Π_{max} is enhanced by κ and C_0, but reduced by increasing A.

Several previous theoretical works have looked at the effects of CGMs on membrane bending [29, 33, 43, 50, 108, 111, 138]. Much of this has dealt with the specific case of clathrin. These models have often found that clathrin by itself can produce an invagination [43]. Other models of clathrin bending have utilized a wide variety of mechanisms, including equilibrium, dynamic, and stochastic approaches [2, 61]. There also exist models incorporating the effects of epsin [18], BAR domain proteins, and other curvature generators. These works have characterized various features of CME, such as the balance between surface tension and curvature generation, and the presence of instabilities in invagination shape.

However, such models have often neglected the influence of the high turgor pressure present in yeast. Some models have either modeled only turgor pressure and not the cell wall force, and thus simply restricted the position of the membrane to be above the cell wall [33]. In other cases, they have approximated the turgor pressure energy with a simplified quadratic form, or modeled the cell wall as infinitely hard [89]. This does not take into account the nearly discontinuous effects caused by presence of the cell wall, and can also be a major source of inaccuracy, since the cell wall stiffness is much higher than the turgor pressure (approximately 80-250 times the magnitude). In this paper, we address this issue with an energy function that shows a smooth, but nonetheless rapid force transition as the membrane presses into the wall. This allows us to correctly treat the approximately linear form of the turgor pressure energy as a function of displacement, while simultaneously considering a cell wall interaction that is essentially a contact force.

Many previous models have used functional minimization of the continuous Helfrich energy [52], applied to CGMs, to calculate membrane shapes. While this has the benefit of computational speed and ease of understanding, and occasionally admits analytic solutions, it obscures effects from the physical discreteness of CGM molecules. For example, bending moments in continuum models correspond to pairs of forces in discrete models, which could have measurable effects in a biological system.

We seek to understand the strength and distribution of forces generated by CGMs and their dependence on key interaction parameters. To this end, we develop a discrete model of interacting CGM molecules subject to a high turgor pressure and bounded by a stiff cell wall. The CGMs also interact with an idealized lipid bilayer membrane, which is modeled according to Helfrich membrane theory. We use energy minimization algorithms to find the equilibrium state of the CGM system. We also look at a simple continuous model of a CGM-covered membrane in a potential with quadratic and linear components, corresponding to the cell wall force when in contact and to turgor pressure respectively. The resulting discrete-model shapes agree well with continuous models of the shape for low turgor pressure, but diverge more for high turgor pressure. We observe several discontinuous transitions in the force and CGM height as a function of key physical parameters, corresponding to the CGM patch overcoming turgor pressure and lifting off from the cell wall. We find that the CGMs alone are sufficient to overcome about half of the turgor pressure, and are sufficient to overcome the full turgor pressure once the actin contribution is considered. Additionally, the force distribution predicted by the model is compared to previous continuous estimates of the force distribution, showing moments at the edges rather than a spread-out force for large enough areas. Finally, we note that the presence of a preferred molecular number can follow from an appropriate attractive interaction.

4.2 Materials and Methods

4.2.1 Discrete model

In developing a discrete model, one is faced with a choice of molecule shapes. CGMs and other curvature-inducing molecules vary widely in shape, from the triskelial shape of clathrin [73] to the more linear shape of BAR domain proteins, or the rod-like shape of curvature-inducing lipids. These shape differences induce some protein-specific effects on CGM assembly and curvature induction, as for example the interactions between different portions of clathrin legs. For maximum generality, we do not treat these in our model, considering instead a simple shape that leads to curvature, rod-like CGMs with different preferred top and bottom spacings. This simplification leads to some limitations, since it does not consider any of the specific shape or chemistry-influenced interactions of actual proteins, but we argue below that our results are generally applicable.

We calculate the equilibrium shape of a collection of rod-shaped CGMs whose centers are arranged in a hexagonal lattice in a system with a high turgor pressure and a stiff cell wall, as shown in Figure 4.1. The molecules interact through their tops, bottoms, and centers. The membrane is assumed to follow the motion of the bases of the CGMs whereas the cell wall reacts to the CGM forces transmitted through the membrane according to elastic theory.

We assume that the CGM energy is of the form:

$$U = U_{CGM} + U_{\Pi} + U_w + U_m + U_a \tag{4.3}$$

Figure 4.1: Schematic of model, showing membrane with attached CGMs and the cell wall. The turgor pressure is Π, and the strength of the interaction with the cell wall is k_w. The top and bottom preferred distances are $a + \epsilon$ and a respectively, with an interaction spring constant k_b.

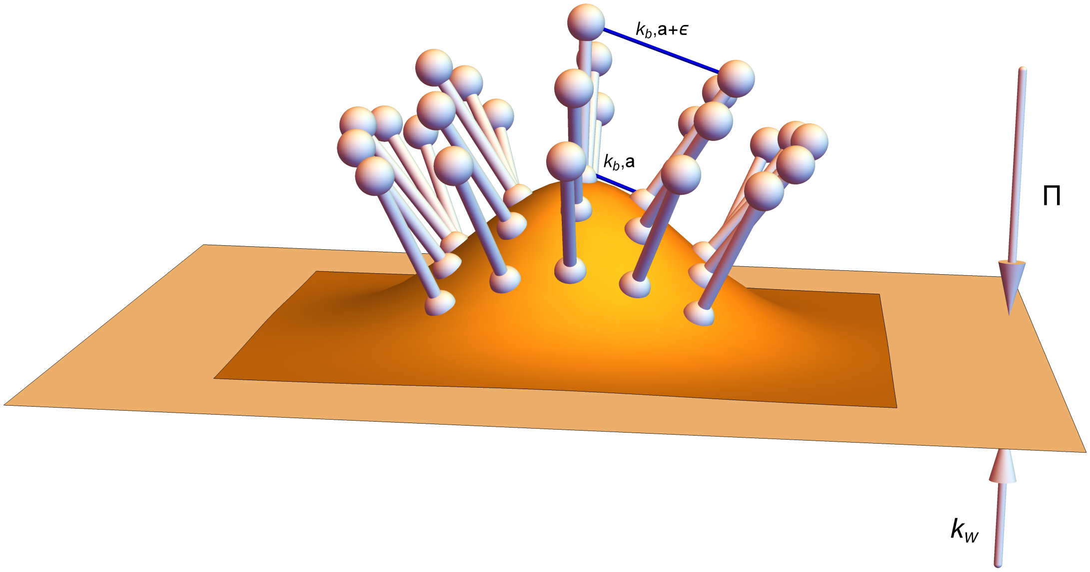

Here U_{CGM} is the energy due to curvature-generating proteins, U_{Π} is the energy due to the turgor pressure, U_w is the energy due to the interaction with the cell wall, U_m is the energy of the lipid membrane beyond the CGM region (including cell wall interactions) and U_a is a number-dependent attractive term.

The interaction energy due to the curvature generating proteins is

$$U_{CGM} = \frac{1}{2}\sum_{\langle ij\rangle} k_b \left\{[d_{ij,top} - (a+\epsilon)]^2 + [d_{ij,bottom} - a]^2\right\} + \frac{1}{2}k_c(\mathbf{d}_{ij,cen} \cdot \mathbf{e}_{ij})^2. \tag{4.4}$$

Here $\mathbf{d}_{ij,cen}$ is the displacement vector between the centers of molecules i and j (and similarly for $\mathbf{d}_{ij,top}$ and $\mathbf{d}_{ij,bot}$. The preferred distances of the tops and bottoms of the molecules are $a + \epsilon$ and a respectively. Thus the first two terms in the CGM energy are responsible for the intrinsic curvature of the membrane-CGM complex. In addition, $\mathbf{e}_{ij}$ is the average of the orientation vectors of the two interacting molecules. Thus this last term is a shear energy, which prevents the centers of the molecules from slipping relative to each other. The strength of the bending energy is given by k_b, and the strength of the anti-slipping interaction is given by k_c.

We assume a constant turgor pressure force, leading to a linear term in the energy, of the form

$$U_{\Pi} = \sum_i \frac{\Pi A}{N} z_{i,bot} \tag{4.5}$$

Here A is the projected area in the x-y plane (the local plane of the membrane and the cell wall) and N is the number of molecules. We consider CGM profiles that are close to flat, such that the pressure acts vertically and each molecule can be assumed to have equal molecular area.

The elastic interaction between the CGMs and the cell wall has two terms, both derived from linear elastic theory (see Section 4.7): direct interaction of a molecule with the membrane, and the force experienced by one molecule due to the interaction of the membrane with neighboring molecules.

$$U_w = \frac{1}{2}(k_0 + 6k_1)\sum_i \{z_{i,bot}^2[1 - H(z_{i,bot})]\}^2 - \frac{1}{2}k_1 \sum_{\langle ij \rangle} z_{i,bot}z_{j,bot}(1 - H(z_{i,bot}))(1 - H(z_{j,bot})) \tag{4.6}$$

Here k_0 and k_1 are defined in terms of the cell wall thickness t and the CGM lattice parameters by equation 4.13, and $H(z)$ is the unit step function. The $H(z)$ factors restrict the elastic terms to $z > 0$.

The attractive number-dependent energy, describing binding between neighboring CGMs, has the form:

$$U_a = -\sum_{\langle ij \rangle} k_a, \tag{4.7}$$

where k_a is an unknown constant. Since this term does not have any coordinate or angle dependence, it only influences the number dependence of the energy, and not the minimum-energy structure for a given number.

Finally, we model the lipids outside the CGM layer according to the Helfrich membrane theory (Section 4.8). In the region with CGMs ($r < R_{CGM}$), where R_{CGM} is the maximum radius of the hexagonal CGM array before corner regularization, the membrane is considered bound to the CGMs and is not treated explicitly. Outside this region, it is subject to a surface tension σ, a bending rigidity κ_b, and a wall potential κ_w, as well as the turgor pressure Π. Since CGMs are absent on the bare portion of the membrane, the membrane height $z(r)$ obeys equation 4.19 for zero intrinsic curvature, and thus has a solution given by 4.21.

The height and slope must be continuous at the interface between the CGM network and the membrane, and the membrane profile must decay to zero at infinity. Thus equations 4.21, 4.22 become $z(r) = a_3 K_0(c_1 r) + a_4 K_0(c_2 r)$, where a_3, a_4 may be complex, and satisfy $a_3 K_0(c_1 R) + a_4 K_0(c_2 R_{CGM}) = z_{CGM}(R_{CGM}), a_3 K_1(c_1 R_{CGM}) + a_4 K_1(c_2 R_{CGM}) = z'_{CGM}(R_{CGM})$, where the second equation is the derivative continuity condition.

Here $z'_{CGM}(R_{CGM})$ is the average CGM orientation, given by $z'_{CGM}(R_{CGM}) = -\sum\limits_{boundary} \tan(\phi)\cos(\theta - \theta_g)$, where the global radial angle is given by $\theta_g = \arctan(y/x)$, taking the quadrant into consideration. Here x, y are the coordinates describing the position of the center of a CGM in the plane defined by the cell wall, and θ, ϕ are respectively the azimuthal and polar angles describing the orientation of the rod-shaped CGM molecule.

From the membrane profile, we obtain the membrane energy resulting from its interaction with the CGMs:

$$U_m = \int\limits_S dS[2\kappa C^2 + \sigma + \frac{1}{2}k_w z^2 + \Pi z] \tag{4.8}$$

Here the height profile $z(r)$ is determined by the boundary conditions given by $z(R_{CGM})$ and $z'(R_{CGM})$, and the integration is taken from R_{CGM} to an appropriately distant cutoff radius (10,000 nm).

The total energy is numerically minimized for various choices of parameters and numbers of molecules through descent algorithms (conjugate gradient and trust-NCG methods).

Our baseline number of molecules is 121, with a height of 10 nm and a preferred bottom spacing of 6 nm and top spacing of 7.5 nm, and with the total area of the molecules, 3300 nm^2, roughly corresponding to measured sizes of clathrin patches.

4.2.2 Continuous model of CGMs

For the purpose of comparison, we also examine a simple continuous model of CGM-membrane bending in the presence of a wall and turgor force. This corresponds to equation 4.19 for the case of non-zero intrinsic curvature. The model treats the region of the membrane covered by CGMs. It is thus subject to the following boundary conditions, derived from the general boundary conditions in Section 4.8:

$$\begin{gathered}
z'(0) = 0 \\
z'''(0) = 0 \\
\tfrac{1}{R} z'(R) + z''(R) = C_0 \\
(\tfrac{1}{R} + \xi^2 R) z'(R) - R z''(R) - z'''(R) = 0
\end{gathered} \tag{4.9}$$

This allows for a second estimate of the effect of the inclusion of the membrane on the CGM height and force profile. This model, however, does not take into account the effect of the CGM-free membrane region.

4.3 Results

The default parameter values are given in Table 4.1. We analyze the CGM behavior for a variety of parameters; however, our default values correspond to those typical of yeast endocytosis. For instance, the cell wall stiffness comes from direct measurements of yeast cell walls, the turgor pressure comes from values determined by AFM indentation

Parameter	**Default value**
Patch dimension, D	6
Molecule height, l	10 nm
Area, A	3300 nm^2
Bending rigidity, κ	300 k_BT [64]
Cell wall stiffness, G	50.8 MPa [124]
Cell wall potential coefficient, k_w	0.00127 J/nm^4
Poisson ratio, ν	0.25
Attractive interaction, k_a	0 k_BT
Bending coefficient k_b	2.3×10^{-3} kg/s^2
Anti-slipping interaction, k_c	2.3×10^{-3} kg/s^2
Preferred top spacing, d_1	7.5 nm
Preferred bottom spacing, d_2	6 nm
Difference between spacings, ϵ	1.5 nm
Intrinsic curvature, C_0	0.02 per nm [64]
Turgor pressure, Π	0.2 MPa or 0.09 MPa (actin force incorporated)
Membrane stiffness, κ_m	30 k_BT [64]
Membrane preferred position, z_0	-0.15 nm
Membrane surface tension, σ	0.0005 N/m

Table 4.1: Parameter values for the discrete and continuous CGM models. For parameters that are varied we give the default values.

experiments, and the CGM bending rigidity comes from measurements of clathrin-coated vesicles, as does the intrinsic curvature. Some values are more uncertain, however: for instance, the value of the membrane surface tension is unknown. We have chosen the patch size to roughly match the measured size of endocytic invaginations, and the molecular length to be close to the thickness of the clathrin coat. The intermolecular interaction coefficient k_b was determined by equating the calculated energy of a flat patch with the known formula $\frac{1}{2}\kappa C_0^2 A$, and the difference between the preferred top and bottom distances, ϵ, was chosen so that the tops of two molecules located and oriented at their preferred distances would intersect at a length, equal to C_0^{-1} , thus ensuring that an array of such molecules would have an average radius approximately equal to the radius of curvature.

At the physically realistic turgor pressure of 0.20 MPa, the CGM-membrane complex is mostly flat, with the center pressed into the cell wall ($z = -0.0367$), while the maximum height (attained near the edges) is $z = 0.144$ (Figure 4.2a). The profile for the corresponding k_w in the continuous model is much higher (Figure 4.2b).

The presence of the part of the lipid bilayer membrane outside of the CGM shell, as modeled by the Helfrich energy contribution, has a substantial effect on these profiles, and thus on the depth of the indentation that the CGMs can generate. At the reference turgor pressure of 0.2 MPa, the inclusion of the membrane energy produces a 20% reduction in the maximum height of the CGM bottoms, z_{max}, relative to the membrane-free system, and a 16% reduction in the vertical extent of the CGMs, $z_{max} - z_{min}$; further, at zero turgor, the membrane causes an 12% reduction in z_{max} and a 23% reduction in the vertical extent. The CGM forces for high turgor pressure are mainly distributed at the edges, in the form of bending moments. This corresponds to the results predicted by the continuous model, which predict only bending moments (and no forces) for a flat, intrinsically curved membrane.

By contrast, for low turgor pressure (Figures 4.3), the shape is determined primarily by the intrinsic curvature of the CGMs. For a radius of curvature of 50 nm, the maximum displacement of the center of the CGM patch is about 10.5 nm (Figures 4.3b, 4.3a), which it attains in the limit of zero turgor pressure.

At low turgor pressure, the majority of the CGMs are not in contact with the cell wall, and so the force distribution is essentially flat, balancing the turgor pressure (Figure 4.4a), with opposing forces at the edge where the molecules press into the wall. As the turgor pressure increases, the center of the CGMs buckles, causing a dip to appear in the CGM profile and the force profile (Figure 4.4b). Eventually, at very high turgor pressure (greater than 0.2 MPa or so), this dip spreads out laterally, such that only the edges of the CGMs are substantially above the cell wall (Figure 4.2a), with the forces (Figures 4.5a, 4.5b) effectively being concentrated at the edges in the form of bending moments.

This is reasonably similar to the form of the CGM forces predicted by previous models. For example, Tweten et al. derived forms for the force resulting from several continuous CGM profiles [135]. One of their force profiles had the form $\frac{\kappa_b \gamma H_0}{s}\mathrm{sech}^2[\gamma(r-r_0)](\gamma s \tanh[\gamma(r-r_0)]-\frac{1}{2})$, shown in Figure 4.5a for several values of γ.

The profiles in Figures 4.4, 4.5 suggest that CGMs can produce a substantial force density, comparable to the turgor pressure. The maximum turgor pressure that can be overcome by a given CGM force density, Π_{max}, is defined as the pressure at which the center of the CGM patch shows appreciable (5%) liftoff relative to its maximum (zero-pressure) height. An energetics calculation based on comparing the bending energy and the turgor pressure energy for a flat configuration and one at the preferred curvature C_0, respectively (Equation 4.2), predicts that at default parameter values $\Pi_{max} = 0.2$ MPa. This equation is based on a membrane-free calculation, so it may not predict the correct prefactors. It also predicts a linear dependence on bending rigidity κ, and an area dependence of the form $[\frac{A}{\pi}(3C_0^{-1} - \frac{AC_0}{2\pi})]^{-1}$, or proportional to $1/A$ for small AC_0^2. Figures 4.6, 4.7 show that it overestimates Π_{max} by about a factor of 2. However, the general form of the area dependence of the simulations is approximately $\Pi_{max}(\kappa) \propto 1/A$ for larger areas (Figure 4.6), and $\Pi_{max}(\kappa)$ is fairly linear over a wide range of bending rigidities (Figure 4.7).

The discrete CGM model also allows us to ascertain the parameter dependence of the central force and total pulling force for CGM patches of various parameter values, as well as their profiles.

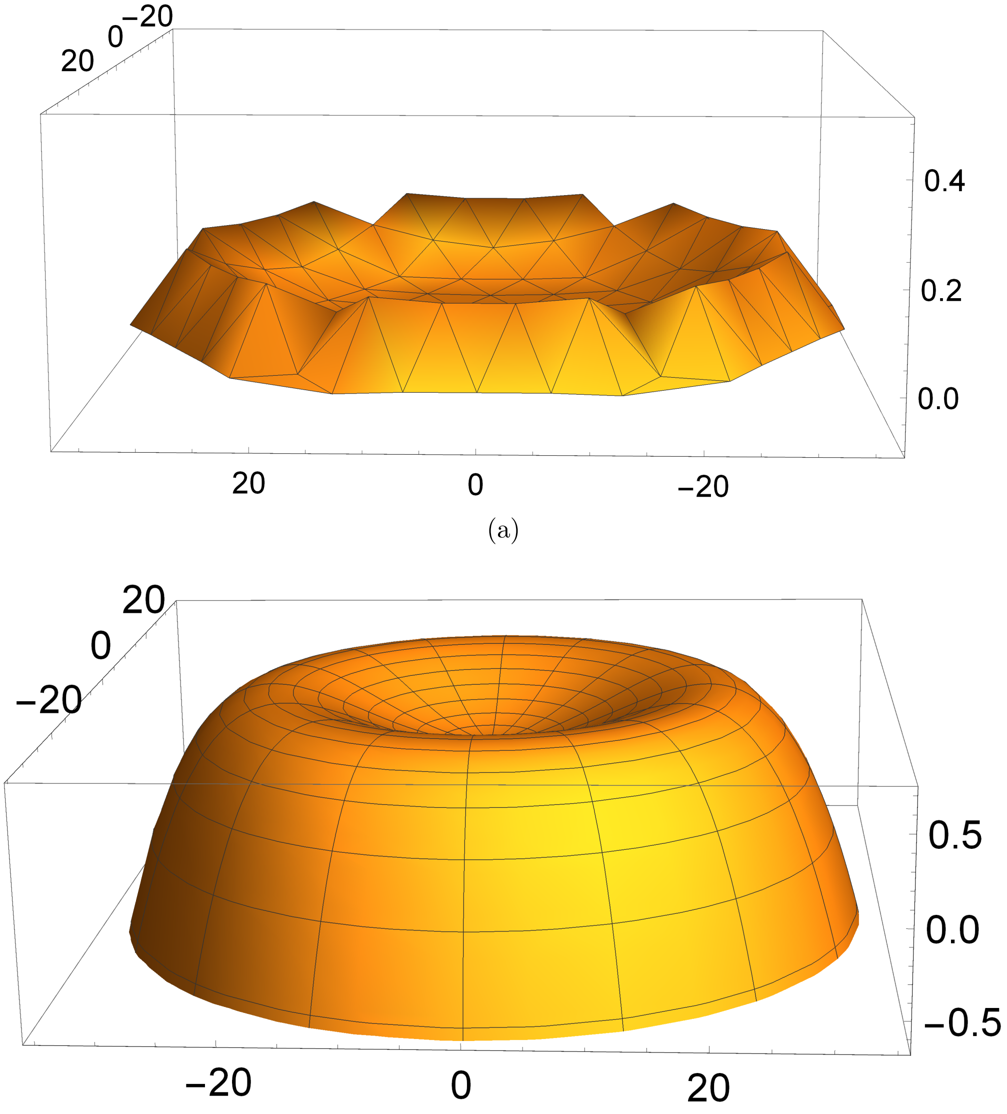

(a)

(b)

Figure 4.2: a) Clathrin network profile for $k_b = 0.002296$ kg/s, $G = 50.8$ MPa, $\Pi = 0.2$ MPa (high turgor pressure case). b) Continuous membrane profile for $\kappa = 300 k_B T$, $\kappa_w = 0.00127\, J/\mathrm{nm}^4$, $\Pi = 0.2$ MPa (high turgor pressure case).

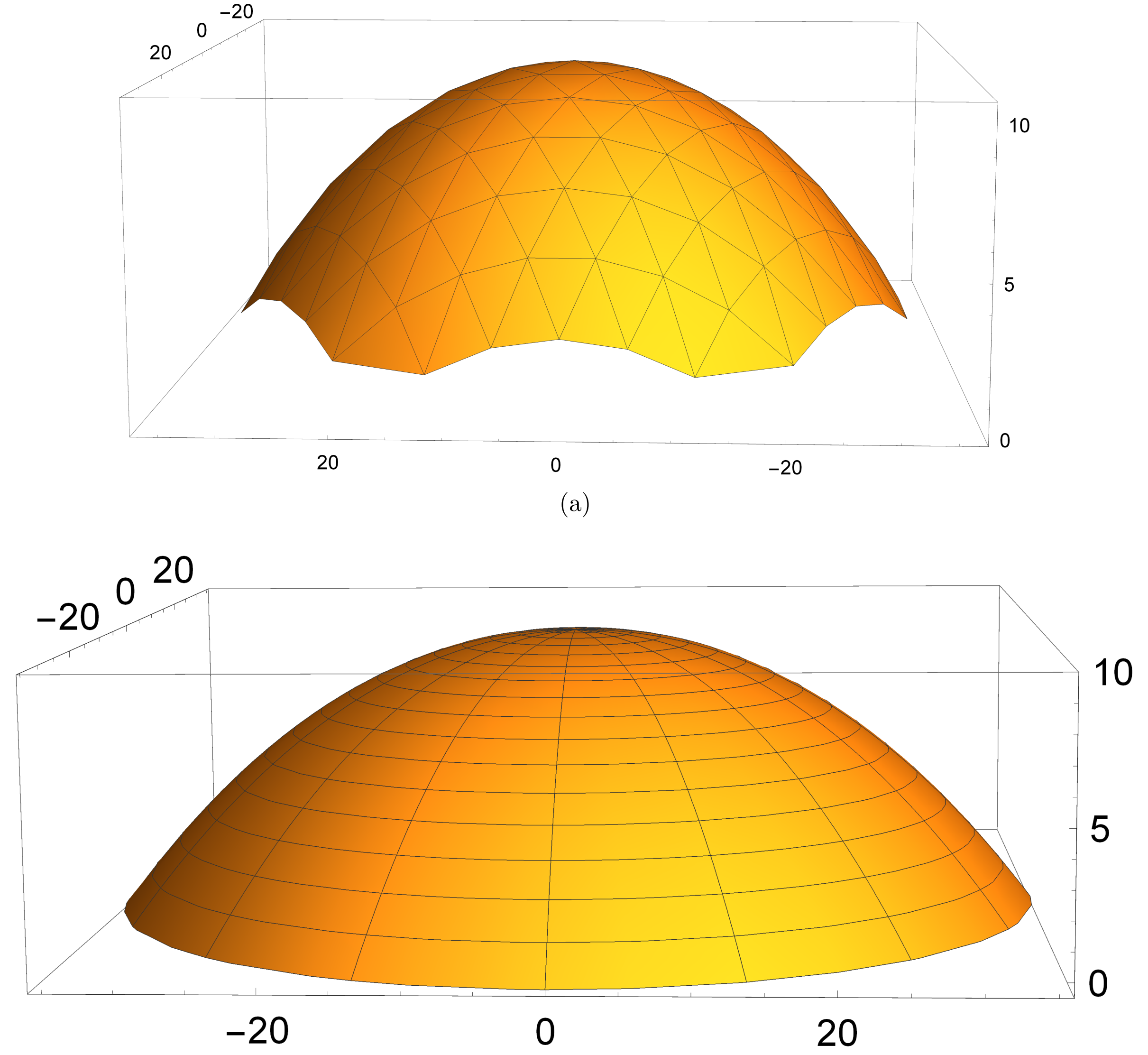

(a)

(b)

Figure 4.3: a) Discrete model network profile for $k_b = 0.002296$ kg/s, $G = 50$ MPa, $\Pi = 0.00002$ MPa (low turgor pressure case). b) Continuous profile for $\kappa = 300 k_B T$, $\kappa_w = 0.00127\, J/\text{nm}^4$, $\Pi = 0$ MPa (low turgor pressure case).

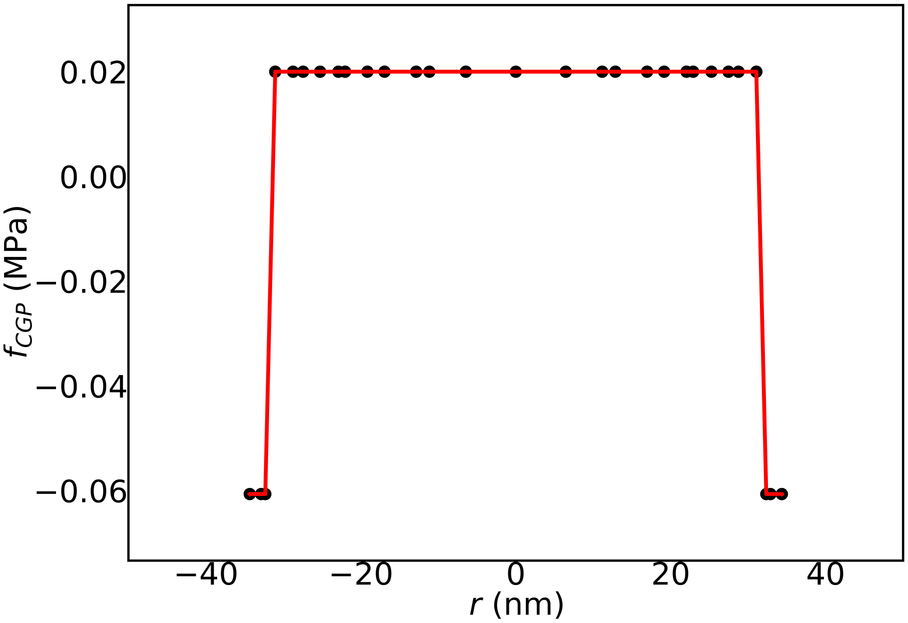

(a)

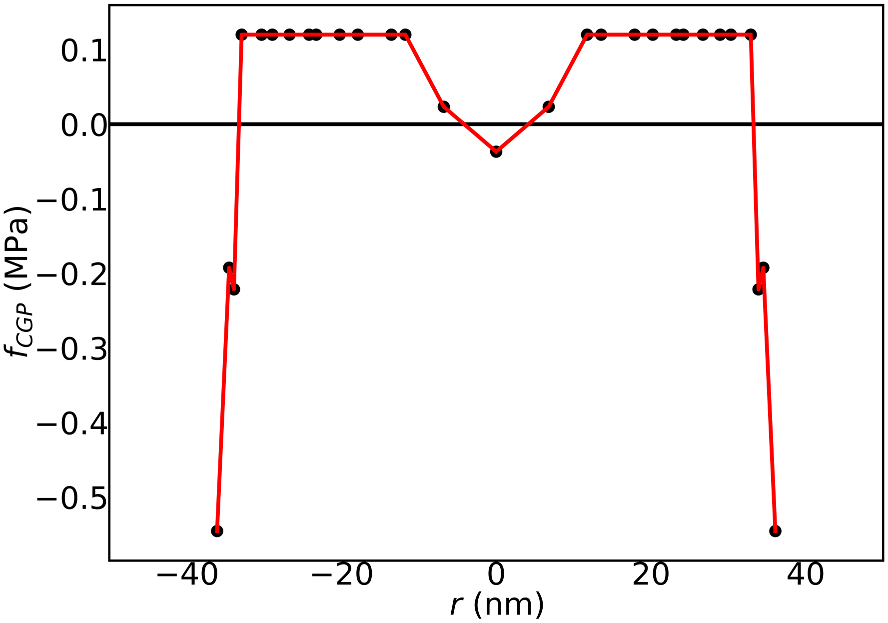

(b)

Figure 4.4: CGM force density vs. radius for $\Pi = 0.02$ MPa. b) CGM force density profile vs. radius for $\Pi = 0.12$ MPa.

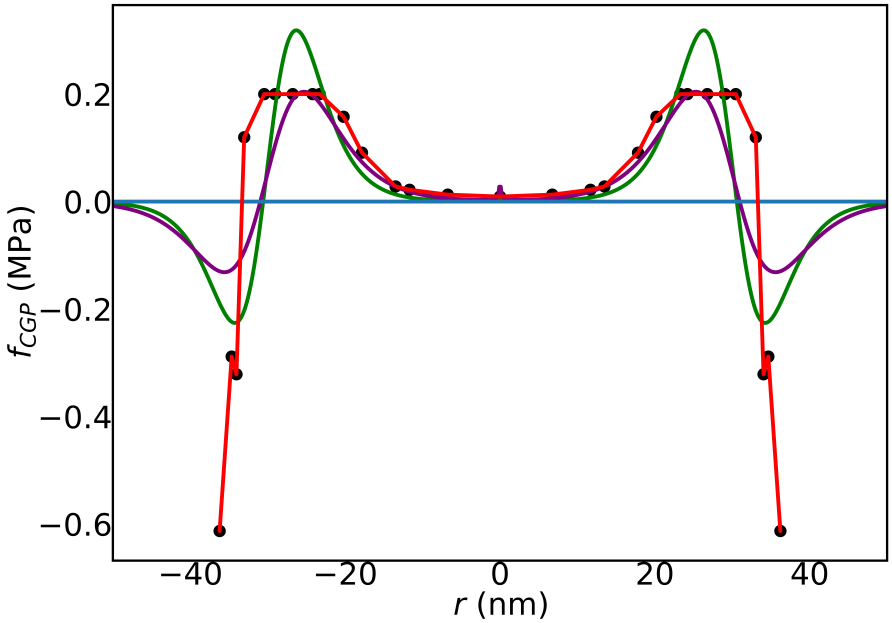

(a)

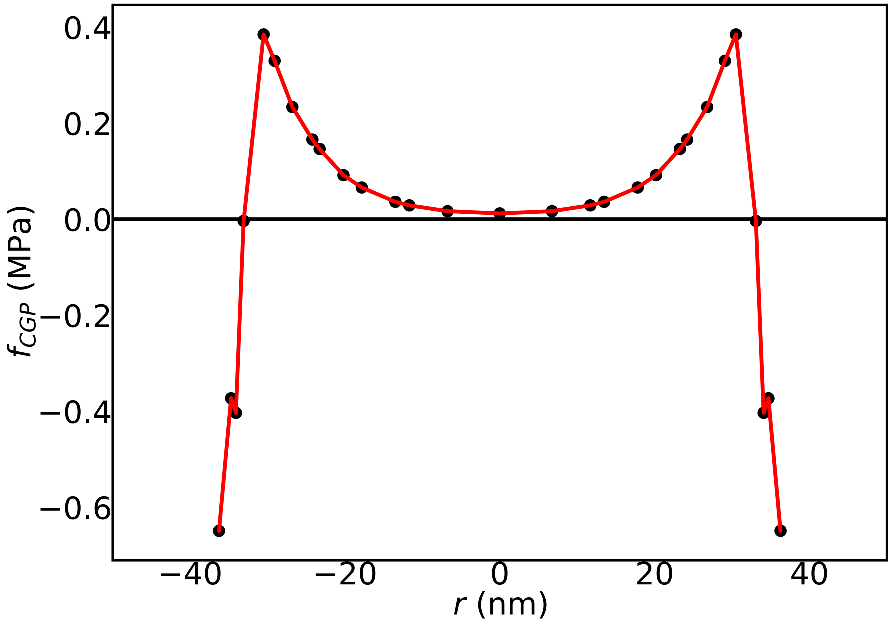

(b)

Figure 4.5: a) Continuous CGM force density profiles (purple, $\gamma = 0.13$; green,$\gamma = 0.167$) and discrete profile (red) vs. radius at 0.2 MPa. b) Discrete CGM force density profile vs. radius at 0.4 MPa.

Figure 4.6: Maximum turgor pressure CGMs can overcome vs. area. The blue curve is the maximum turgor pressure Π_{max} from the simulations, the orange curve is the best fit of the form a/A, and the green curve is the unfitted prediction (Equation 4.2).

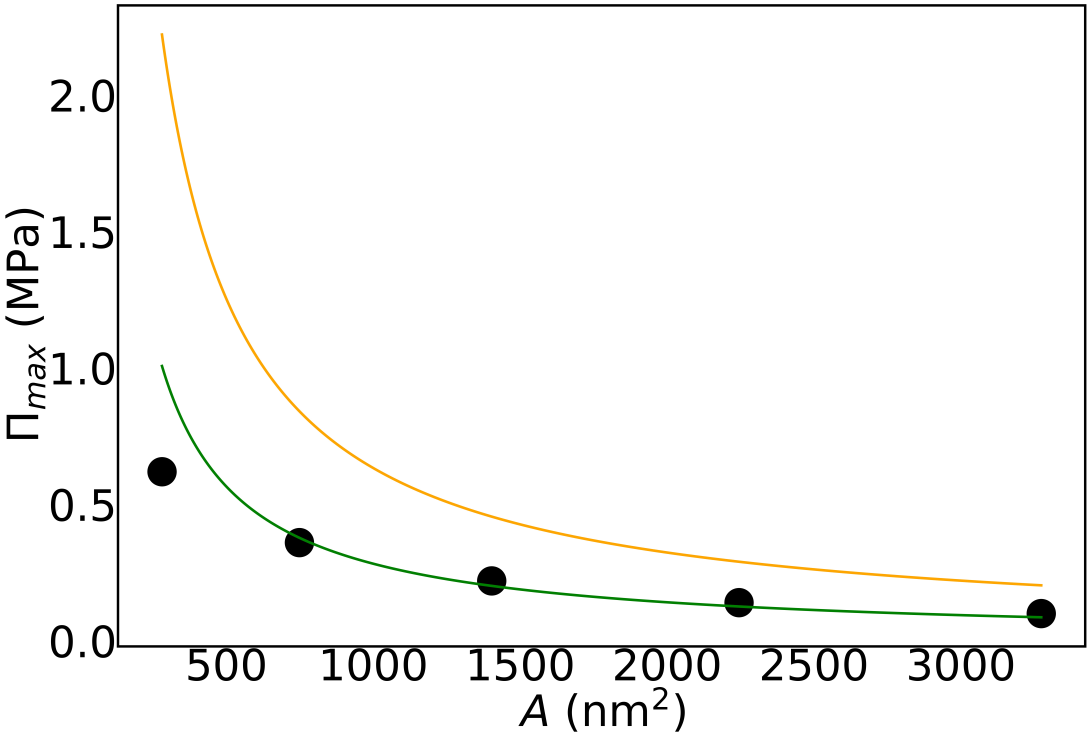

Figure 4.7: Maximum turgor pressure CGMs can overcome vs. κ. The black dots are the actual maximum turgor pressure Π_{max}, the orange curve is the best fit of the form $b\kappa$, and the green curve is the unfitted prediction (Equation 4.2).

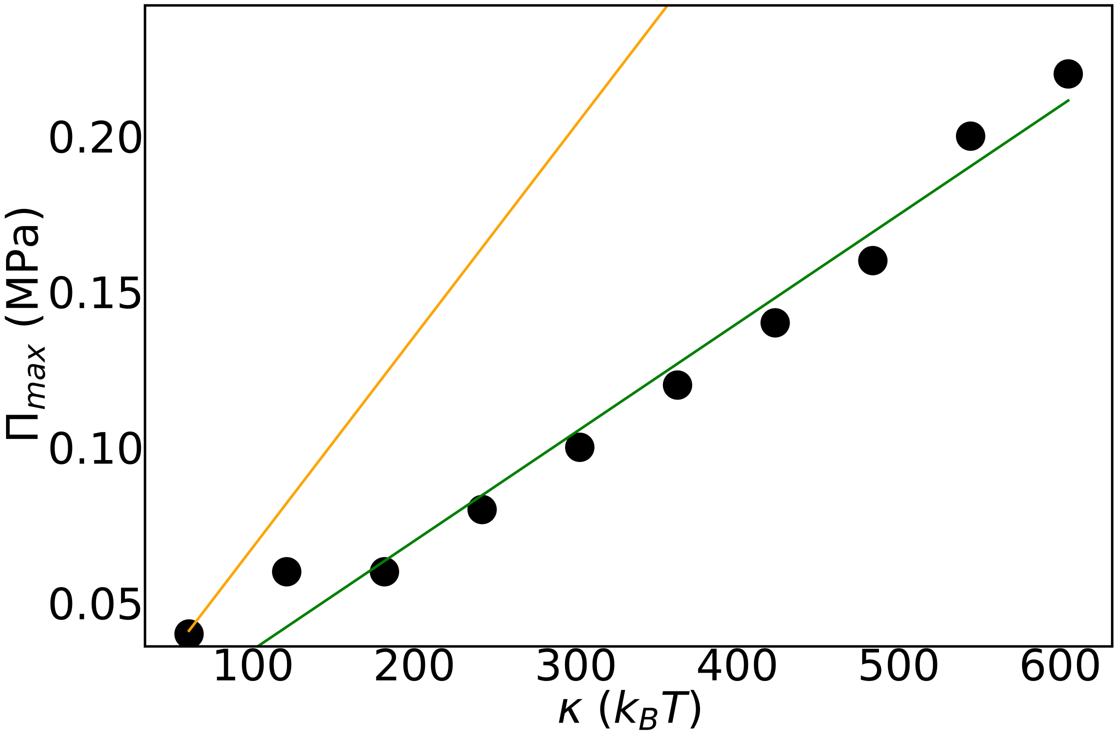

The area dependence of the CGM center force for the default parameters exhibits a transition between $A = 1400$ nm^2 and 2200 nm^2 (Figure 4.8a). This corresponds to the area becoming sufficiently large that the bending forces are not strong enough to overcome the turgor pressure and detach the CGM patch center from the cell wall; at smaller areas, the center is not in contact with the wall ($z > 0$), and the force density at the center is approximately equal to the turgor pressure. The total pulling force increases sublinearly with area.

Figure 4.8b shows the dependence of the center and maximum displacement on A. For physically realistic areas ($A > 1400$ nm^2) and the corresponding number of molecules ($N > 55$), the center of the patch does not detach from the cell wall for physical values of the bending rigidity and turgor pressure. Indeed, save for near small areas, the maximum and center height of the CGM patch decrease with increasing area, implying that the overall profile is flattening. This suggests that smaller CGM patches would successfully detach the membrane under pressures that might prevent larger patches from lifting off.

Figure 4.9 shows the dependence of CGM forces and displacements on preferred curvature. The force on the center of the CGM patch starts small but increases slowly with preferred curvature, up to a point. Around 0.04/nm curvature (for the other parameters default), the patch undergoes a transition, with the center detaching from the membrane (Figure 4.9a), which causes the load at the center of the CGM patch to approach its turgor-pressure-only value of 0.2 MPa, with the center force correspondingly approaching $-PA/N$. This suggests that the presence of CGMs alone might be sufficient to lift the center of an endocytic region off the cell wall, contrary to what might be expected from the presence of moments only at the edges in continuum theory. However, this occurs at a curvature of 0.043 per nm, significantly greater than our default value, which corresponds to the curvature of a clathrin-coated vesicle (0.02 nm). In addition, at a sufficiently high

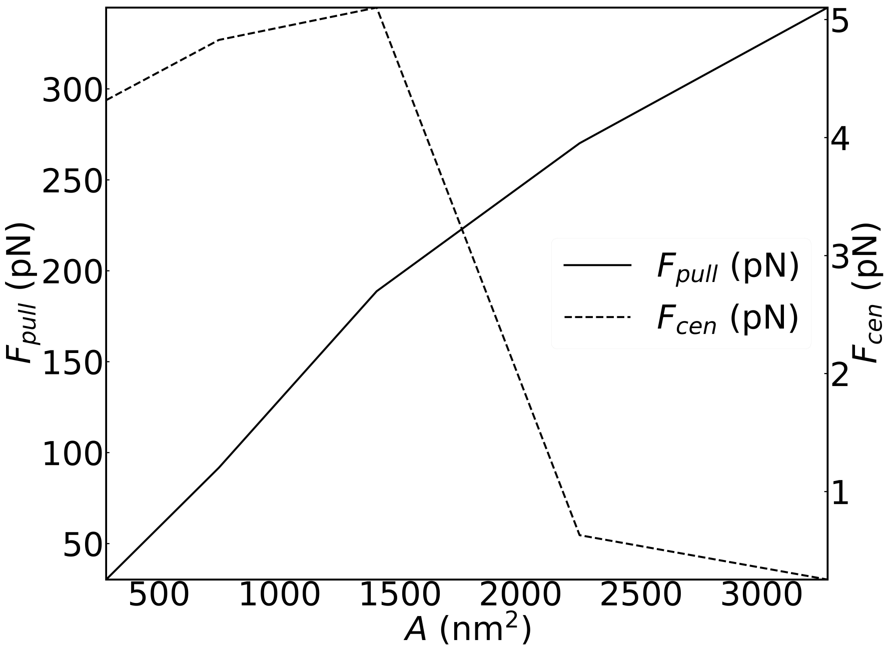

(a)

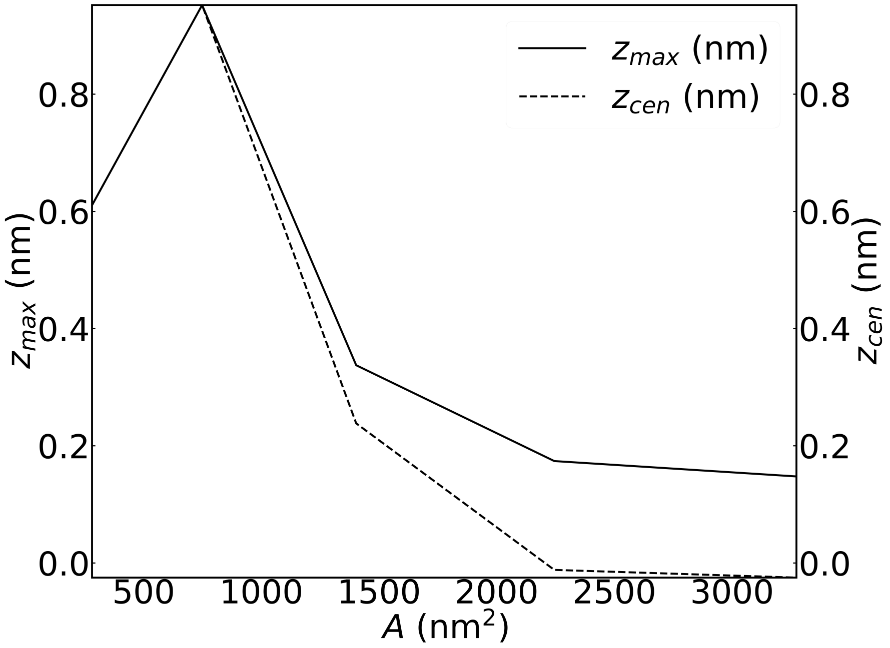

(b)

Figure 4.8: a) CGM force at CGM patch center (dashed) and total pulling force (solid) for varying area, with spacing constant. b) Center height (dashed) and maximum height (solid) for varying area, with spacing constant.

Figure 4.9: a) CGM force on center (dashed) and total pulling force (solid) vs. curvature. b) Height at center of patch (dashed) and maximum height (solid) vs. curvature

(a)

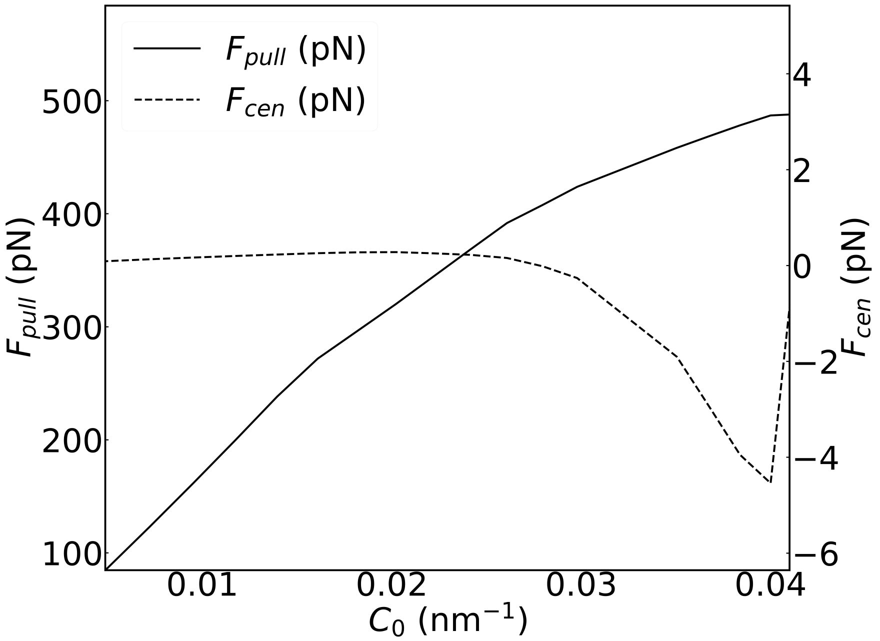

(b)

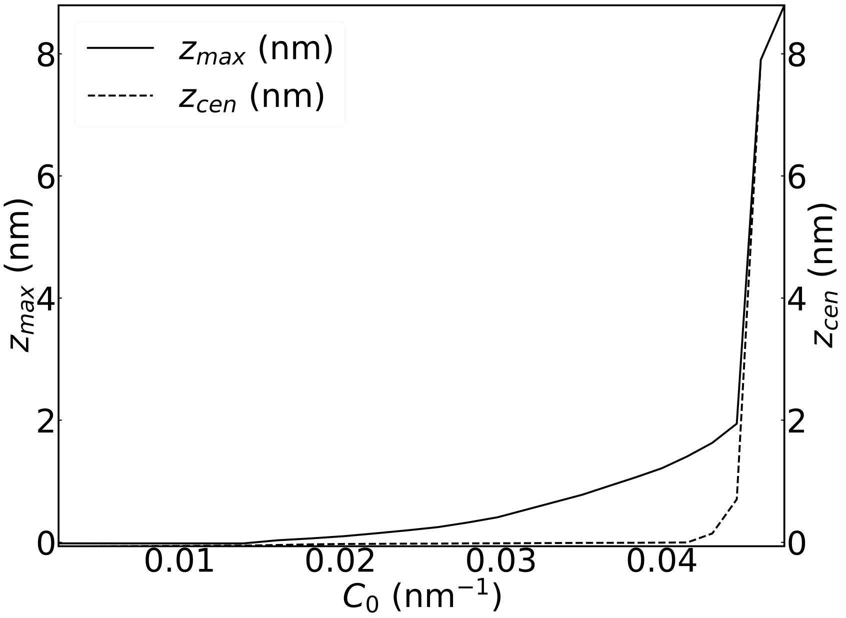

(unphysical) value of the intrinsic curvature, the molecules will be almost antiparallel, and the displacement will approach a maximum value. The total pulling force again increases sublinearly with curvature. A transition is also seen in the displacements (frame b)

As the bending rigidity κ increases, the CGM force on the center undergoes a rapid transition. At a certain critical value of κ, approximately 600 k_BT, the CGM-membrane patch lifts off the cell wall altogether (Figures 4.10b, 4.10a), indicated by the center force approaching a constant value of, corresponding to the force density per area approaching 0.2 MPa, equal to the magnitude of the turgor pressure (Figure 4.10a). The total pulling force also approaches a constant value of around 500 pN for high κ, indicating a maximum pulling force that can be generated at a given pressure regardless of stiffness, as well as suggesting that approximately 76% of the CGM molecules, or 92, are not in contact with the cell wall and thus generating the pulling forces. It is worth noting that the functional form of z_{cen} as a function of increasing κ (Figure 4.10b) does not have the same shape as its behavior with respect to the curvature (Figure 4.9b). This shows that the combination κC_0 used by Tweten et al. is not an accurate predictor of curvature-generating strength [135]. Further, the bending rigidity necessary to cause the membrane to lift off of the cell wall is much higher, relative to the corresponding biological values, than the intrinsic curvature necessary to do so: the critical value of κ is about 1950 k_BT (more than six times greater than the value of $300k_BT$ corresponding to the bending rigidity of a clathrin-coated vesicle, for instance), while the critical value of C_0 is about 0.043 per nm, which is only twice the intrinsic curvature of clathrin.

The center height also shows a rapid transition as a function of turgor pressure (Figure 4.11b). It changes from its maximum value of 10.5 nm (lifted off the cell wall) to being essentially flat against the membrane over a range of 0.12 MPa. For all values of the turgor pressure within a physically plausible range, the membrane-CGM complex is essentially

Figure 4.10: a) Force at center of patch (dashed) and total pulling force (solid) vs. κ. b) Center height (dashed) and maximum height (solid) vs. κ.

(a)

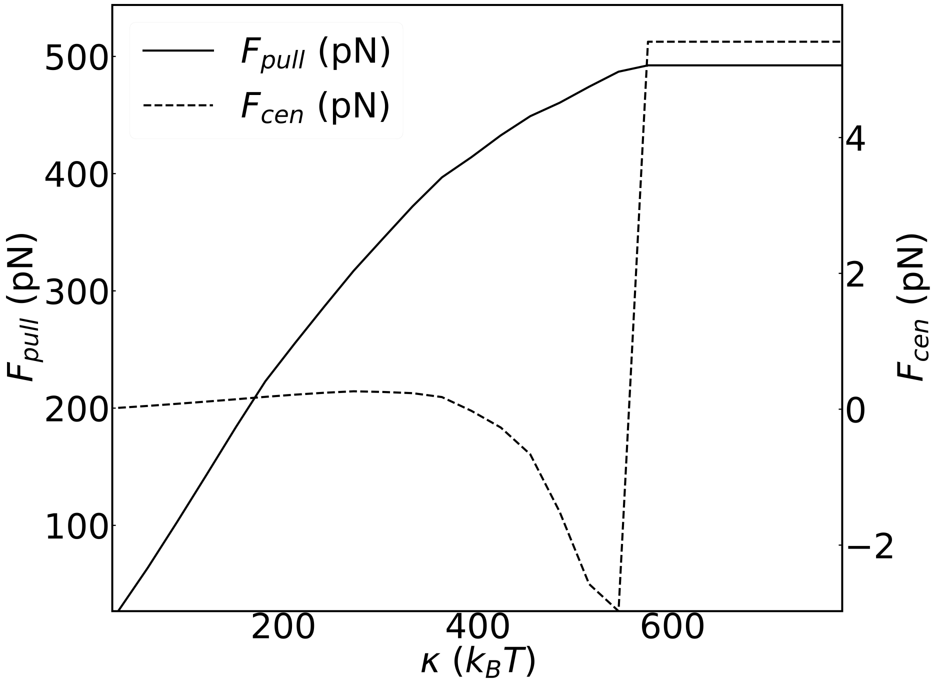

(b)

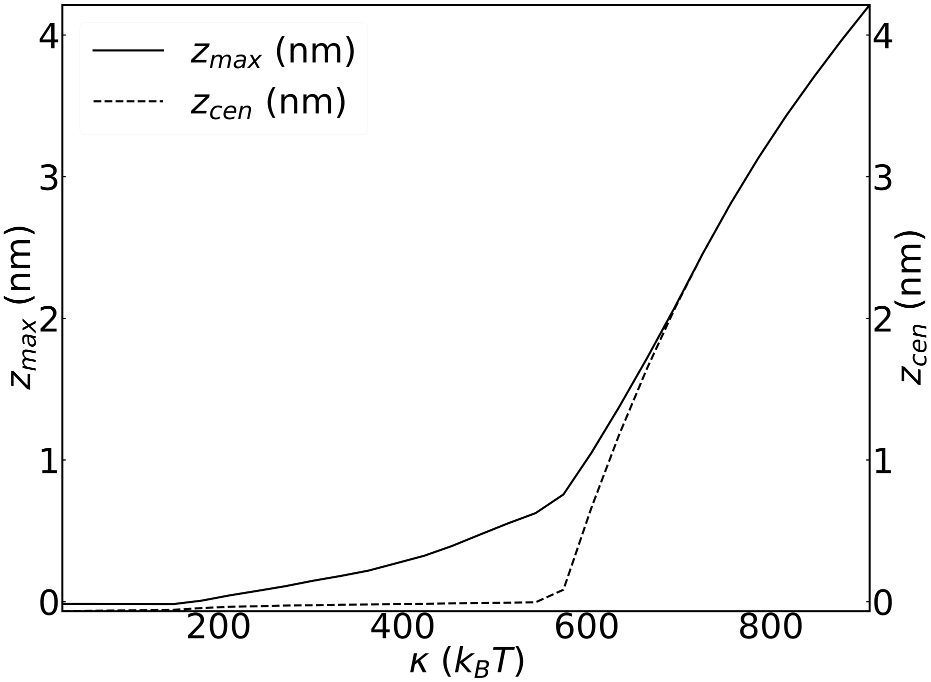

Figure 4.11: a) CGM force at center of patch (dashed) and total pulling force (solid) vs. turgor pressure. This includes the contribution from the turgor pressure itself. b) Center height (dashed) and maximum height (solid) vs. turgor pressure.

(a)

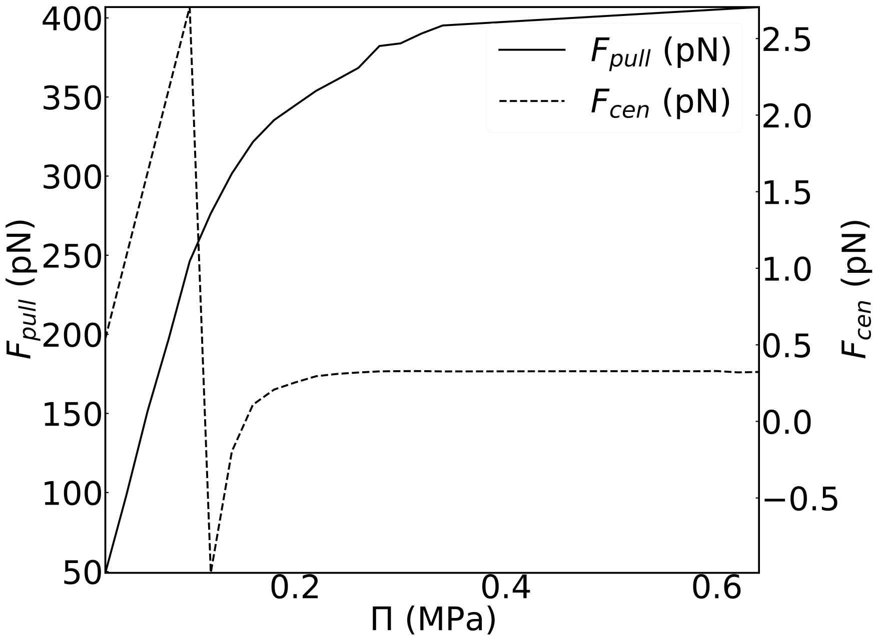

(b)

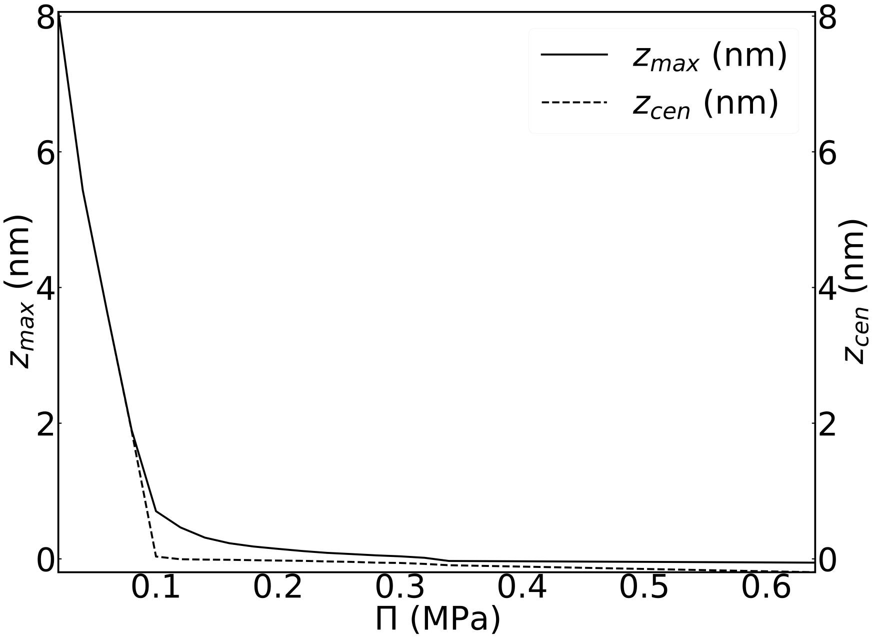

flat, again exhibiting the insufficiency of CGMs with comparable bending rigidity to that of clathrin to overcome turgor pressure on their own. On the other hand, the CGM force on the center of the patch (Figure 4.11a) increases up to the transition point of 0.12 MPa. It then exhibits a transition to negative values as the the pressure pushes the center of the CGMs into the cell wall, but then slowly increases as the complex is pressed further into the cell wall, since the magnitude of the wall force increases quadratically. This has little effect on the behavior of the total pulling force, however, which increases uniformly with pressure, since it is mostly unaffected by fluctuations in the sign of the height of individual molecules.

In order to see whether the combination of an attractive interaction between CGMs and the other mechanical interactions can lead to a preferred CGM patch size, we calculated the total CGM energy as a function of size for several values of k_a, the strength of the attractive interaction (see equation 4.7). The magnitude of the k_a term has no effect on the equilibrium configuration of the CGM-membrane complex for a given N. However, it does influence the number dependence of the energy, and thus the equilibrium number of molecules in the system. For small values of k_a, the energy increases without bound, indicating that the system will not grow at all if starting from a system of minimal size (Figure 4.12a).

Intermediate values, however, produce a minimum at physically realistic numbers of molecules (Figure 4.12b). As k_a increases, the optimal number of molecules grows. For $k_a/\mathrm{nm}^2 = 0.8k_b$, the minimum is at 31 molecules, occupying an area of about 280 nm^2. Around $k_a/\mathrm{nm}^2 = k_b$, the optimal number increases rapidly, with an equilibrium at around 163 molecules or 4490 nm^2. An equilibrium corresponding to the default number and area occurs slightly below $k_a/\mathrm{nm}^2 = k_b$. However, the optimal number can exceed 121; the data for this case is not present in the figure.

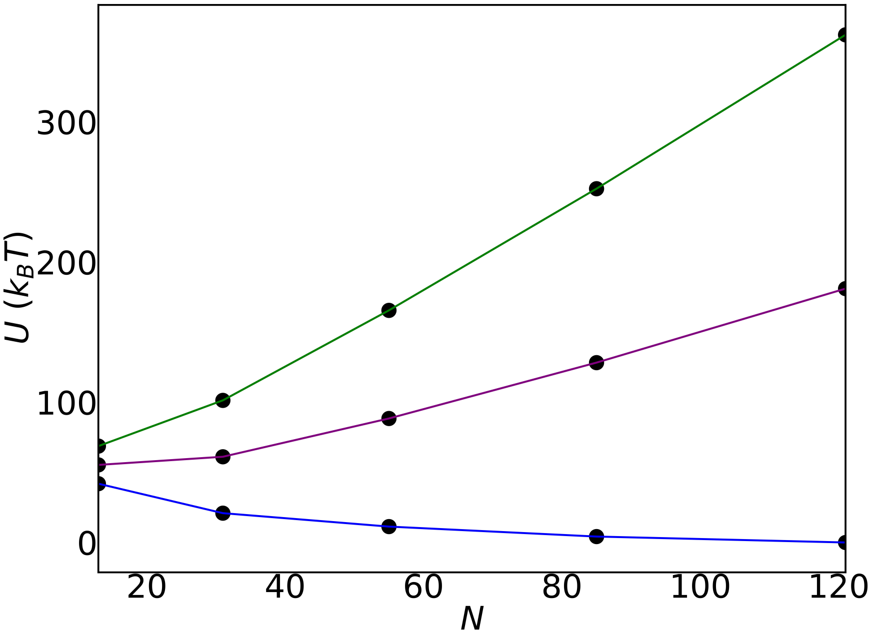

(a)

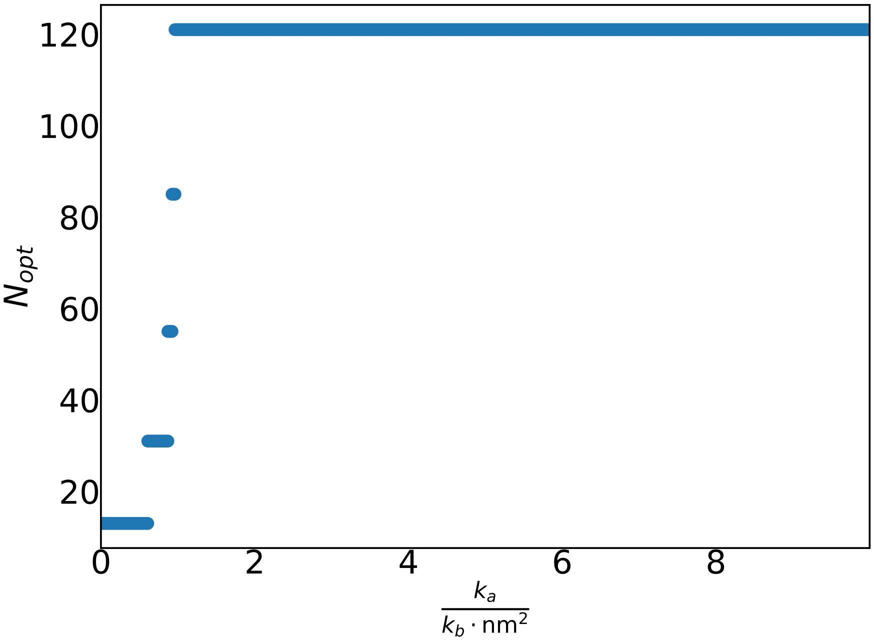

(b)

Figure 4.12: a) Total equilibrium energy vs. number of CGM molecules for $k_a/\mathrm{nm}^2 = 0$, $0.5k_b$, $0.8k_b$, k_b (red, purple, green, and blue). Plot starts at 13 molecules. b) Optimal CGM number vs. $\frac{k_a}{k_b \cdot \mathrm{nm}^2}$.

4.4 Discussion

4.4.1 Conclusions

The results of the simulations and analytic theory suggest that CGMs may play a major role in producing membrane curvature, and by extension in driving processes such as endocytosis. For CGMs with a bending rigidity corresponding to that of clathrin, the stiffness is about 16% of that needed to lift the membrane-CGM complex 8 nm, or about 80% of its maximum zero-turgor height, off the cell wall against a turgor pressure of 200 kPa. If we consider the effects of actin, we see that a CGM with properties comparable to clathrin is sufficient to lift the membrane about 2 nm off the cell wall, or 20% of its maximum height, in the presence of an effective turgor pressure corresponding to the presence of actin. However, to successfully lift the lipid bilayer off the cell wall by itself, a CGM would have to have an intrinsic curvature twice that of clathrin, or have about six times the bending rigidity of the clathrin-membrane complex.

It is also clear that CGMs do not merely produce moments at the edges of a CGM patch, as continuous models might suggest (Section 4.9), but also produce a substantial force at the center of the endocytic region, thus providing a portion of the force necessary to initiate endocytosis. We found that a reasonably accurate continuous approximation to the CGM force is given by the force corresponding to a tanh distribution of CGMs.

Further, the simulations suggest that the transition from on-wall to off-wall behavior is quite rapid. The membrane transitions from being pressed into the cell wall ($z < 0$) to 1 nm above the cell wall over a pressure range of about 0.1 MPa, or a curvature range of about 0.01 per nm. It is thus likely that once a certain critical load is reached (whether from CGM accumulation, actin nucleation, or even local reduction of the turgor pressure), endocytosis proceeds rapidly. This is also borne out by the discontinuous transition of the forces as a function of various parameters. Part of this comes from the nature of the cell wall interaction as a contact force, a feature which is lost in treatments of the wall-turgor interaction as quadratic.

4.4.2 Limitations

The examined models in this paper, both discrete and continuous, are equilibrium models that ignore time-dependent fluctuation effects. In particular, the size of the average fluctuation of a membrane in a linear pressure potential near a hard wall, as in our model, is given by [89]:

$$\sigma = \left[\frac{(k_B T)^2}{64 c_\perp \kappa}\right]^{1/3} P^{-1/3} \tag{4.10}$$

Here $c_\perp = 1.81$. For the typical case of a clathrin-coated membrane in a yeast cell, $\kappa = 300 k_B T$ and $P = 0.2$ MPa, producing an average fluctuation size of 0.08 nm. Given this small magnitude relative to the displacement of the CGMs, it is probably legitimate to neglect fluctuations.

Our assumption of rod-shaped rod-shaped molecules with differing preferred distances between the top and bottom is a minimal model for generating intrinsic curvature, but it does not accurately correspond to any particular curvature-inducing molecule. Clathrin, for instance, actually forms from triskelial molecules, and also has specific interactions between portions of the triskelion legs. The linear shape is perhaps most similar to intrinsically-curved lipids, which may not have much influence on membrane curvature during endocytosis. However, this limitation is also a strength, insofar as the results may be applicable with some degree of accuracy to all CGPs.

The turgor pressure is treated statically, not dynamically, and assumed to be uniform. The uniformity of the turgor pressure is not certain: as we have suggested in our previous paper [114], it is possible for local channel accumulation to induce a spatially varying turgor pressure.

Most of the model parameters are derived from measured quantities such as the bending rigidity of clathrin or the yeast turgor pressure. However, the extent of the k_c anti-slipping interaction in particular is uncertain. It roughly corresponds to the shear strength, but to our knowledge there are not any experiments directly measuring this for clathrin-coated vesicles.

4.4.3 Relation to experiment

Measuring the variation of the shape of CGP complexes on the scale predicted by this model is difficult, particularly in the case of endocytosis. Live-cell imaging typically has a resolution of no better than 60 nm, and the height variations predicted by this model range from approximately 4 nm (in the zero-turgor case) to a few tenths or hundredths of a nanometer in the case of more realistic turgor pressure, on the order of 0.2 MPa. As such, it may be virtually impossible to directly confirm the structures predicted here via light microscopy. However, electron microscopy may be able to elucidate the coarsest features.

The force profiles generated by those shapes are also difficult to measure because of the small lateral size. However, the maximum center force generated by CGPs under high-turgor versus low-turgor conditions could potentially be measured. There are some force-sensing molecules suitable for measuring intracellular forces [107], such as fusion-protein based sensors. It could be possible to engineer sensors to measure forces at the CGM-membrane contacts.

The relationships between the various parameters and CGM complex detachment from the cell wall are easier to test. Previous research has examined the effect of varying turgor pressure on the depth of membrane invagination in fission yeast [12]. Some aspects of these results might be predicted quantitatively by our model, if the effects of actin forces can be subtracted off (potentially effectively equivalent to a reduced value of Π in our model). The effect of stiffness on membrane displacement could be measured by varying the composition of the cell wall. Finally, comparison of the magnitude of membrane displacement produced by different CGPs could provide confirmation or disconfirmation of the effects of intrinsic curvature on membrane displacement predicted by our model.

4.5 Author contributions

J.K.S.-Z. performed the calculations, prepared the figures, and co-wrote the paper. A.E.C co-wrote the paper.

4.6 Acknowledgements

This work was supported by the National Institutes of Health under Grant R01 GM107667 and the National Science Foundation under Grant Agreement CMMI:15-458571. We appreciate informative input from Phil Bayly.

4.7 Cell wall elastic theory

We derive the energy of interaction of the CGMs with the cell wall by considering two easily treatable cases. We have a collection of molecules indexed by i. The molecules are arranged a on a square lattice, and the cell wall has thickness t and is assumed to be infinite in extent. First, let us consider the case in which all the molecules have an equal displacement, i.e. $u_i = u$. Then, from the definition of the Young's modulus Y, the areal force density is $f = Yu/t$, and thus the force on each molecule is simply this scaled by the area per molecule, $F_i = YA_m u_i/t$.

Let us next consider the case where the displacement of the molecules alternates, i.e. $u_i = u_0 e^{i\mathbf{q}\cdot\mathbf{r}}$, where the exponential alternates between ± 1. In this case we assume a semiinfinite cell wall because the molecule spacing is much smaller than the thickness. Then the the Fourier transform of the force density is $f = Yku_k$, which gives

$$F_i = -\sqrt{2}\pi Y A_m u_i/a, \tag{4.11}$$

where a is the intermolecular spacing.

We fit these two results to a harmonic force of the form:

$$F_i = -k_0 u_i + k_1 \sum_{j\in\langle nn\rangle} (u_j - u_i) \tag{4.12}$$

This gives

$$k_0, k_1 = \frac{A_m Y}{t}, \frac{A_m Y}{6}\left(\frac{\pi}{\sqrt{2}a} - \frac{1}{t}\right) \tag{4.13}$$

This thus corresponds to an energy of

$$U_i = \frac{1}{2}(k_0 + 6k_1)u_i^2 - \frac{1}{2}k_1 \sum_{j\in\langle nn\rangle} u_i u_j \tag{4.14}$$

It is important to note that this form of the energy, used in our simulations, only strictly is valid in the interior of the CGM patch. At boundary points, where molecules have less than the full number of nearest neighbors, it is somewhat inaccurate, which could lead to overestimation of the effective wall force experienced by these molecules.

4.8 Helfrich membrane theory with wall potential

A lipid bilayer can be modeled as a thin membrane subject to bending forces (strength κ), and surface tension (strength σ). In yeast, this membrane also experiences force from high turgor pressure and a rigid cell wall. This is modeled by a quadratic potential per area $\frac{1}{2}\kappa_w z^2$, corresponding to the wall force, and a linear potential Πz corresponding to the turgor pressure. The wall force potential is only present for $z < 0$. The Helfrich membrane energy for the portion of the system below the cell wall is:

$$U = \int\limits_S dS[2\kappa(C - C_0)^2 + \sigma + \frac{1}{2}k_w z^2 + \Pi z] \tag{4.15}$$

For the portion above the cell wall, the quadratic term is not present. A similar equation has previously [147] been described and analyzed for a clathrin-coated membrane, but the above equation incorporates the effects of turgor pressure and wall forces, leading to a different equation of shape.

We use the Monge parametrization, i.e. $z = z(x, y)$, and the small-displacement approximation, i.e. $dS = 2\pi r[1 + \frac{1}{2}(\bigtriangledown_S z)^2]dr)$.

This leads to the equation of shape:

$$z'''' + \frac{2}{r}z''' - (\frac{1}{r^2} + \xi^2)z'' + (\frac{1}{r^3} - \frac{\xi^2}{r})z' + \frac{\kappa_w}{\kappa_b}[z - \frac{1}{2}(z')^2 + \frac{1}{2}z^2 z'' + \frac{1}{2}z^2 z']\Big[\frac{1}{2} - \frac{1}{2}H(z)\Big] + \Pi/\kappa = 0 \tag{4.16}$$

where $\xi^2 = 2C_0^2 + \frac{\sigma}{\kappa_b}$.

However, for computational convenience and improved convergence, we use the linearized version:

$$z'''' + \frac{2}{r}z''' - (\frac{1}{r^2} + \xi^2)z'' + (\frac{1}{r^3} - \frac{\xi^2}{r})z' + \frac{\kappa_w}{\kappa_b}z\Big[\frac{1}{2} - \frac{1}{2}H(z)\Big] + \Pi/\kappa = 0 \qquad (4.17)$$

which corresponds to:

$$\bigtriangledown^4 z - \xi \bigtriangledown^2 z + \frac{\kappa_w}{\kappa_b}z\Big[\frac{1}{2} - \frac{1}{2}H(z)\Big] + \Pi/\kappa = 0 \qquad (4.18)$$

Or:

$$\frac{1}{\zeta}\bigtriangledown^4 z - \frac{\xi^2}{\zeta}\bigtriangledown^2 z + z\Big[\frac{1}{2} - \frac{1}{2}H(z)\Big] + \Pi/\kappa = 0 \qquad (4.19)$$

where $\zeta = \frac{\kappa_w}{\kappa_b}$.

This is equivalent to

$$(1 - c_1\bigtriangledown^2)(1 - c_2\bigtriangledown^2)z + \Pi/\kappa = 0 \qquad (4.20)$$

For $c_1, c_2 = \frac{1}{2\zeta}(\xi^2 \pm \sqrt{\xi^4 - 4\zeta})$.

For $k = 5904$, corresponding to low turgor pressure, this simplification changes the center height by less than 0.3%, and for high turgor pressure ($k = 0.66$) it changes the center height by about 0.009%.

Equation 4.19 has the solution

$$z(r) = a_1 I_0(\xi r) + a_2 K_0(\xi r) + a_3 \ln r + a_4 + \frac{\Pi}{4\kappa\xi^2} r^2 \tag{4.21}$$

above the cell wall, and

$$z(r) = b_1 I_0(c_1 r) + b_2 I_0(c_2 r) + b_3 K_0(c_1 r) + b_4 K_0(c_2 r) - \Pi/\kappa \tag{4.22}$$

below the cell wall. Here I_0, K_0 are the modified Bessel functions of order zero.

The four (possibly complex) coefficients are determined by the boundary conditions, the form of which is determined by the type of system being considered. They can either be derived from the Helfrich energy density, the physical constraints imposed upon the system, or a combination thereof. In particular, for a fixed radius of integration R, consider the energy:

$$U = \int_0^R dr L(r, z, z', z'') \tag{4.23}$$

The shape equation is given by

$$\delta U = \lim_{\epsilon \to 0} \frac{d}{d\epsilon} U(z + \epsilon \delta z) = 0 \tag{4.24}$$

We can thus write:

$$\delta U = \int_0^R dr \Big[\frac{\partial L}{\partial z} \delta z + \frac{\partial L}{\partial z'} \delta z' + \frac{\partial L}{\partial z''} \delta z'' \Big] \tag{4.25}$$

Applying integration by parts, we are left with

$$\delta U = \left[\left(\frac{\partial L}{\partial z'} - \frac{d}{dr}\frac{\partial L}{\partial z''}\right)\delta z(r)\right]_{r=0}^{r=R} + \left[\frac{\partial L}{\partial z''}\delta z'(r)\right]_{r=0}^{r=R} + \int_{0}^{R} dr \left[\frac{\partial L}{\partial z} - \frac{d}{dr}\frac{\partial L}{\partial z'} + \frac{d^2}{dr^2}\frac{\partial L}{\partial z''}\right]\delta z \quad (4.26)$$

The last term is simply the familiar Euler-Lagrange equation, which in the Monge parametrization corresponds to Equation 4.16. The other four terms provide the natural boundary conditions: either a term's coefficient is zero, or the corresponding variable in the variation is constant: e.g. either $z'(R)$ is constant or the bending moment is zero. The first two terms correspond to line or point forces, and the last two correspond to bending moments, as expanded upon in the next section.

For the function to be symmetric and not have a cusp, it is necessary that $z'(0) = 0$. For all the other cases, we choose the natural boundary conditions corresponding to the coefficients of the boundary variations being zero.

4.9 Forces and Bending Moments in the Continuum Model with CGMs

In the case of a continuum model of a CGM patch of stiffness κ_1 and intrinsic curvature on a membrane of stiffness κ_2 and zero intrinsic curvature C_0 , neglecting Gaussian curvature and line tension, which do not change the final result, the energy is [147]:

$$U = \int_{0}^{R} L_1 dr + \int_{R}^{\infty} L_2 dr \quad (4.27)$$

where

$$L_1 = \pi\kappa_1 r\left[\left(\frac{1}{r}z' + z''\right)^2 - 4C_0\left(\frac{1}{r}z' + z''\right) + \xi_1^2(z')^2 + 2\xi_1^2\right] \tag{4.28}$$

and

$$L_2 = \pi\kappa_2 r\left[\left(\frac{1}{r}z' + z''\right)^2 + \xi_2^2(z')^2 + 2\xi_2^2\right] \tag{4.29}$$

The system is subject to the following forces and moments in the z-direction: A force density per area, which is simply the variational derivative of the energy with respect to displacement that gives the Euler-Lagrange equations, $\frac{\delta U}{\delta z}$, a point force at the center, $\frac{\delta U}{\delta z}\Big|_{r=0}$, a line force at the interface between the two regions $\frac{\delta U}{\delta z}\Big|_{r=R}$, and a bending moment at this same interface, $\frac{\delta U}{\delta z'}\Big|_{r=R}$.

Now,

$$\begin{gathered} \tfrac{\partial L_1}{\partial z} = 0 \\ \tfrac{\partial L_1}{\partial z'} = 2\pi\kappa_1\left(\tfrac{1}{r}z' + z''\right) + 2\pi\kappa_1\xi_1^2 r z' - 4\pi\kappa_1 C_0 \\ \tfrac{\partial L_1}{\partial z''} = 2\pi\kappa_2 r\left(\tfrac{1}{r}z' + z''\right) - 4\pi\kappa_1 C_0 r \end{gathered} \tag{4.30}$$

The expressions for the second Lagrangian are easily obtained by substituting $C_0 = 0$. The first variational derivative is then simply

$$\frac{\partial L_1}{\partial z} - \frac{\partial}{\partial r}\frac{\partial L_1}{\partial z'} + \frac{\partial^2}{\partial r^2}\frac{\partial L_1}{\partial z''} \tag{4.31}$$

The radial derivative eliminates the curvature terms from equation 4.30, and then all the remaining terms are zero since they contain powers of $z^{(n)}$, which are zero for an identically flat membrane.

The term corresponding to $\delta z(R)$ is $\frac{\partial L_1}{\partial z'} - \frac{\partial}{\partial r}\frac{\partial L_1}{\partial z''}$, or the equivalent for L_2. In this case the term $-4\pi\kappa_1 C_0$ from $\frac{\partial L_1}{\partial z'}$ is cancelled out by the corresponding term in $\frac{\partial}{\partial r}\frac{\partial L_1}{\partial z''}$, which also implies that the term in the variation corresponding to $\delta z(0)$ is zero. These terms correspond to a line force density and a point force per length, respectively. However, $\frac{\partial L_1}{\partial z''}$ is $-4\pi\kappa_1 R C_0$ at $r = R$. The bending moment is therefore $\frac{\partial L_1}{\partial z''} - \frac{\partial L_2}{\partial z''} = -4\pi\kappa_1 R C_0$. The bending moment density per length around the boundary will then be $-4\kappa_1 C_0$.

Thus, for the case of a continuum Helfrich-theory model of a flat membrane, the CGMs generate no forces, and only generate bending moments concentrated at the edges.

Chapter 5

Summary and Future Directions

In this thesis, we considered theoretical models of various aspects of endocytosis in cells with high turgor pressure. First, in Chapter 2, we considered the barrier to endocytosis posed by the high osmotic pressure in yeast cells, roughly proportional to the difference in osmolyte concentration between the interior and exterior, which a rough estimate suggested could not be overcome by actin and clathrin alone. To investigate the possibility that cells might reduce this turgor pressure barrier in the vicinity of the endocytic zone, we developed a semi-analytic model of the diffusion of the osmolyte glycerol consisting of a single spherical cell with a spatially varying permeability, which we solved using a Fourier-Legendre series method. This allowed us to characterize the radial and angular distribution of glycerol in the system inside and outside the cell. We found that physically reasonable numbers of patches could produce a substantial turgor pressure reduction, around 50%. Finally, we characterized the dependence of the steady-state concentration profile on various parameters of interest, such as the patch size and the patch permeability, providing and testing simple analytic estimates of the dependence of quantities such as the average concentration. We also compared this description to a fully analytic solution in the vicinity of the patch under certain simplifying approximations.

We then extended this model. In Chapter 3 we examined glycerol diffusion models with an arbitrary angularly-dependent permeability, corresponding to the presence of multiple endocytic patches. We also were able to incorporate the time evolution of the glycerol concentration. We examined these aspects primarily through finite-element modeling, although we also extended our semi-analytic theory to a more general angular dependence and incorporated time dependence. In the case of a single permeable patch, we found that the equilibration time was approximately 10 seconds, less than the time scale of endocytosis.We found that we were able to describe the equilibration of the system in terms of a small number of eigenvalues, one interior and one exterior. We also found that for small numbers of permeable patches, the total number and distribution of patches has little effect on the ratio of the concentration near a patch to the concentration far from a patch.

Finally, in Chapter 4 we modeled a system of idealized rod-shaped curvature-generating molecules under high turgor pressure in the presence of a stiff cell wall. We calculated the steady-state configuration of this system, which incorporated simple intermolecular interactions that generated curvature and resisted shear forces, turgor pressure, lipid membrane, and wall forces. Further, we developed an analytic model of the system based on Helfrich membrane theory. We found that, contrary to the basic estimate at the start of Chapter 3, CGMs with a stiffness comparable to that of clathrin cannot fully overcome the turgor pressure, although they come closer to overcoming a effective reduced turgor pressure incorporating the presence of actin. We modeled the differences between CGM-membrane profiles and force distributions under high and low turgor pressure, corresponding for instance to yeast and mammalian cells, noting that the turgor pressure significantly reduced the height of the CGMs profiles relative to the turgor-free case. We compared the force distributions to previous analytic estimates of CGM forces. We were also able to look at the parameter dependence of the positions and forces in this system, allowing the results to be generalized to CGMs with curvature or stiffness different from those of clathrin. Finally, we demonstrated the presence of a stable molecule number with a simple number-dependent attractive interaction.

There are several potential research directions we could follow to extend this work. First, although the analytic theory of a spherical cell with multiple endocytic regions is straightforward, the estimation of the concentration for physical patch sizes presents difficulties when using the most obvious methods of calculation. However, it might be possible to simplify the formula to reduce computational difficulty and calculate the concentration semi-analytically, which would allow for comparison with FE element formulations of the problem. As well, certain simple approximate analytic formulas could be derived from the formulas given in Chapter 3 for multiple patches or time-dependent systems. We could also potentially incorporate the time dependence into this formulation, although practically this provides another layer of computational difficulty.

The FEM formulation of the glycerol diffusion problem readily lends itself to examining the forces and stresses that occur during the equilibration process. Future models could be extended to incorporate these variables. In addition, some previous papers have suggested that local changes in the turgor pressure may provide a mechanism of cellular locomotion. By incorporating hydrodynamics into the FeBio FEM model, we could potentially look at how local permeability increases could cause a cell to migrate.

With regard to our model of curvature-generating molecules, we have modeled the CGMs as rod-shaped molecules with very general interactions. Although this may improve the generality of the model, and may be accurate for certain molecules such as preferentially curved lipids, real CGMs, in particular clathrin, have more complicated interactions. We could consider molecules with a different geometry, such as the triskelial geometry of clathrin, and different interactions between the various zones. We could also do a full molecular dynamics simulation of the system, which would allow us to consider both its time evolution, and to treat the effect of thermal fluctuations on the equilibrium profile of the CGM region. In addition, we could extend the analytic model to incorporate the portion of the membrane beyond the CGM-coated region.

References

[1] Soheil Aghamohammadzadeh and Kathryn R Ayscough. “Differential requirements for actin during yeast and mammalian endocytosis.” In: *Nature cell biology* 11.8 (2009), pp. 1039–1042.

[2] Neeraj J Agrawal, Jonathan Nukpezah, and Ravi Radhakrishnan. “Minimal mesoscale model for protein-mediated vesiculation in clathrin-dependent endocytosis.” In: *PLoS computational biology* 6.9 (2010), e1000926.

[3] B Aguilar-Uscanga and JM Francois. “A study of the yeast cell wall composition and structure in response to growth conditions and mode of cultivation.” In: *Letters in applied microbiology* 37.3 (2003), pp. 268–274.

[4] Paulo FF Almeida, Winchil LC Vaz, and TE Thompson. “Lipid diffusion, free area, and molecular dynamics simulations.” In: *Biophysical journal* 88.6 (2005), pp. 4434–4438.

[5] John L Anderson and Dermot M Malone. “Mechanism of osmotic flow in porous membranes.” In: *Biophysical journal* 14.12 (1974), pp. 957–982.

[6] Lars André, Anna Hemming, and Lennart Adler. “Osmoregulation in Saccharomyces cerevisiae studies on the osmotic induction of glycerol production and glycerol 3-phosphate dehydrogenase (NAD+).” In: *FEBS letters* 286.1-2 (1991), pp. 13–17.

[7] Ori Avinoam, Martin Schorb, Carsten J Beese, John AG Briggs, and Marko Kaksonen. “Endocytic sites mature by continuous bending and remodeling of the clathrin coat.” In: *Science* 348.6241 (2015), pp. 1369–1372.

[8] Katja Backhaus, Clemens J Heilmann, Alice G Sorgo, Günter Purschke, Chris G de Koster, Frans M Klis, and Jürgen J Heinisch. “A systematic study of the cell wall composition of Kluyveromyces lactis.” In: *Yeast* 27.8 (2010), pp. 647–660.

[9] David Ball. *Physical Chemistry.* Thomson Brooks-Cole, 2011.

[10] F Baluška, J Šamaj, A Hlavacka, J Kendrick-Jones, and D Volkmann. “Actin-dependent fluid-phase endocytosis in inner cortex cells of maize root apices.” In: *Journal of Experimental Botany* 55.396 (2004), pp. 463–473.

[11] František Baluška et al. “F-actin-dependent endocytosis of cell wall pectins in meristematic root cells. Insights from brefeldin A-induced compartments.” In: *Plant Physiology* 130.1 (2002), pp. 422–431.

[12] Roshni Basu, Emilia Laura Munteanu, and Fred Chang. “Role of turgor pressure in endocytosis in fission yeast.” In: *Molecular biology of the cell* 25.5 (2014), pp. 679–687.

[13] Léna Beauzamy, Julien Derr, and Arezki Boudaoud. “Quantifying hydrostatic pressure in plant cells by using indentation with an atomic force microscope.” In: *Biophysical journal* 108.10 (2015), pp. 2448–2456.

[14] Léna Beauzamy, Naomi Nakayama, and Arezki Boudaoud. “Flowers under pressure: ins and outs of turgor regulation in development.” In: *Annals of botany* 114.7 (2014), pp. 1517–1533.

[15] Eric Beitz, Slavica Pavlovic-Djuranovic, Masato Yasui, Peter Agre, and Joachim E Schultz. “Molecular dissection of water and glycerol permeability of the aquaglyceroporin from Plasmodium falciparum by mutational analysis.” In: *Proceedings of the National Academy of Sciences of the United States of America* 101.5 (2004), pp. 1153–1158.

[16] Howard C Berg. *Random walks in biology.* Princeton University Press, 1993.

[17] Julien Berro, Vladimir Sirotkin, and Thomas D Pollard. “Mathematical modeling of endocytic actin patch kinetics in fission yeast: disassembly requires release of actin filament fragments.” In: *Mol. Biol. Cell* 21.16 (2010), pp. 2905–2915.

[18] Ryan Bradley and Ravi Radhakrishnan. “Curvature-Undulation Coupling as a Basis for Curvature Sensing and Generation in Bilayer Membranes.” In: *Biophysical Journal* 112.3 (2017), 220a–221a.

[19] John F Brady. “Brownian motion, hydrodynamics, and the osmotic pressure.” In: *The Journal of chemical physics* 98.4 (1993), pp. 3335–3341.

[20] Christopher Buser and David G Drubin. “Ultrastructural imaging of endocytic sites in Saccharomyces cerevisiae by transmission electron microscopy and immunolabeling.” In: *Microscopy and Microanalysis* 19.2 (2013), pp. 381–392.

[21] Anna Bzducha-Wróbel, Stanisław Błażejak, Magdalena Molenda, and Lidia Reczek. “Biosynthesis of β (1, 3)/(1, 6)-glucans of cell wall of the yeast Candida utilis ATCC 9950 strains in the culture media supplemented with deproteinated potato juice water and glycerol.” In: *European Food Research and Technology* 240.5 (2015), pp. 1023–1034.

[22] Anders E Carlsson and Philip V Bayly. “Force generation by endocytic actin patches in budding yeast.” In: *Biophysical journal* 106.8 (2014), pp. 1596–1606.

[23] J Carper. *The CRC handbook of chemistry and physics*. 1999.

[24] Elliot J Carr and Giuseppe Pontrelli. “Modelling mass diffusion for a multi-layer sphere immersed in a semi-infinite medium: application to drug delivery.” In: *Mathematical biosciences* 303 (2018), pp. 1–9.

[25] Lucia Carrillo, Bayram Cucu, Vera Bandmann, Ulrike Homann, Brigitte Hertel, Stefan Hillmer, Gerhard Thiel, and Adam Bertl. “High-resolution membrane capacitance measurements for studying endocytosis and exocytosis in yeast.” In: *Traffic* 16.7 (2015), pp. 760–772.

[26] Xu Chen, Niloufer G Irani, and Jiří Friml. “Clathrin-mediated endocytosis: the gateway into plant cells.” In: *Current opinion in plant biology* 14.6 (2011), pp. 674–682.

[27] Agnieszka Collins, Anthony Warrington, Kenneth A Taylor, and Tatyana Svitkina. “Structural organization of the actin cytoskeleton at sites of clathrin-mediated endocytosis.” In: *Current Biology* 21.14 (2011), pp. 1167–1175.

[28] John Crank. *The mathematics of diffusion*. Oxford university press, 1979.

[29] Nily Dan. “Membrane-induced interactions between curvature-generating protein domains: the role of area perturbation.” In: *AIMS BIOPHYSICS* 4.1 (2017), pp. 107–120.

[30] Philip N Dannhauser and Ernst J Ungewickell. “Reconstitution of clathrin-coated bud and vesicle formation with minimal components.” In: *Nature cell biology* 14.6 (2012), p. 634.

[31] IM De Mara on, Pierre-André Marechal, and Patrick Gervais. “Passive response of Saccharomyces cerevisiae to osmotic shifts: cell volume variations depending on the physiological state.” In: *Biochemical and biophysical research communications* 227 (1996), pp. 519–523.

[32] Daniel Degreif, Bayram Cucu, Itay Budin, Gerhard Thiel, and Adam Bertl. “Lipid determinants of endocytosis and exocytosis in budding yeast.” In: *Biochimica et Biophysica Acta (BBA)-Molecular and Cell Biology of Lipids* 1864.7 (2019), pp. 1005–1016.

[33] Serge Dmitrieff and François Nédélec. “Membrane mechanics of endocytosis in cells with turgor.” In: *PLoS computational biology* 11.10 (2015), e1004538.

[34] Serge Dmitrieff and François Nédélec. “Amplification of actin polymerization forces.” In: *The Journal of Cell Biology* 212.7 (2016), pp. 763–766.

[35] Vincent Dupres, Yves F Dufrêne, and Jurgen J Heinisch. “Measuring cell wall thickness in living yeast cells using single molecular rulers.” In: *ACS nano* 4.9 (2010), pp. 5498–5504.

[36] E Evans and A Yeung. “Hidden dynamics in rapid changes of bilayer shape.” In: *Chemistry and physics of lipids* 73.1-2 (1994), pp. 39–56.

[37] Marijn GJ Ford, Ian G Mills, Brian J Peter, Yvonne Vallis, Gerrit JK Praefcke, Philip R Evans, and Harvey T McMahon. "Curvature of clathrin-coated pits driven by epsin." In: *Nature* 419.6905 (2002), p. 361.

[38] Alexander Fotin, Yifan Cheng, Piotr Sliz, Nikolaus Grigorieff, Stephen C Harrison, Tomas Kirchhausen, and Thomas Walz. "Molecular model for a complete clathrin lattice from electron cryomicroscopy." In: *Nature* 432.7017 (2004), p. 573.

[39] Mitsuhiro Fukuda and Hiromichi Kawai. "Diffusion of low molecular weight substances into a fiber with skin-core structure—rigorous solution of the diffusion in a coaxial cylinder of multiple components." In: *Polymer Engineering & Science* 34.4 (1994), pp. 330–340.

[40] Toshio Fukuda, Fumihito Arai, and Masahiro Nakajima. *Micro-nanorobotic manipulation systems and their applications*. Springer Science & Business Media, 2013.

[41] Brian J Galletta and John A Cooper. "Actin and endocytosis: mechanisms and phylogeny." In: *Current opinion in cell biology* 21.1 (2009), pp. 20–27.

[42] C Gancedo, JM Gancedo, and A Sols. "Glycerol metabolism in yeasts: pathways of utilization and production." In: *European journal of biochemistry* 5.2 (1968), pp. 165–172.

[43] M Giani, WK den Otter, and WJ Briels. "Early stages of clathrin aggregation at a membrane in coarse-grained simulations." In: *The Journal of Chemical Physics* 146.15 (2017), p. 155102.

[44] André Goffeau et al. "Life with 6000 genes." In: *Science* 274.5287 (1996), pp. 546–567.

[45] Björn Goldenbogen, Wolfgang Giese, Marie Hemmen, Jannis Uhlendorf, Andreas Herrmann, and Edda Klipp. "Dynamics of cell wall elasticity pattern shapes the cell during yeast mating morphogenesis." In: *Open biology* 6.9 (2016), p. 160136.

[46] Bruce L Goode, Julian A Eskin, and Beverly Wendland. "Actin and endocytosis in budding yeast." In: *Genetics* 199.2 (2015), pp. 315–358.

[47] IS Gradshteyn and IM Ryzhik. "Table of Integrals, Series and Products." In: *London: Aca—demic* (1980).

[48] Michael J Greenberg, Tianming Lin, Yale E Goldman, Henry Shuman, and E Michael Ostap. "Myosin IC generates power over a range of loads via a new tension-sensing mechanism." In: *Proceedings of the National Academy of Sciences* 109.37 (2012), E2433–E2440.

[49] Morten Grunnet, Nanna MacAulay, Nanna K Jorgensen, Bo Jensen, Søren-Peter Olesen, and Dan A Klaerke. "Regulation of cloned, Ca2+-activated K+ channels by cell volume changes." In: *Pflügers Archiv* 444.1-2 (2002), pp. 167–177.

[50] Julian E Hassinger, George Oster, David G Drubin, and Padmini Rangamani. "Design principles for robust vesiculation in clathrin-mediated endocytosis." In: *Proceedings of the National Academy of Sciences* 114.7 (2017), E1118–E1127.

[51] C Hawes, K Crooks, J Coleman, and B Satiat-Jeunemaitre. "Endocytosis in plants: fact or artefact?" In: *Plant, Cell & Environment* 18.11 (1995), pp. 1245–1252.

[52] Wolfgang Helfrich. "Elastic properties of lipid bilayers: theory and possible experiments." In: *Zeitschrift für Naturforschung C* 28.11-12 (1973), pp. 693–703.

[53] William Mike Henne et al. "Structure and analysis of FCHo2 F-BAR domain: a dimerizing and membrane recruitment module that effects membrane curvature." In: *Structure* 15.7 (2007), pp. 839–852.

[54] *Here we have ignored possible changes in the concentrations resulting from pressure variations, since pressure changes in cells are much smaller than the gigapascal bulk modulus of water.*

[55] RI Hickson, SI Barry, and GN Mercer. "Critical times in multilayer diffusion. Part 1: Exact solutions." In: *International Journal of Heat and Mass Transfer* 52.25-26 (2009), pp. 5776–5783.

[56] Terrell L Hill and Marc W Kirschner. "Bioenergetics and kinetics of microtubule and actin filament assembly–disassembly." In: *International review of cytology* 78 (1982), pp. 1–125.

[57] Lars Hinrichsen, Anika Meyerholz, Stephanie Groos, and Ernst J Ungewickell. "Bending a membrane: how clathrin affects budding." In: *Proceedings of the National Academy of Sciences* 103.23 (2006), pp. 8715–8720.

[58] Takashi Hirama and Gregory D Fairn. "Induction of spontaneous curvature and endocytosis: Unwanted consequences of cholesterol extraction using methyl-β-Cyclodextrin." In: *Communicative & integrative biology* 11.2 (2018), pp. 1–4.

[59] Takashi Hirama, Stella M Lu, Jason G Kay, Masashi Maekawa, Michael M Kozlov, Sergio Grinstein, and Gregory D Fairn. "Membrane curvature induced by proximity of anionic phospholipids can initiate endocytosis." In: *Nature communications* 8.1 (2017), p. 1393.

[60] Daryl P Holland and Anthony E Walsby. "Digital recordings of gas-vesicle collapse used to measure turgor pressure and cell–water relations of cyanobacterial cells." In: *Journal of microbiological methods* 77.2 (2009), pp. 214–224.

[61] Ioana M Ilie, Wouter K den Otter, and Wim J Briels. "Rotational Brownian Dynamics simulations of clathrin cage formation." In: *The Journal of chemical physics* 141.6 (2014), 08B607_1.

[62] Rurika Itofusa, Takuro Tojima, and Hiroyuki Kamiguchi. "Visualization of clathrin-mediated endocytosis during Semaphorin-guided axonal growth." In: *Semaphorin Signaling: Methods and Protocols* (2017), pp. 287–298.

[63] Urška Jelerčič and Nir S Gov. “Pearling instability of membrane tubes driven by curved proteins and actin polymerization.” In: *Physical biology* 12.6 (2015), p. 066022.

[64] Albert J Jin, Kondury Prasad, Paul D Smith, Eileen M Lafer, and Ralph Nossal. “Measuring the elasticity of clathrin-coated vesicles via atomic force microscopy.” In: *Biophysical journal* 90.9 (2006), pp. 3333–3344.

[65] Ludger Johannes, Christian Wunder, and Patricia Bassereau. “Bending on the rocksa cocktail of biophysical modules to build endocytic pathways.” In: *Cold Spring Harbor perspectives in biology* 6.1 (2014), a016741.

[66] HT Johansson and C Forssén. “Fast and Accurate Evaluation of Wigner 3 j, 6 j, and 9 j Symbols Using Prime Factorization and Multiword Integer Arithmetic.” In: *SIAM Journal on Scientific Computing* 38.1 (2016), A376–A384.

[67] Marko Kaksonen and Aurélien Roux. “Mechanisms of clathrin-mediated endocytosis.” In: *Nature Reviews Molecular Cell Biology* 19.5 (2018), p. 313.

[68] Marko Kaksonen, Christopher P Toret, and David G Drubin. “Harnessing actin dynamics for clathrin-mediated endocytosis.” In: *Nature reviews molecular cell biology* 7.6 (2006), pp. 404–414.

[69] Christoph Kalthoff, Jürgen Alves, Claus Urbanke, Ruth Knorr, and Ernst J Ungewickell. “Unusual structural organization of the endocytic proteins AP180 and epsin 1.” In: *Journal of Biological Chemistry* 277.10 (2002), pp. 8209–8216.

[70] Sara Karlgren, Nina Pettersson, Bodil Nordlander, John C Mathai, Jeffrey L Brodsky, Mark L Zeidel, Roslyn M Bill, and Stefan Hohmann. “Conditional Osmotic Stress in Yeast A SYSTEM TO STUDY TRANSPORT THROUGH AQUAGLYCEROPORINS AND OSMOSTRESS SIGNALING.” In: *Journal of biological chemistry* 280.8 (2005), pp. 7186–7193.

[71] ARTHUR L Koch and MF Pinette. “Nephelometric determination of turgor pressure in growing gram-negative bacteria.” In: *Journal of bacteriology* 169.8 (1987), pp. 3654–3663.

[72] Christian Kock, Yves F Dufrêne, and Jürgen J Heinisch. “Up against the wall: is yeast cell wall integrity ensured by mechanosensing in plasma membrane microdomains?” In: *Appl. Environ. Microbiol.* 81.3 (2015), pp. 806–811.

[73] Svetlana Kotova, Kondury Prasad, Paul D Smith, Eileen M Lafer, Ralph Nossal, and Albert J Jin. “AFM visualization of clathrin triskelia under fluid and in air.” In: *FEBS letters* 584.1 (2010), pp. 44–48.

[74] TV Sachin Krishnan, Sovan L Das, and PB Sunil Kumar. “Transition from curvature sensing to generation in a vesicle driven by protein binding strength and membrane tension.” In: *Soft matter* 15.9 (2019), pp. 2071–2080.

[75] Wanda Kukulski, Martin Schorb, Marko Kaksonen, and John AG Briggs. "Plasma membrane reshaping during endocytosis is revealed by time-resolved electron tomography." In: *Cell* 150.3 (2012), pp. 508–520.

[76] Wanda Kukulski, Andrea Picco, Tanja Specht, John AG Briggs, and Marko Kaksonen. "Clathrin modulates vesicle scission, but not invagination shape, in yeast endocytosis." In: *Elife* 5 (2016), e16036.

[77] LD Landau and EM Lifshitz. *Statistical Physics: V. 5: Course of Theoretical Physics*. Pergamon Press, 1969.

[78] Jian Liu, Yidi Sun, David G Drubin, and George F Oster. "The mechanochemistry of endocytosis." In: *PLoS biology* 7.9 (2009), e1000204.

[79] James A Lockhart. "A new method for the determination of osmotic pressure." In: *American Journal of Botany* 46.10 (1959), pp. 704–708.

[80] Rebecca Lu, David G Drubin, and Yidi Sun. "Clathrin-mediated endocytosis in budding yeast at a glance." In: *J Cell Sci* 129.8 (2016), pp. 1531–1536.

[81] Richard Lundmark and Sven R Carlsson. "Driving membrane curvature in clathrin-dependent and clathrin-independent endocytosis." In: *Seminars in cell & developmental biology*. Vol. 21. 4. Elsevier. 2010, pp. 363–370.

[82] Ying Luo, Jianguo Wang, Bin Liu, Zhouli Wang, Yahong Yuan, and Tianli Yue. "Effect of yeast cell morphology, cell wall physical structure and chemical composition on patulin adsorption." In: *PloS one* 10.8 (2015), e0136045.

[83] Steve A Maas, Benjamin J Ellis, Gerard A Ateshian, and Jeffrey A Weiss. "FEBio: finite elements for biomechanics." In: *Journal of biomechanical engineering* 134.1 (2012), p. 011005.

[84] Wojciech Makałowski. "The human genome structure and organization." In: *Acta Biochim. Pol* 48 ().

[85] BN Mandal and Nanigopal Mandal. *Advances in dual integral equations*. Vol. 400. CRC Press, 1998.

[86] Christopher Mazzochi, James K Bubien, Peter R Smith, and Dale J Benos. "The carboxyl terminus of the α-subunit of the amiloride-sensitive epithelial sodium channel binds to F-actin." In: *Journal of Biological Chemistry* 281.10 (2006), pp. 6528–6538.

[87] Harvey T McMahon and Emmanuel Boucrot. "Molecular mechanism and physiological functions of clathrin-mediated endocytosis." In: *Nature reviews Molecular cell biology* 12.8 (2011), p. 517.

[88] Harvey T McMahon and Emmanuel Boucrot. "Membrane curvature at a glance." In: *J Cell Sci* 128.6 (2015), pp. 1065–1070.

[89] Klaus R Mecke, Thierry Charitat, and François Graner. "Fluctuating lipid bilayer in an arbitrary potential: theory and experimental determination of bending rigidity." In: *Langmuir* 19.6 (2003), pp. 2080–2087.

[90] Amanda J Meikle, Robert H Reed, and Geoffrey M Gadd. “Osmotic adjustment and the accumulation of organic solutes in whole cells and protoplasts of Saccharomyces cerevisiae.” In: *Microbiology* 134.11 (1988), pp. 3049–3060.

[91] Mirko Messa et al. “Epsin deficiency impairs endocytosis by stalling the actin-dependent invagination of endocytic clathrin-coated pits.” In: *Elife* 3 (2014).

[92] Marta Miaczynska and Harald Stenmark. *Mechanisms and functions of endocytosis*. 2008.

[93] Marziale Milani et al. “Differential two-color x-ray radiobiology of membrane/cytoplasm in yeast cells and lymphocytes.” In: *Advances in Optical Biophysics*. Vol. 3256. International Society for Optics and Photonics. 1998, pp. 195–206.

[94] Carsten Mim and Vinzenz M Unger. “Membrane curvature and its generation by BAR proteins.” In: *Trends in biochemical sciences* 37.12 (2012), pp. 526–533.

[95] Nicolas Minc, Arezki Boudaoud, and Fred Chang. “Mechanical forces of fission yeast growth.” In: *Current Biology* 19.13 (2009), pp. 1096–1101.

[96] Katarina Moravcevic, Diego Alvarado, Karl R Schmitz, Jon A Kenniston, Jeannine M Mendrola, Kathryn M Ferguson, and Mark A Lemmon. “Comparison of Saccharomyces cerevisiae F-BAR domain structures reveals a conserved inositol phosphate binding site.” In: *Structure* 23.2 (2015), pp. 352–363.

[97] Dale Muzzey, Carlos A Gómez-Uribe, Jerome T Mettetal, and Alexander van Oudenaarden. “A systems-level analysis of perfect adaptation in yeast osmoregulation.” In: *Cell* 138.1 (2009), pp. 160–171.

[98] Ralph Nossal and Joshua Zimmerberg. “Endocytosis: curvature to the ENTH degree.” In: *Current Biology* 12.22 (2002), R770–R772.

[99] Ryusuke Ohmiya, Hisami Yamada, Kyoko Nakashima, Hirofumi Aiba, and Takeshi Mizuno. “Osmoregulation of fission yeast: cloning of two distinct genes encoding glycerol-3-phosphate dehydrogenase, one of which is responsible for osmotolerance for growth.” In: *Molecular microbiology* 18.5 (1995), pp. 963–973.

[100] KJ Oparka, KM Wright, EA Murant, and EJ Allan. “Fluid-phase endocytosis: do plants need it?” In: *Journal of experimental botany* (1993), pp. 247–255.

[101] Karin M Overkamp, Barbara M Bakker, Peter Kötter, Marijke AH Luttik, Johannes P van Dijken, and Jack T Pronk. “Metabolic engineering of glycerol production in Saccharomyces cerevisiae.” In: *Appl. Environ. Microbiol.* 68.6 (2002), pp. 2814–2821.

[102] Li-Long Pan, Qun-Fang Chen, Juan-Juan Zhao, Tao Guo, Xiao-Wei Wang, Aliza Hariton-Shalev, Henryk Czosnek, and Shu-Sheng Liu. “Clathrin-mediated endocytosis is involved in Tomato yellow leaf curl virus transport across the midgut barrier of its whitefly vector.” In: *Virology* 502 (2017), pp. 152–159.

[103] Andrea Picco, Markus Mund, Jonas Ries, François Nedelec, and Marko Kaksonen. "Visualizing the functional architecture of the endocytic machinery." In: *Elife* 4 (2015), e04535.

[104] Andrea Picco, Markus Mund, Jonas Ries, François Nédélec, and Marko Kaksonen. "Visualizing the functional architecture of the endocytic machinery." In: *eLife* 4 (2015), e04535.

[105] Thomas D Pollard. "Rate constants for the reactions of ATP-and ADP-actin with the ends of actin filaments." In: *The Journal of cell biology* 103.6 (1986), pp. 2747–2754.

[106] NV Popova, IE Deyev, and AG Petrenko. "Clathrin-mediated endocytosis and adaptor proteins." In: *Acta Naturae ( )* 5.3 (18) (2013).

[107] Meenakshi Prabhune, Florian Rehfeldt, and Christoph F Schmidt. "Molecular force sensors to measure stress in cells." In: *Journal of Physics D: Applied Physics* 50.23 (2017), p. 233001.

[108] Vyas Ramanan, Neeraj J Agrawal, Jin Liu, Sean Engles, Randall Toy, and Ravi Radhakrishnan. "Systems biology and physical biology of clathrin-mediated endocytosis." In: *Integrative Biology* 3.8 (2011), pp. 803–815.

[109] Jean-Philippe Richard et al. "Intracellular curvature-generating proteins in cell-to-cell fusion." In: *Biochemical Journal* 440.2 (2011), pp. 185–193.

[110] Stephen J Royle. "The cellular functions of clathrin." In: *Cellular and Molecular Life Sciences CMLS* 63.16 (2006), pp. 1823–1832.

[111] Mohammed Saleem, Sandrine Morlot, Annika Hohendahl, John Manzi, Martin Lenz, and Aurélien Roux. "A balance between membrane elasticity and polymerization energy sets the shape of spherical clathrin coats." In: *Nature communications* 6 (2015), p. 6249.

[112] Abhishek Saxena and Ramakrishnan Sitaraman. "Osmoregulation in Saccharomyces cerevisiae via mechanisms other than the high-osmolarity glycerol pathway." In: *Microbiology* 162.9 (2016), pp. 1511–1526.

[113] Jörg Schaber et al. "Biophysical properties of Saccharomyces cerevisiae and their relationship with HOG pathway activation." In: *European Biophysics Journal* 39.11 (2010), pp. 1547–1556.

[114] Jonah K Scher-Zagier and Anders E Carlsson. "Local turgor pressure reduction via channel clustering." In: *Biophysical journal* 111.12 (2016), pp. 2747–2756.

[115] Roger Schneiter et al. "Electrospray ionization tandem mass spectrometry (ESI-MS/MS) analysis of the lipid molecular species composition of yeast subcellular membranes reveals acyl chain-based sorting/remodeling of distinct molecular species en route to the plasma membrane." In: *The Journal of cell biology* 146.4 (1999), pp. 741–754.

[116] Brandon L Scott et al. "Membrane bending begins at any stage of clathrin-coat assembly and defines endocytic dynamics." In: *bioRxiv* (2017), p. 163303.

[117] Atsushi Shimada et al. "Curved EFC/F-BAR-domain dimers are joined end to end into a filament for membrane invagination in endocytosis." In: *Cell* 129.4 (2007), pp. 761–772.

[118] Mijo Simunovic, Gregory A Voth, Andrew Callan-Jones, and Patricia Bassereau. "When physics takes over: BAR proteins and membrane curvature." In: *Trends in cell biology* 25.12 (2015), pp. 780–792.

[119] Mijo Simunovic et al. "How curvature-generating proteins build scaffolds on membrane nanotubes." In: *Proceedings of the National Academy of Sciences* (2016), p. 201606943.

[120] Vladimir Sirotkin, Julien Berro, Keely Macmillan, Lindsey Zhao, and Thomas D Pollard. "Quantitative analysis of the mechanism of endocytic actin patch assembly and disassembly in fission yeast." In: *Mol. Biol. Cell* 21.16 (2010), pp. 2894–2904.

[121] Michal Skruzny, Thorsten Brach, Rodolfo Ciuffa, Sofia Rybina, Malte Wachsmuth, and Marko Kaksonen. "Molecular basis for coupling the plasma membrane to the actin cytoskeleton during clathrin-mediated endocytosis." In: *Proceedings of the National Academy of Sciences* (2012), p. 201207011.

[122] AE Smith, KE Moxham, and APJ Middelberg. "Wall material properties of yeast cells. Part II. Analysis." In: *Chemical Engineering Science* 55.11 (2000), pp. 2043–2053.

[123] Alex J Smith and Alan S Verkman. "Superresolution Imaging of Aquaporin-4 Cluster Size in Antibody-Stained Paraffin Brain Sections." In: *Biophysical journal* 109.12 (2015), pp. 2511–2522.

[124] Alexander E Smith, Zhibing Zhang, Colin R Thomas, Kennith E Moxham, and Anton PJ Middelberg. "The mechanical properties of Saccharomyces cerevisiae." In: *Proceedings of the National Academy of Sciences* 97.18 (2000), pp. 9871–9874.

[125] Alexander Evans Smith, Z Zhang, and CR Thomas. "Wall material properties of yeast cells: Part 1. Cell measurements and compression experiments." In: *Chemical Engineering Science* 55.11 (2000), pp. 2031–2041.

[126] Zachary J Smith. *Integrated Raman and angular scattering of single biological cells*. ProQuest, 2009.

[127] Wilton T Snead, Carl C Hayden, Avinash K Gadok, Chi Zhao, Eileen M Lafer, Padmini Rangamani, and Jeanne C Stachowiak. "Membrane fission by protein crowding." In: *Proceedings of the National Academy of Sciences* 114.16 (2017), E3258–E3267.

[128] Tolga Soykan, Natalie Kaempf, Takeshi Sakaba, Dennis Vollweiter, Felix Goerdeler, Dmytro Puchkov, Natalia L Kononenko, and Volker Haucke. "Synaptic vesicle endocytosis occurs on multiple timescales and is mediated by formin-dependent actin assembly." In: *Neuron* 93.4 (2017), pp. 854–866.

[129] John D Stenson, Peter Hartley, Changxiang Wang, and Colin R Thomas. "Determining the mechanical properties of yeast cell walls." In: *Biotechnology progress* 27.2 (2011), pp. 505–512.

[130] Kimberly M Stroka, Hongyuan Jiang, Shih-Hsun Chen, Ziqiu Tong, Denis Wirtz, Sean X Sun, and Konstantinos Konstantopoulos. "Water permeation drives tumor cell migration in confined microenvironments." In: *Cell* 157.3 (2014), pp. 611–623.

[131] Shiro Suetsugu. "Higher-order assemblies of BAR domain proteins for shaping membranes." In: *Journal of Electron Microscopy* 65.3 (2016), pp. 201–210.

[132] Shiro Suetsugu, Shusaku Kurisu, and Tadaomi Takenawa. "Dynamic shaping of cellular membranes by phospholipids and membrane-deforming proteins." In: *Physiological reviews* 94.4 (2014), pp. 1219–1248.

[133] Yidi Sun, Adam C Martin, and David G Drubin. "Endocytic internalization in budding yeast requires coordinated actin nucleation and myosin motor activity." In: *Developmental cell* 11.1 (2006), pp. 33–46.

[134] Markus J Tamás et al. "Fps1p controls the accumulation and release of the compatible solute glycerol in yeast osmoregulation." In: *Molecular microbiology* 31.4 (1999), pp. 1087–1104.

[135] DJ Tweten, PV Bayly, and AE Carlsson. "Actin growth profile in clathrin-mediated endocytosis." In: *Physical Review E* 95.5 (2017), p. 052414.

[136] Agnieszka N Urbanek, Adam P Smith, Ellen G Allwood, Wesley I Booth, and Kathryn R Ayscough. "A novel actin-binding motif in Las17/WASP nucleates actin filaments independently of Arp2/3." In: *Current Biology* 23.3 (2013), pp. 196–203.

[137] Dominic Vella, Amin Ajdari, Ashkan Vaziri, and Arezki Boudaoud. "The indentation of pressurized elastic shells: from polymeric capsules to yeast cells." In: *Journal of the Royal Society Interface* 9.68 (2011), pp. 448–455.

[138] Nikhil Walani, Jennifer Torres, and Ashutosh Agrawal. "Endocytic proteins drive vesicle growth via instability in high membrane tension environment." In: *Proceedings of the National Academy of Sciences* 112.12 (2015), E1423–E1432.

[139] Daobing Wang, Jeff Sletto, Brandon Tenay, and Kyoungtae Kim. "Yeast dynamin implicated in endocytic scission and the disassembly of endocytic components." In: *Communicative & integrative biology* 4.2 (2011), pp. 178–181.

[140] Xinxin Wang, Brian J Galletta, John A Cooper, and Anders E Carlsson. "Actin-Regulator Feedback Interactions during Endocytosis." In: *Biophysical Journal* 110.6 (2016), pp. 1430–1443.

[141] A Wesp, L Hicke, J Palecek, R Lombardi, T Aust, AL Munn, and H Riezman. "End4p/Sla2p interacts with actin-associated proteins for endocytosis in Saccharomyces cerevisiae." In: *Molecular Biology of the Cell* 8.11 (1997), pp. 2291–2306.

[142] Xin-Sheng Wu, Sharon Elias, Huisheng Liu, Johanna Heureaux, Peter J Wen, Allen P Liu, Michael M Kozlov, and Ling-Gang Wu. "Membrane tension inhibits rapid and slow endocytosis in secretory cells." In: *Biophysical journal* 113.11 (2017), pp. 2406–2414.

[143] Xianfa Xie and Peter N Lipke. "On the evolution of fungal and yeast cell walls." In: *Yeast* 27.8 (2010), pp. 479–488.

[144] Ayako Yamada et al. "Catch-bond behaviour facilitates membrane tubulation by non-processive myosin 1b." In: *Nature communications* 5 (2014).

[145] Baoxue Yang and AS Verkman. "Water and glycerol permeabilities of aquaporins 1–5 and MIP determined quantitatively by expression of epitope-tagged constructs in Xenopus oocytes." In: *Journal of Biological Chemistry* 272.26 (1997), pp. 16140–16146.

[146] Shirley Yang, M Jamie TV Cope, and David G Drubin. "Sla2p is associated with the yeast cortical actin cytoskeleton via redundant localization signals." In: *Molecular biology of the cell* 10.7 (1999), pp. 2265–2283.

[147] Tao Zhang, Rastko Sknepnek, MJ Bowick, and JM Schwarz. "On the modeling of endocytosis in yeast." In: *Biophysical journal* 108.3 (2015), pp. 508–519.

[148] Yalan Zhang et al. "Kv3. 3 Channels Bind Hax-1 and Arp2/3 to Assemble a Stable Local Actin Network that Regulates Channel Gating." In: *Cell* (2016).